SELF HEALING OF DEFORMATION-INDUCED DAMAGE IN Fe-W ALLOYS

Nikodem Krzysztof Szymański

TU Delft

REACTOR
INSTITUTE
DELFT

Self-healing of deformation-induced damage in Fe-W alloys

by

Nikodem Krzysztof Szymański

in the partial fulfillment of the requirements for the degree of
Master of Science in Aerospace Engineering
at the Delft University of Technology,
to be defended publicly on Wednesday, December 20, 2017 at 10:00 AM.

Student number:	4504615	
Project duration:	March 1 – December 20, 2017	
Thesis committee:	Dr. ir. N.H. van Dijk,	TNW, TU Delft, supervisor
	Prof. dr. ir. S. van der Zwaag,	LR, TU Delft
	Dr. S. J. Garcia Espallargas,	LR, TU Delft
	Dr. S. R. Turteltaub,	LR, TU Delft

TUDelft

REACTOR
INSTITUTE
DELFT

Próbowałam różnych doświadczeń opisanych w podręcznikach fizyki i chemii. Niekiedy dodawał mi otuchy jakiś drobny sukces, kiedy indziej znów wpadałam w głęboką rozpacz z powodu wypadków i błędów, wynikających z mojego braku doświadczenia. Na ogół jednak wiedziałam, że postępy nie mogą przychodzić ani szybko, ani łatwo; te pierwsze próby utrwaliły we mnie zamiłowanie do badań eksperymentalnych z dziedziny fizyki i chemii.

I tried to reproduce various experiments described in the treatises on physics or chemistry. From time to time a little unhoped-for success would come to encourage me, and at other times I sank into despair because of the accidents or failures due to my inexperience. However, on the whole, I learned, that progress in such matters is neither rapid nor easy, I developed my taste for experimental research during these first trials.

Maria Skłodowska-Curie (on her research beginnings)

Preface

This Thesis report is the result of my the Master's Thesis research at the group of Novel Aerospace Materials (LR, TU Delft) in the collaboration with the group of Fundamental Aspects of Materials and Energy at the Reactor Institute Delft (TNW, TU Delft). The aim of the report is to disclose the details behind the research project and its results on the subject of self healing of the deformation-induced damage in Fe-W alloys. The insight on this topic has been gained by means of mechanical testing at high temperatures and sophisticated microstructural characterization techniques at Delft University of Technology and at ESRF facilities in Grenoble, France. The final outcomes of this project certainly demystified the development of damage in Fe-W alloys and their subsequent filling mechanism by solute transport under creep conditions, which has been studied using various computational and experimental methods. Now, a greater knowledge has been gained and a further development of the self-healing alloys for structural applications can be considered.

At this point, I would like to express by gratitude to all the people involved in this project. Not only this work would not have been possible, but also my stay in Delft would have been extremely dull without them. This Thesis concludes my 2-year life in the Netherlands, which certainly was fruitful and full of adventures.

Firstly, I would like to thank my daily supervisor, Dr.ir. N.H. van Dijk, for his continuous support, excellent supervision and scientific insight he conveyed me. I really enjoyed all the meetings with him, which were always absolutely helpful, reassuring, and full of jokes and historical/geographical facts. I can easily say that I have expanded my knowledge on every possible matter thanks to Niels.

I owe a big debt of gratitude to my main supervisor, Prof.dr.ir. S. van der Zwaag for the opportunity to take part in this project, which included many brilliant minds and interesting members. He always offered me his help and supervision, not only during my Thesis work, but also throughout my entire studies at Novel Aerospace Materials Department. His great knowledge, which he conveyed me, occurred to be extremely useful during my every academic struggle.

Additionally, I would like to express my appreciation to Dr.ir. N.H. van Dijk and Prof.dr.ir. S. van der Zwaag for an opportunity of joining them on the research, that took place in the facilities of ESRF in Grenoble, France. The journey was absolutely pleasant, full of entertainment, but most importantly, filled with work using X-ray nano-tomography, which enabled me to obtain my most essential research results.

Furthermore, I would like to thank C.D. Versteylen for his endless support with the finite element calculations utilized in this project. He always had time for me, when I approached him, always shared his insight with me and was patient, when I had troubles understanding the code and the concept. Thanks to Casper I gained a huge knowledge on finite element modelling, which will be extremely helpful for my future.

I would like to express a special and sincere gratitude to H. Fang. His support and help was countless and I do not know how to properly address my acknowledgements. Haixing helped me with every single matter during the whole duration of this project, and I am certain, that without his presence, these following pages would be blank. His patience and availability were sometimes impossible to comprehend for me, as he had to deal with my lack of insight on the daily basis. I am simply concluding this expression of gratitude towards Haixing with a statement, that I honestly think he is the best researcher I have ever had the pleasure to meet.

Moreover, I would like to thank Drs. K. Goubtiz, S. Visser, staff members from RID, LR and 3mE faculties, and all my colleagues whom I worked with, for their academic help and support, as well as, all of my friends in Delft and Antwerp, whom I shared the greatest moments of my life with, during my studies.

Finally, I would like to deeply thank my parents in Poland for their love, support and encouragement. Last but not least, a special thank goes to my closest friends from Poland, who always reminded me that my stay in the Netherlands is not meaningless and found the time for long talks over the phone.

Nikodem Krzysztof Szymański

Abstract

The autonomous filling of creep-induced grain-boundary cavities by tungsten-rich precipitates has been studied for Fe-W alloys at various temperatures, loading conditions and creep rupture times. To this aim, scanning electron microscopy, energy-dispersive spectroscopy and X-ray nano-tomography were used. Additionally, the effect of local plastic deformation, followed by ageing processes, on the surface precipitation in these alloys has been studied by means of scanning electron microscopy, together with energy-dispersive spectroscopy. Finally, a diffusion-based finite element analysis has been performed to study cavity filling for different combination of diffusion mechanisms. From scanning electron micrographs it can be confirmed, that Fe-W alloys show damage-selective precipitation of the Laves phase (Fe_2W). Furthermore, the filling ratios of individual cavities are determined and it is found, that the autonomous healing strongly depends on the duration of the loading at of elevated temperature. From the quantitative analysis of the size and shape of the precipitates and cavities it is found, that the orientation of grain boundaries to the stress direction has an influence on the morphology of the induced-cavities, as well as, the filling ratio. The grain-boundary cavities orientated favourably for the cavity growth show low filling ratios, due to the fact, that their propagation proceeds with a higher rate than the solute transport. The critical volume of a cavity, that can be fully filled with solute atoms, is found to be of the order of 10 μm^3, while the average filling ratio for Fe-W alloys is found to be around 50% for the sample loaded to 100% of its lifetime. Moreover, the scanning electron micrographs of the indentation-deformed samples subjected to ageing revealed surface precipitates (Fe_2W), which existence has to be further researched. The hardness measurements of Fe-W samples showed that after 200 hours of ageing at 580°C, the strength of the alloy is only reduced if the material has been pre-strained, but it remains constant for the solution heat treated specimens. This result shows, that the process of dislocation recovery dominates over work-hardening only in the case of a high dislocation density. Finally, the finite element analysis revealed, that during the diffusive cavity filling of an equilibrium-shaped void, three different diffusion profile regimes are plausible. Namely, a diffusive filling dominated by volume diffusion, which occurs for a relatively small spacing between neighbouring cavities and is independent of the ratio of bulk and grain-boundary diffusion. Secondly, a diffusive filling governed by volume diffusion with contributing grain-boundary diffusion, which occurs for relatively low ratios of bulk and grain-boundary diffusion. And ultimately, a diffusive filling governed by grain-boundary diffusion, which occurs for relatively high ratios of bulk and grain-boundary diffusion.

Contents

1

Introduction

One of the most concerning issues of today's world is the unpredictability of the lifespan of anything that has been created, either by humans or nature. The greatest goal of all has always been to more or less 'guarantee' a minimal lifespan of anything that exists, irrespective of any (initially non-fatal) damage which it encountered during its life. While the nature has supplied the living organisms with an ability to reconstruct and heal local non-fatal damage and thereby prolong the subsequent lifetime, man-made materials and constructions lack such a feature. Therefore, engineers and scientists, inspired by the self healing mechanisms in nature, decided to devise and incorporate self mechanisms into man-made materials. This idea gained a high popularity in early 21st century, following a land-mark paper by White et al. [84] in which healing of a thermoset polymer, due to the inclusion of micro-capsules filled with a liquid adhesive, was demonstrated. The concept however dates back to the less-known work by Dry [22] in which the matrix material was concrete. Since then, self-healing systems have been introduced into polymers, fibre-reinforced composites, asphalt, concrete and metallic materials [78, 79].

The work described in this thesis focuses on the formation of local damage and its subsequent healing, during continuous loading at high temperatures, in a model alloy for so-called creep-resistant steels, which are utilized at high temperatures and so-called creep loading conditions. Creep-resistant steels are the key construction materials in thermally and mechanically loaded elements in high temperature installations, such as steam turbines and aeroengines. Under the combined effect of temperature and stress, the components show the well-known phenomenon of creep deformation. Creep deformation not only leads to dimensional changes, but also to microstructural changes which eventually lead to premature fracture of the component. This damage usually starts at grain boundaries and is in the form of cavities, which grow and coalesce with proceeding deformation. Traditional methods to design more robust creep-resistant steels with either the ability to endure higher stresses or with a longer lifetime, focus on compositional and microstructural changes, which prevent, or at least retard, the formation of the creep cavities at the grain boundaries. Hence, the traditional approach focuses on the prevention rather than the (autonomous) management of the creep damage [78]. The approach, which is the subject of this work, i.e. autonomous self healing of early stage creep damage, does not deal with the enhancement of the initial properties of the material, but with autonomous control or healing of damage, during the entire period of creep deformation, as the aim is to obtain as significantly increased 'guaranteed' lifetime.

As first explicitly expressed in [37, 78], an autonomous self healing ability in a material requires the presence of "local temporary mobility" which does not compromise its initial properties too much [30]. In particular, the condition of 'mobility' is important as repair of damage requires the transport of the 'healing agent' from its original position to the damage site. While designing for self healing behaviour is now an intentional design route, it has been discovered that self healing sometimes also occurs in conventional materials, such as old concrete bridges, that autonomously filled their cracks with newly reacted calcite [78]. Self healing in steels is hard to achieve as the high melting point of steels implies a very strong bonding between the constituent atoms (the dominant iron atoms and the substitutional and interstitial alloying elements) resulting in a very low (or virtually absent) intrinsic mobility at room or modest temperatures. Only when steels are exposed to high temperatures (typically >550°C), the atomic mobility reaches a value that leads to healing of the small scale local damage. As the healing reaction involves the controlled autonomous deposition of well-selected alloying elements in the creep cavities, the starting condition at the beginning of the creep loading should be the one of an over-saturated solid solution [30]. In response to the newly-created open volume defects the solute atoms move via volume and grain-boundary diffusion to the surfaces of the cavities and segregate there. The healing automatically stops when all the solute atoms are used to form precipitates at damage sites or when a cavity is fully filled [86]. The filling of the cavities not only prolongs the lifetime of the material, but also enhances its strength and creep properties.

The most successful creep damage healing results have been obtained with Fe-Au model alloys. Fang et al. [24] developed an iron-gold system which evidently showed precipitation of gold-rich phases in creep deformation-induced grain-boundary cavities, when subjected to stress levels of 60 – 120 MPa at temperature of 550°C. Another worth-mentioning material that has been studied, is the iron-copper steel grade. Unlike the Au atoms, copper showed both precipitation at crack surfaces and inside the bulk. A substantial fraction of the healing agents, in this case the Cu atoms, were rendered immobile by internal precipitation in the interior of the grain and could no longer contribute to the healing reaction. Hence, the Fe-Cu system is considered to be a rather inefficient system for self healing of creep damage [39, 40]. As internal homogeneous precipitation is less likely to occur for atoms with a larger atoms radius, recent research focused on the iron-molybdenum system and the precipitation of Mo-rich phases in creep cavities has been demonstrated [89]. The current research is focused on yet another system selected on the guiding principle of large diameter solute atoms which can be brought into a supersaturated state, the iron-tungsten (Fe-W) system.

The main aim of this research Thesis is to investigate the self healing mechanism of the aforementioned ferritic Fe-W alloys. In particular, the healing of deformation-induced damage, which is either formed during creep loading or by micro-indentation. The (internal quasi-homogeneous) creep-induced damage is formed during the mechanical tests of the alloys and its filling is examined afterwards, while the local surface indentation-induced damage is formed during plastic deformation of the alloys' surface in ambient environment and its filling and strength changes are investigated after ageing processes. Each of this experiments is performed at different testing conditions, in order to thoroughly evaluate the self healing mechanism. The experimental techniques used for the second phase precipitation examination include scanning electron microscopy, energy-dispersive spectroscopy and X-ray nano-tomography. Additionally, a diffusion-based finite element analysis is performed for the general case of Fe-X substitutional model alloys, in order to evaluate the role of the various diffusion mechanisms in controlling the filling of the creep-induced cavity, having an equilibrium starting shape. The diffusivity values are adequately varied to gain an insight on all possible cases of the diffusive solute transport in Fe-X alloys.

The Thesis report commences with the theoretical background on creep deformation, its damage nucleation and evolution, and a review on currently used methods to elongate creep lifetime (Chapter 2). Then, the notion of a general self healing effect is described, together with the detailed description of autonomous repair in steels and its applications and prospects (Chapter 3). Subsequently, the main matter is addressed, which includes the description of Fe-W alloys, the mechanical creep testing and experimental investigation of their self healing effect (Chapter 4). Then, the results of the investigation of the indentation-deformed surfaces after (stress-free) ageing is presented (Chapter 5). The report ends with the detailed description of the diffusion-based finite element model, together with its outcomes and directions for future research on the self healing effect in creep steels (Chapter 6).

2

Creep deformation

In this chapter, the phenomenon of creep and creep damage in metallic materials and in particular (ferritic) steels is presented. Although the Thesis report is on the healing of creep damage, it is important to describe and analyze the processes which lead to the formation of creep damage. Creep, the plastic elongation of a material loaded at a high temperature (at a homologous temperature >$0.4T_{melt,}$ when T_{melt} is expressed in Kelvin) for a long time at a constant external load, is known as a slow, time-dependent and continuous plastic deformation of a material, and it involves the combined contributions of dislocation motion and diffusion [2]. The chapter commences with the description of creep behaviour, and is followed by a section on the classification of creep mechanisms, that govern the deformation of materials under specific conditions. Then, the chapter introduces the various mechanisms for creep damage formation and ends with the description of some potential approaches to control and prevent the formation of creep damage.

2.1. Creep behaviour

Typically, to determine the tensile strength of a metal, a quasi-static or even a dynamic tensile test is required, in which the applied load increases continuously as a function of time. However, in the case of conventional creep testing, creep deformation takes place under a constant load and the strain rate is measured as a function of time until the final fracture takes place [5, 32]. As creep is to provide information on the long term behaviour of a material, the loading conditions are selected such that a specimen failure will take place after a relatively long time, ranging from 1000 to over 200,000 hours. To show the various stages of the creep deformation the actual creep curves (see Fig. 2.1) are often presented on logarithmic time scales [5]. In Fig. 2.1 it can be observed, that with the application of a load there is a rapid initial strain, which is the sum of the elastic deformation and the instantaneous plastic deformation. As this strain is non-dependent on time, the initial elongation is not classified as being part of the creep process. Following the instantaneous strain evolution, Stage I (also called primary creep stage) occurs. During this stage, there is a significant continuous change of the creep rate (i.e. plastic strain rate) with time and accumulated plastic strain. With the creep rate decreasing, after some time, the creep rate (on a logarithmic time scale) becomes constant and this state can be sustained for a long period of time. This stage is called Stage II (also stationary, steady-state or secondary stage). During this stage, the total creep strain increases linearly with the logarithm of time [5, 32]. From a time perspective, stretching from the application of the load to the moment of sample failure, Stage II very often is the dominant part of the creep curve, and a parameter called steady-state creep rate ($\dot{\varepsilon}_{SS} = \Delta\epsilon/\Delta t$) can be derived from it. This steady state creep rate is very important as it is used in the calculations of the engineering design parameters of all metallic components that are subjected to creep deformation in service. Using steady-state creep rate, an allowable applied stress of a component can be estimated [5, 32, 33]. Subsequently after the second stage, the creep curve enters the region, where its creep rate significantly increases as a function of time (stage III). The accelerated creep is mainly caused by the additional elongation of the sample, due to the extensive cavitation and/or cracking that nucleated. Stage III of a creep curve is called tertiary stage, and it eventually ends with a final creep fracture of a sample [5, 32].

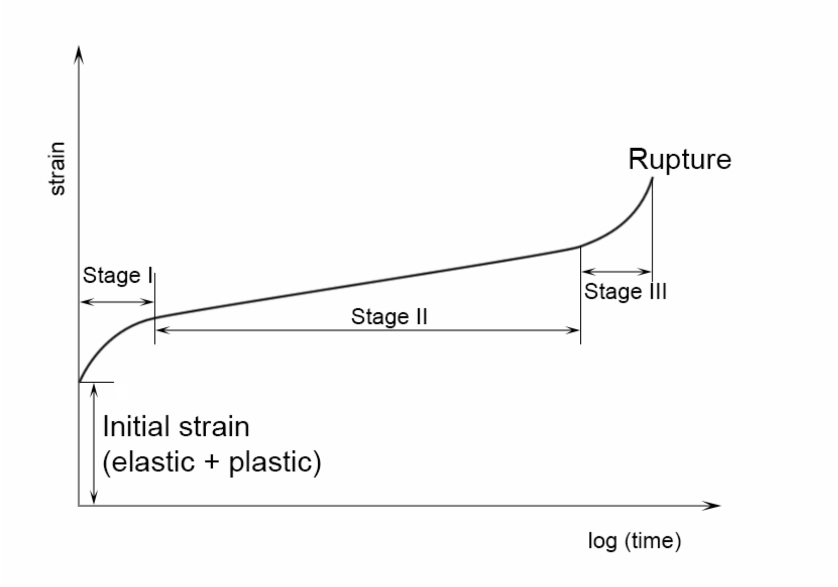

Figure 2.1: Schematic representation of a creep curve.

At every creep curve stage different deformation processes occur. These processes are:

- Stage I: The high initial creep rate is caused by the activation of primary glide systems, which allows the primary dislocations to become mobile. Subsequently, the primary dislocations are multiplied by Frank-Read sources and joined by dislocations generated from grain boundaries or defects, which increases the dislocation density in a material. Such a phenomenon of the dislocation density increase is called work-hardening and lasts until the primary dislocation motion is stopped by secondary dislocations or grain boundaries. As the creep process takes place at higher temperatures, at which diffusion takes place, a dynamic equilibrium is formed between dislocation production (work hardening) and dislocation annihilation (recovery) after some time [32, 72].

- Stage II: The constant creep rate ($d\epsilon/dt$) is caused by the balance between the recovery process (i.e. decrease in material's strength ($d\sigma/dt$) and work hardening ($d\sigma/d\epsilon$), given that $d\epsilon/dt = (d\sigma/dt)/(d\sigma/d\epsilon)$. Meaning, that the rate of dislocation annihilation is fast enough to match the rate of the increasing dislocation density [72].

- Stage III: The increase in creep rate is partially due to the recovery rate dominating the work-hardening rate. This is mainly caused by cross slip of screw dislocations. This cross slip allows screw dislocations to circumvent obstacles, and enhances a dislocation slip length. At high temperatures, the cross slip process is accompanied by grain boundary sliding, as well as, the enhanced mobility of vacancies, which help dislocations to pass over obstacles. The significant reduction of the cross-sectional area of a test sample (i.e. an increase in the true applied strain) and the formation of grain-boundary cavities also contribute to the acceleration of the creep rate. The end of Stage III, the sample fracture, is usually associated with sample necking in combination with grain-boundary cavity growth and coalescence [32, 72].

The shape of the creep curve depends on the applied constant stress and the imposed temperature. These creep curve changes are depicted in Fig. 2.2. From Fig. 2.2a it can be concluded, that the instantaneous strain increases with increasing applied stress and temperature and that the time to failure is reduced. From Fig. 2.2b it can be concluded, that the duration of the steady-state creep rate stage decreases with increasing applied stress and temperature.

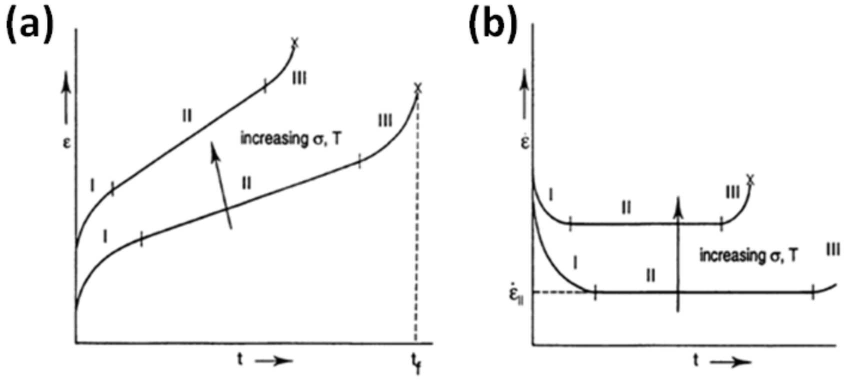

Figure 2.2: (a) Schematic representation of a creep curve and its alternations when σ and T increase, t_f indicates time of fracture. (b) Schematic diagram of creep rate as a function of time and its alternations when σ and T increase. $\dot{\varepsilon}_{II}$ indicates the secondary creep rate [32].

The interrelations between stress, temperature, strain rate and stage ratios depend on physical parameters such as, for instance, grain size, stacking fault energy, and shear modulus of the crystal lattice. The influence of different parameters on creep deformation depends on the prevailing creep mechanisms. The following Equation 2.1 (known as the power-law creep equation), containing physical parameters and constants to be obtained by fitting to experimental data sets, has been shown to give a decent first order estimate of the creep rate as a function of stress, temperature and grain size, as well as, the activation energy of the dominant deformation mechanism [32, 72, 82].

$$\dot{\varepsilon}_{SS} = C \cdot d^{-m}\sigma^{n} \exp\left(-\frac{Q}{RT}\right), \tag{2.1}$$

where C is a material constant that dependents on material's microstructure and particular creep mechanism, Q is the activation energy for creep, m is the grain size exponent, n is the stress exponent, σ is the applied stress, d is the grain diameter, R is the gas constant and T is the applied temperature.

2.2. Creep deformation mechanisms

As stated before, creep deformation is governed by different mechanisms, and the balance between them depends on the most dominating microstructural processes and specific thermomechanical parameters. In general, creep mechanisms can be divided into two categories:

1. Solid state diffusion dominated creep

2. Dislocation motion dominated creep

Grain boundary sliding has been proposed as the third independent creep mechanism [31]. However, it has been concluded by Raj and Ashby [68], that the accommodation of grain boundary sliding involves both diffusional creep and/or plastic flow by dislocation motion. Therefore, grain boundary sliding cannot be present without at least one of the other two microstructural processes governing creep deformation. Despite the fact, that grain boundary sliding is described separately in this section, strictly speaking, it should not be regarded as a separate creep mechanism.

2.2.1. Solid state diffusion dominated creep

This creep mechanism takes place under the conditions of high temperature-low stress or low temperature-high stress [23]. Then, the creep strain is governed by the movement of individual atoms as a result of the generation and propagation of vacancies [2]. The driving force for the movement of matter is the difference in the chemical potential of vacancies in the grain interior and those located in grain boundaries. Depending on the local conditions, the grain boundaries are either sources or sinks for vacancies (or interstitials) [67].

Nabarro-Herring creep

The mechanism is also known as bulk diffusion creep. It takes place at combination of a high temperature (nearing the melting point) and low stresses, when a metal starts to show Newtonian viscous flow. Meaning, that the deformation is governed by diffusional motion of atoms and vacancies across the grains, i.e. the crystal lattice. The motion of atoms and vacancies is stress-directed. In this mechanism, steady-state creep rate is linear and directly dependent on the applied load and motion of vacancies through the lattice [35, 59, 63, 85]. Therefore it can be written that [33]:

$$\dot{\varepsilon}_{SS} \propto \frac{\sigma D_V}{d^2}, \tag{2.2}$$

where σ is the applied stress, D_V is the volume/bulk diffusivity of the crystal lattice and d is the diameter of a grain.

Coble creep

This mechanism is also known as grain-boundary diffusion creep and it is based on diffusional motion of vacancies, which primarily travel along grain boundaries. It has been noticed, that such a motion is enhanced, when the applied stress is increased and/or the high temperature is slightly reduced (below 0.7 T_m). The motion of vacancies along grain boundaries is stress-directed. In this mechanism, steady-state creep rate is also linear and directly dependent on the applied load and motion of vacancies across grain boundaries [36, 55], and can be written [33]:

$$\dot{\varepsilon}_{SS} \propto \frac{\sigma D_{GB}}{d^3}, \tag{2.3}$$

where D_{GB} is the grain-boundary diffusivity.

As it can be observed from Equation 2.2 and Equation 2.3, the grain size has a strong influence on diffusional mechanisms of creep. This grain size dependence is more pronounced in Coble creep than in the Nabarro-Herring creep because of the extensive diffusion of vacancies along well-oriented grain boundaries. A schematic comparison between vacancy flow in Coble and Nabarro-Herring creep mechanisms is depicted in Fig. 2.3.

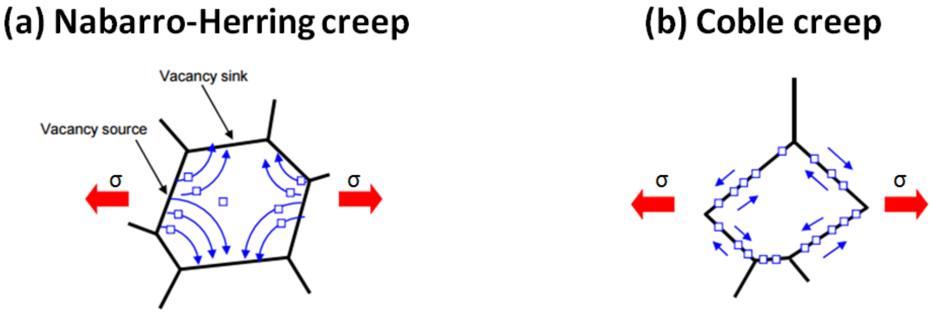

Figure 2.3: Schematic representation of the vacancy flow in (a) Nabarro-Herring creep mechanism – bulk diffusion, and (b) Coble creep mechanism – grain-boundary diffusion. Vacancies are represented as blue-framed squares and their direction of flow is depicted with blue arrows. The direction of the applied stress σ is indicated by red arrow [34].

2.2.2. Dislocation motion dominated creep

Dislocation creep can take place over a very broad range of applied stresses and temperatures. It comprises of mechanisms such as dislocation glide and climb, and both are usually assisted by vacancy diffusion. Dislocation glide describes the dislocation movement through a crystal lattice, when the dislocation core moves along a slip plane, stepping one Burger's vector distances at a time. This form of dislocation movement will continue until they reach grain boundaries and annihilate or when the dislocations encounter obstacles, in a form of particles or other dislocations. The obstacles prevent further dislocation motion and to overcome them, an additional assisting process is required, which is the vacancy diffusion. Vacancies help the dislocations to climb over obstacles, by means of vacancy-atom exchange and jog formation, allowing further dislocation glide. However, the dislocation climb requires the application of more energy than dislocation glide, as the equilibrium concentration of the vacancies in the grain has to increase in order to enable the continuation of the dislocation movement. Therefore, for this process to take place a higher temperature is required [65]. As in the end every dislocation creep mechanism involves work-hardening (dislocation glide prevention) and recovery (dislocation climb and dislocation annihilation by vacancy diffusion), the secondary creep rate of dislocation creep can be written as follows [65]:

$$\dot{\varepsilon}_{SS} \propto D \cdot \sigma^n, \tag{2.4}$$

where D stands for the material's diffusivity and n is the stress exponent, which defines the contribution of dislocation mechanisms in the creep deformation. This value of the exponent is larger for dislocation dominated deformation (usually between 3 and 10) and lower for diffusion dominated deformation (between 1 and 2). The lower experimentally observed stress exponent n, the larger the contribution of diffusion processes in the overall creep deformation.

2.2.3. Grain boundary sliding

Grain boundary sliding takes place due to shear stresses being generated between individual grains loaded under a common far-field imposed uniform tensile (or compressive) stress. These shear stresses cause the grains to slide along each other via their boundaries. In the case of the dislocation dominated creep, the dislocations on grain-boundary planes can cause grains to slide. However, this process requires very high stresses and the likelihood of it occurring highly depends on the grain size, grain boundary surface area, and grain boundary orientation and type [29]. Therefore, grain boundary sliding is usually more often encountered in (and by many scientists assigned to) the diffusion creep conditions. During diffusion creep, the diffusional flow of matter in the boundaries (between the regions under tension and compression) accommodates the sliding process. While relatively low stresses are sufficient, a high vacancy concentration and a high diffusion rate are required for the process to be effective [73].

2.3. Creep damage mechanisms

Creep in its tertiary stage ends with a rupture of the test piece or the installation. This final failure develops gradually over time and can be governed by different mechanisms, called creep damage mechanisms. This section focuses on the relevant mechanisms of damage and their dependence on stress and temperature. Whatever the mechanism, every creep failure events starts with the nucleation of local damage, before the damage will grow at later stages of the process. Therefore, firstly, creep damage initiation will be described.

2.3.1. Damage nucleation

Cavitation, i.e. the formation of pores not containing a gas or other matter, is initiated on grain boundaries by one of the two modes of nucleation: atomic bond breaking or vacancy condensation. Atomic bonds can break at weak interfaces, but almost exclusively if the grain boundary contains a high concentration of weakly bound solute atoms and it is not often encountered during high-temperature deformation. Therefore, cavity nucleation by vacancy condensation is regarded as a more common damage nucleation mechanism during creep as it appears in high temperature conditions. In such a mode, cavity nucleation is highly dependent on stress and temperature application [61]. A significant stress level is required, as a large stress concentration needs to be introduced locally in the material before cavities can start nucleating. On the other hand, a high temperature is required to allow rapid diffusion of vacancies to and along the grain boundary if the grain boundary is to be opened up to create a damage.

Although cavity formation can, in principle, take place at any place along the grain boundary, grain boundary junctions, as well as, grain-boundary inclusions and impurity particles are preferred locations for cavities to be formed. The actual nucleation rate also depends on the nature and the inclinations of the grain boundary. Grain boundary can create a hole at grain junctions or a ledge on an inclined single grain boundary (to the stress direction), as well as, cause incohesion between the lattice and a grain-boundary inclusion or an impurity particle. The exception is a void created at grain boundaries located exactly perpendicular to the stress direction, for which grain boundary sliding will not occur. Such nuclei are assumed to be due to a dislocation pile-up that breaks through from the grain into the boundary. This nucleation mechanism does not require a diffusional transport of vacancies, unlike the mechanisms governed by grain boundary sliding.

However, the application of a stress remains required in order to cause the dislocation movement leading to dislocation pile up at boundaries [46, 61, 69]. A schematic depiction of these nucleation mechanisms is presented in Fig. 2.4.

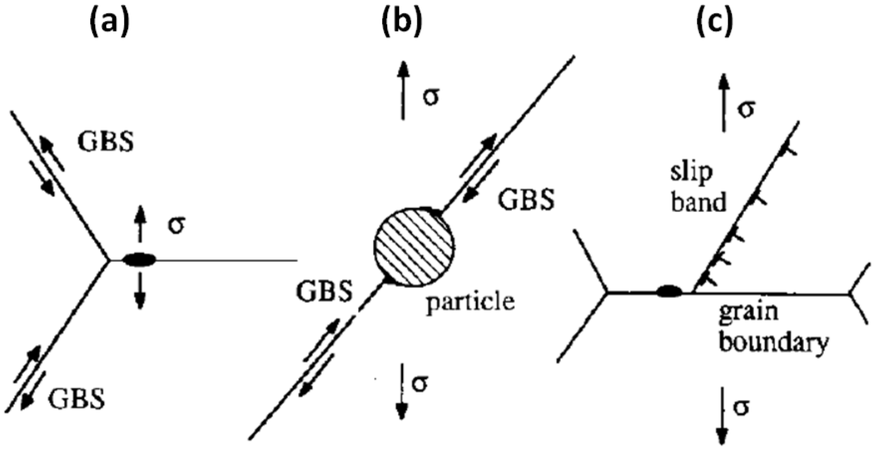

Figure 2.4: Schematic representation of (a) cavity nucleation at grain-boundary triple-junction caused by the grain boundary sliding (GBS) mechanism, (b) cavity nucleation at grain-boundary impurity particle (or inclusion) caused by the grain boundary sliding mechanism, and (c) cavity nucleation at a single grain boundary transverse to the applied stress σ caused by dislocation pile-up [61].

2.3.2. Damage growth

Given that the creep deformation continues after cavity nucleation, the damage can grow by one of the following mechanisms. The mechanism governing the particular cavity growth is associated with temperature and applied stress, under which the creep deformation takes place. Diffusive cavity growth is usually associated with high temperature-low stress conditions, while plastic flow cavity growth is usually assigned to low temperature-high stress conditions.

Diffusive cavity growth

The cavities which are wide apart on a grain boundary grow solely by diffusion. During this growth atoms are transported from the surface of the cavity to the grain boundary, which the cavity lies on. Then, the atoms are deposited there and their entire transport from the cavity surface is controlled by either grain boundary diffusion or surface diffusion. The slower of these two processes controls the cavity growth. When grain-boundary diffusion controls the growth, the cavity sustains its equilibrium shape due to the rapid surface diffusion. In other words, the atoms are deposited faster at the surface of the cavity than they are removed from the tip of the cavity by grain-boundary diffusion [61]. If the cavity growth is controlled by surface diffusion, the void takes the shape of a crack-like cavity, which is regarded as its non-equilibrium shape (see Fig. 2.7) [62]. The diffusive cavity growth is also further enhanced by the diffusion of vacancies to the cavity surface from bulk and grain boundary, but its influence on the shape of the growing cavity is considered to be negligible, as the vacancies tend to diffuse back and forth [75]. The equilibrium shape of a cavity is presented in Fig. 2.5, which also presents a schematic representation of a diffusive cavity growth.

Creep-enhanced cavity growth

Once nucleated, grain-boundary cavity can also grow solely by the creep deformation. Meaning, that its growth is governed by power law creep as a result of the surrounding stress field in the bulk, adjacent to the cavity [49]. However, this mode of cavity growth is only possible when there is no vacancy flux in the material, which is an unrealistic condition at elevated temperature. Therefore, it is more realistic to assume that creep-enhanced growth takes place as a result of coupled diffusion and plastic mechanisms. In such a case, the diffusion mechanism contributes to the expansion of damage within a certain region, defined by a characteristic diffusion length Λ (see Fig. 2.6). Outside of it, the cavity growth is governed by power law creep deformation. Creep can accelerate the diffusional cavity growth by decreasing the length Λ, which takes place at high applied stresses and strain rates [61]. A comparison between the creep cavity growth controlled by diffusion and by creep (plastic) flow is depicted in Fig. 2.8. Finally, the cavity growth can be enhanced by pre-existing grain-boundary cavities (nucleated earlier), which propagation is controlled by the stress fields (increased stress concentration at the cavity tip) of the adjacent cavities, that lie on the same grain boundary [49].

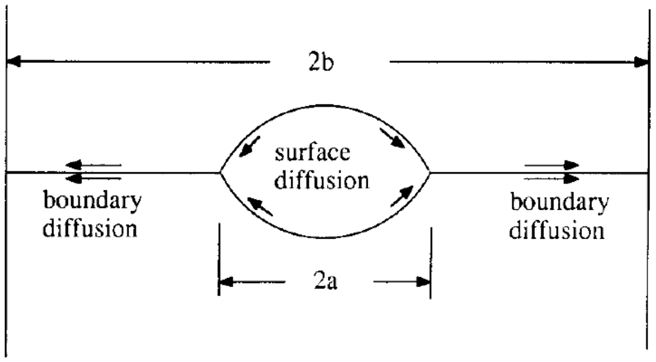

Figure 2.5: Schematic representation of a diffusive cavity growth controlled by grain boundary diffusion (equilibrium cavity shape), where *a* stands for the radius of the cavity and *b* for the radius of the box of interest [61].

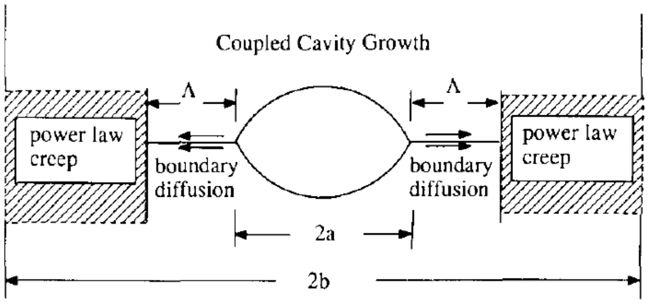

Figure 2.6: Schematic representation of a coupled diffusion-plastic cavity growth. Λ is the characteristic diffusion length, which defines the region of diffusive cavity growth, *a* stands for the radius of the cavity and *b* for the radius of the box of interest [61].

Additionally, the shape of the cavities during growth can be strongly influenced by grain boundary sliding. However, grain boundary sliding itself does not affect the volumetric growth the cavity [62]. The shape change of the cavity before and after grain boundary sliding, at an inclined (to the applied stress) single grain boundary is depicted in Fig. 2.9. Furthermore, the cavity growth is also affected by the polycrystalline nature of the most technical metals. Therefore, the growth of the cavity can be constrained or unconstrained. Constrained creep cavity growth is caused by the creep flow in the surrounding grains. When the cavity propagation is faster than creep deformation, the redistribution of stress in the solid occurs, which leads to heterogeneous distribution of cavities in the material. This means, that cavities are not evenly distributed on grain boundaries, and a situations where there are many cavities along one grain and none along another can be encountered [62]. The unconstrained creep cavity growth takes place when both normal and shear stresses are applied on cavitated grain boundaries. The shear stress causes the grain boundary sliding effect, which further establishes a homogeneous spatial distribution of cavities in the material [62].

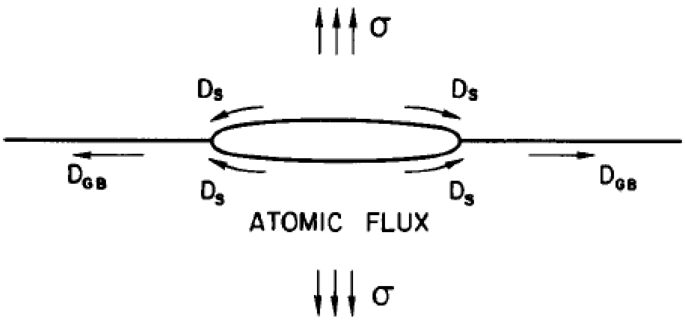

Figure 2.7: Schematic representation of a non-equilibrium shape of a cavity during diffusive creep cavity growth [62]. Arrows indicate the applied stress (σ) direction, while the D_S and D_{GB} arrows along the cavity and the boundary indicate the direction of surface diffusion and grain-boundary diffusion, respectively.

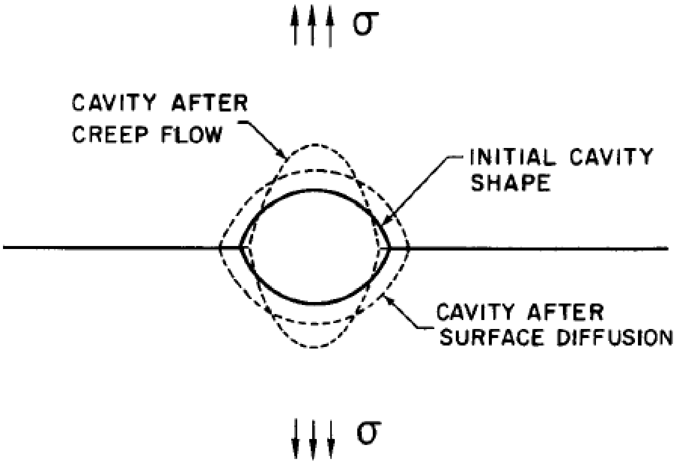

Figure 2.8: Schematic representation of the influence of the diffusive and creep cavity growth mechanisms on the shape of the cavity [62]. Arrows indicate the applied stress (σ) direction.

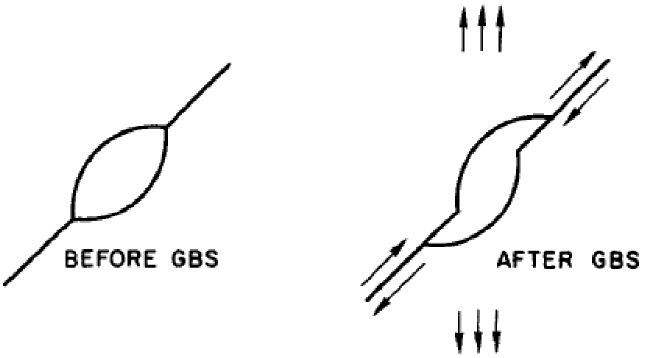

Figure 2.9: Schematic representation of the influence of grain boundary sliding (GBS) on the cavity shape [62]. Arrows indicate the the normal and shear stress directions.

2.4. Creep failure

The propagating cavities, controlled by any of the aforementioned growth mechanisms, eventually coalesce with one another, creating micro- and macro-cracks. The final fracture can take place according to different modes, depending on the ductility of the metal. These modes are presented in Fig. 2.10:

- Intergranular creep fracture (by voids and wedge cracks): This fracture mode is observed when the applied stress is relatively low. It is controlled by grain boundary sliding and/or wedge and crack formation along grain boundaries normal to the applied stress [4, 27].
- Growth of voids by power-law creep (transgranular and intergranular): Fracture takes place due to the diffusional growth of voids along grain boundaries or inside the bulk material [4, 27].
- Rupture due to dynamic recrystallization: This fracture is usually connected with dynamic recrystallization of the material. As a result of the local transient softening the deformation is highly localized leading to an extreme reduction of the cross-section [4, 27].

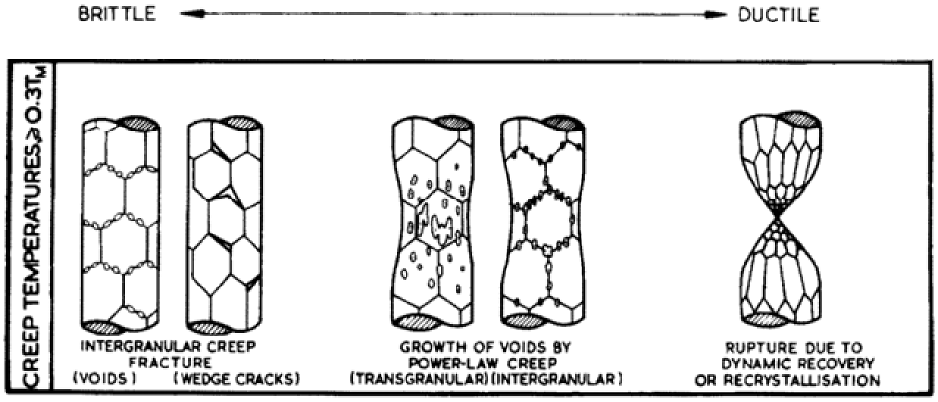

Figure 2.10: Schematic representation of fracture mechanisms for fcc metals and alloys. The sequence of mechanisms is ordered according to the brittleness/ductility of a metallic material [4].

2.5. Prevention and control of creep damage

As the creation and growth of local creep damage is the most important aspect controlling creep life time, many researchers have tried to come up with the solution to retard or control the formation and growth of creep cavities. One of the approaches is connected with the composition of the steels, which can be alloyed with other metallic elements and brought to a solid solution state before the material is exposed to creep loading conditions. The solute atoms contribute to an increase in strength and a delayed damage nucleation by weakly pinning the moving dislocations. Similar approaches consider precipitation hardening, which constrains the dislocation movement due to the presence of precipitated carbides, nitrides or intermetallics, or grain boundary hardening, which involves tempering treatments of steels that lead to the formation of laths and blocks in the microstructure of a material, delaying the creep deformation [1, 54]. These mechanisms can certainly work, but the introduction of discrete microstructural entities such as precipitates and (strong) grain boundaries also leads to the introduction of stress concentrations, which do favour the formation of cavities. Whatever the approach, they have in common that they aim to prevent the formation of cavities rather than to make any formed cavity more harmless. The latter approach has been demonstrated in a laboratory experiment in which creep loaded samples were ex-situ post-sintered to remove the porosity [30]. Of course such a strategy is non-realistic for real technical constructions. Finally, a completely new, innovative and attractive approach for creep damage control has recently emerged, which considers the autonomous filling of creep cavities by solute atoms, priory incorporated into the crystal lattice of alloys. This method is called self healing of creep-induced damages, and it requires significantly larger attention and description. The following chapter solely focuses on that intriguing mechanism of creep damage control.

3

Self healing

The creep damage mechanisms mentioned in the previous chapter will guide the development of a self healing strategy for creep damage in high-temperature metals. This approach is an alternative option for the conventional approach of damage prevention. The concept of autonomous damage healing appears to be an attractive option as it takes into account the eventual damage presence in the materials and deals with its control by full or partial repair, resulting in an elongated lifetime of structural elements. This chapter aims to exemplify this innovative concept by describing its principles and requirements in order to have a greater understanding of the mechanism applied in the actual research reported in the next chapters. The chapter ends with present applications and future prospects of self healing implementation in metallic materials, which sums up the accomplishments that were and can be achieved in the field of damage control in metallic materials exposed to high temperatures and serious stresses for extremely long times.

3.1. Self-healing requirements

Self healing materials should not be perceived as newly developed materials, but rather as materials that are modified in a way to possess a new functionality, which enables them to autonomously (or with a small stimulation) restore their initial properties, for instance, strength or stiffness [79]. In order to alter an already existing material type to make it self healing, a set of requirements has to be followed [78, 79]:

1. The process of the damage healing has to take place with a relatively high rate, i.e. damage creation cannot outweigh the filling process, otherwise the self healing does not serve its purpose of performance elongation.
2. The material, after modification, has to perform regular mechanical functions, that were assigned to it before alternations.
3. Ideally, the process has to be able to perform multiple successive healing actions at the same location.
4. Ideally, the process can heal a damage of any given size.
5. Ideally, the damage of the material is complete.
6. Ideally, the process has to be autonomous, i.e. does not require any external intervention.
7. Ideally, the self healing material has to have the same properties as the material before modification.
8. Ideally, the self healing material should cost less or at least not a lot more than the pre-modified material.
9. Ideally, the process makes the material forever-lasting, i.e. there is no need for the replacement of a structural element made of a self healing material.

Some of the above-mentioned requirements consider ideal cases, which are most of the time hard to achieve. This is due to the sheer constrains imposed by the intrinsic material chemistry and resulting physics, which cannot be modified to certain extends as their atomic/molecular/bond structure are not so easily manipulatable. However, even a self healing process which only delivers a "minimal" healing action, but contributes to the increase in material's lifetime in the case of accidental or expected localised damage, is considered to be serving its purpose [78, 79]. The minimal requirements that a self healing material has to possess impose, that the material: (i) can have a significantly extended lifetime in the case of an accidental (non-fatal) damage, (ii) can perform at least one self healing event, (iii) only needs weak external factors to be activated, (iv) heals defects up to a specific size (called a critical size of damage), (v) heals the damage only partially, (vi) decreases slightly the properties of the material and (vii) costs a bit more than its non-self healing counterpart. As long as these minimal properties are satisfied, a material can be regarded as self-healing because the generic purpose of the autonomous repair is not to maximize the performance of the material, but that of the final product. The product performance increases as long as the embedded self healing ability does not adversely effect the entire material system [78, 79]. A schematic plot of performance versus lifetime for four cases is presented in Fig. 3.1. From Fig. 3.1 it can be observed, that an original material can indeed be improved by traditional approaches and still perform longer than the reference base material. Moreover, it can be seen, that self healing causes periodic increases in materials' performance, which the original or traditionally improved approach cannot do. Finally, a comparison between a minimal and ideal self healing approach can be seen, which shows what can be achieved if the self healing field is further explored and advanced.

3.1.1. Self healing scheme

In order to incorporate a self healing ability into any material, a general scheme has to be followed. To introduce a self healing ability in a material, a certain fraction of atoms/molecules has to be set aside, which may later contribute to the performance recovery upon damage (see Fig. 3.1), but does not enhance any of the material's initial properties or most likely even lowers the initial mechanical properties of a material. Moreover, it has to be made sure, that not only there are enough atoms and atomic configurations, which are set aside to realize healing of damage, but also that there are enough atoms left that give the material desired mechanical properties [78, 79].

The "healing agents", responsible for the performance elongation of the material, have to be able to move to the damage site and when they are present there, they have to be able to fill the space and stay at the spot. Furthermore, they have to bond with the surface of the damage, otherwise they would not contribute to the local restoration of the load-bearing capabilities. Thus, the self healing scheme has to take into account a solution involving a local temporary mobility in a rigid material, which is halted as soon as the damage-filling is completed. To facilitate crack healing, it is important that the surfaces of the damage stay in relatively close contact with each other and are kept in a fixed position during healing actions. This implies that the damage propagation cannot take place during healing or the healing has to be spontaneous enough [78, 79].

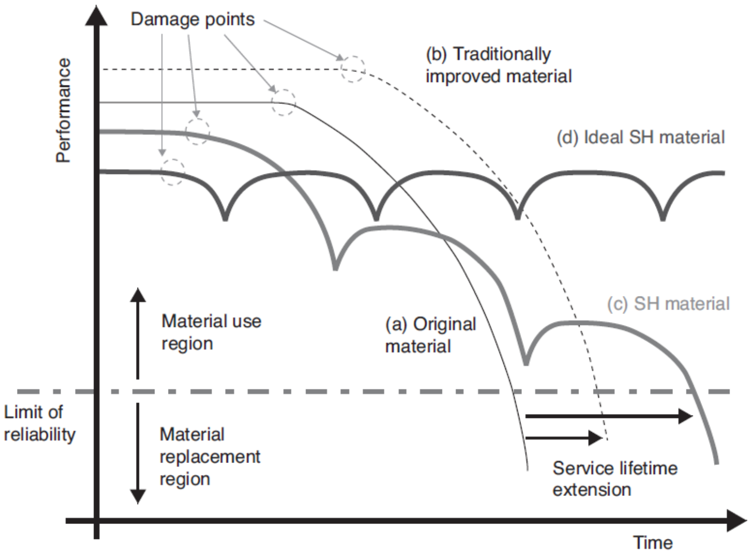

Figure 3.1: Schematic plot of performance versus service lifetime for four different cases of materials: (a) original material, (b) traditionally improved material, (c) (minimal) self healing (SH) material and (d) ideal self healing material [28].

In summary, the general self healing scheme (quasi-) autonomous healing of structural materials can be formulated as follows [30]:

1. Self healing agents are added into the material (or a fraction of a material is transformed into self healing agents), which has to be performed homogeneously. Meaning, that this action does not jeopardize the structural integrity of the entire material.
2. The agents are delivered autonomously or with slight stimuli under full or slightly reduced operating conditions of the material.
3. The defects are healed by reactions taking place under full or slightly reduced operating conditions.

3.2. Self-healing mechanism in steel

Since the subject of this work are Fe-based creep-resistant alloys, the self healing principle and scheme for steels are introduced hereafter. Firstly, the general scheme that was described in the previous section can be adapted as follows [30]:

1. Solute elements with healing functions have to be introduced in the crystal lattice of the metallic material by the means of solid solution heat treatment and quenching.
2. Solute atoms have to be delivered autonomously to the defect sites through volume and/or grain boundary diffusion during high temperature exposure and constant loading (creep conditions).
3. Solute atoms have to segregate preferentially on cavity surfaces and subsequently precipitate into second phase, binding with the crystal lattice. The precipitates heal the damage by closing it.

In order to implement the above-mentioned concept, the kinetic and thermodynamic requirements of solute transport by volume and grain-boundary diffusion into open-volume defects have to be considered, which is the aim of the following subsection.

3.2.1. Self healing of creep-induced damage by solute diffusion

As mentioned in the chapter, the nucleation and growth of grain-boundary cavities during creep is inevitable as the deformation progresses. It has been proven that creep cavity growth takes by diffusive transport, which leads to the intergranular creep fracture, is the most frequently encountered creep damage mechanism in creep-resistant steels under ordinary service conditions [30]. Therefore, the self healing ability has to be focused on this kind of damage.

The fact that the cavity growth takes place by the combined action of diffusive transport of matter from creep cavity surface to grain boundary, and vacancy diffusion, has already been mentioned in the previous chapter. Therefore, using the phenomenon of self-diffusion (which also governs the vacancy diffusion), a self healing mechanism that relies on the diffusion of matter into the cavity can be introduced [66, 87]. By doping steels with appropriate alloying elements, a solute transport of matter to the cavity surface can be achieved, provided that the alloying element atoms can be put in an initially supersaturated state. The solute atoms in their supersaturated state are triggered to move toward the cavity surface by the combined action of volume and grain boundary diffusion. The main driving force for the diffusional transport of matter into the cavity surface is the reduction of system's energy, which comprises of the following driving forces: (i) the chemical potential provided by a supersaturation of solute, (ii) grains in strain and (iii) surface energy for precipitation located at creep cavities. These driving forces can facilitate a higher diffusion rate of solute compared to the vacancy diffusion and atomic transport that cause the cavity growth. This is also enabled by the fact that solute atom transport is enhanced by dislocations, which attract impurities and diffuse them to the grain boundaries and open-volume defects (dislocation diffusion). Moreover, the high rate of solute diffusion can be accomplished by localized high diffusivity paths present in the material, such as grain boundaries and free surfaces [30, 51, 71, 87]. Once the solute atoms are segregated to the damage sites, they start to form precipitates or other 2nd phases, which are interfacially bonded to the matrix.

For the healing to be efficient, it has take place during the early stages of the cavity growth and at the appropriate rate. If the solute depletion is too slow, the cavity can growth and/or coalesce to the size which cannot longer be fully prevented. This fact suggests that there is a critical size of a cavity that can be healed upon the transport of solute for every self healing system [87].

In summary, the main requirements for the self healing process in creep-resistant steels are as follows [87]:

1. High mobility of the solute in the material (at the prevailing temperature and stress).
2. Driving forces towards the damage site (provided by damage itself, the supersaturated state of material and applied stress).
3. Free surface of cavities (provided by damage formation) that acts as a trigger for precipitation.
4. Sufficient interfacial precipitate-matrix bonding (provided by prior studies on bonding between solute and solvent atoms).
5. High healing rate compared to damage propagation rate (provided by driving forces, dislocations and high-energy paths).
6. Sufficient reservoir of healing solute atoms within the matrix (provided by the composition of the material).

Additionally, one extra requirement has been incorporated into this scheme, which is the **site-selective precipitation**. This requires a high energy barrier for homogeneous precipitation of solute, which is directly connected with the atomic radii of solute and atoms constituting the matrix. Once the solute atoms have a larger size than solvent atoms, this barrier is provided. This requirement has been added to the scheme after the work on Fe-Cu alloys, which show a high amount of bulk precipitates as Cu atoms and Fe atoms are comparable in sizes [39, 40].

An illustrative scheme of a self healing effect, that complies with all the above-mentioned requirements, is depicted in Fig. 3.2, where a propagation of a creep-induced cavity on a single grain boundary, located transversely to the applied stress, is described. In reality, all the aforementioned steps in Fig. 3.2 take place simultaneously once the cavity is nucleated. Meaning, that the solute transport does not start at larger crack opening, but is activated by any open-volume defect in the material.

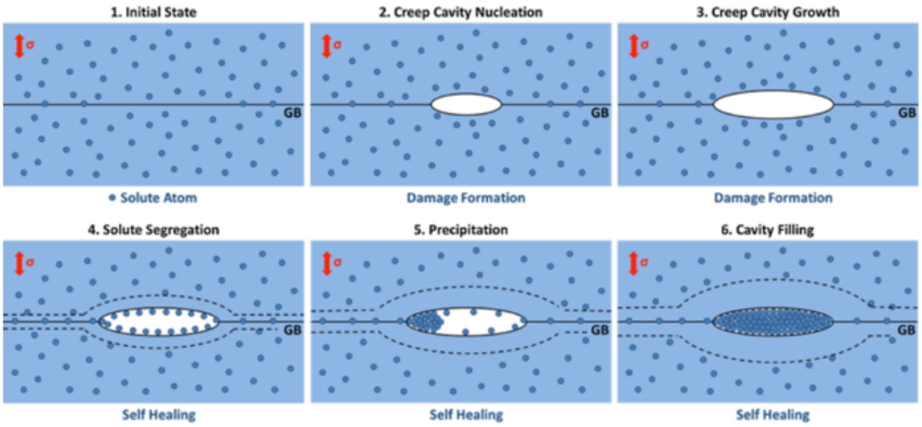

Figure 3.2: Schematics of the self healing effect at a creep-induced cavity, located transveresely to the applied stress (σ): (1) nucleation of a creep cavity at a grain boundary, (2) and (3) growth of the cavity, (4) solute diffusion towards the surface of the cavity and its segregation, (5) and (6) filling of the cavity with solute atoms. Around the cavity and the adjacent grain boundary, a solute depleted zone is marked (dashed lines) [87].

3.3. Applications and prospects of self healing steel

Creep-resistant steels are in a high demand in power plants, in particular in their structural parts like: rotors, blades, casings, casing bolts, pipework. In such installations, lower fuel costs and lower carbon-dioxide emissions are accomplished by increasing the steam conditions, i.e. by raising the temperature and pressure (up to 600°C and 160 bar, respectively) [57]. Creep-resistant steels are also exploited extensively in the aerospace industry, where they serve as structural elements for aeroengines, utilized at even more severe conditions as they deal with higher temperature (even up to 1000°C) and forced cooling [7]. Self healing steels offer an elongated time of performance, which is connected with fewer replacements of these structural parts. This eventually leads to the energy savings due to the lack of recycling of the scrap elements, and economical advantages for the industries, which can allocate a smaller budget for the substitutional parts and their service. The service conditions of steam turbines and aeroengines are perfect for the autonomously healed steels. Thanks to this harsh environment they can thrive in their performance, inducing the healing ability on the service damage. The healed damage not only elongates the lifetime of the structural parts, but also reduces the material's deformation. This means, that the increasing strain can be halted by healed creep cavities or the strain rate can be lowered by the damage filling. The problem of the progressing deformation particularly affect the blades of aeroengines, which after straining can rub against the casing that leads to malfunction or catastrophic outcomes during service [33].

The most important matter is that self healing steel is no longer a material, but a system, which develops its functions during worktime. The solid solution heat-treated self-healing steels are relatively ductile and they tend to show lower strength at the beginning of their deformation, compared to traditionally manufactured creep-resistant steels. However, as the deformation proceeds, the solute atoms contribute to the strength increase by (i) dislocation pinning, (ii) by dynamic precipitation at damage sites and (iii) by the reduction of precipitation coarsening, which ultimately leads to the longer times when the material possesses an adequate strength, ductility and shows an overall reliable performance, compared to the traditionally improved steels [33]. Number of researchers have conducted projects on the self healing effect in steels and showed that there are multiple compositional options that can serve as autonomous repair systems. The creep deformation studies of austenitic stainless steels doped with traces of boron and nitrogen [30] have shown that the segregation of B to the cavity surfaces leads to the precipitation of boron nitrides, that fill up the creep damage. Furthermore, the precipitation of BN particles not only fills the volume of the damage, but causes a complete cessation of the creep cavity growth, which was assigned to the high melting point of the particles (around 3000°C) and a strong precipitate-matrix interfacial bonding. Such findings show the prospects of the self healing effect in steels, which can be possibly achieved in many more grades of steel, with further research and experimental investigation [87].

Systematic experimental investigations of self healing in iron-based alloys has been conducted most extensively by researchers from the Delft University of Technology, who elaborated this subject on Fe-Au, Fe-Cu and Fe-Mo alloys. They have demonstrated that Fe-Au at elevated temperature and constant loading conditions shows an effective autonomous healing capabilities. Fe-Au alloys resulted in high filling ratios of creep-induced cavities (up to 80%) and its precipitates immobilized the growth of voids prior to their coalescence, which proves that the solute transport to damage takes place at a high rate in the early stages of deformation [87]. Moreover, the work on Fe-Cu alloys showed the enhancement of the creep lifetime in solutionised alloys compared to the same alloys in which the solutes were effectively immobilised by a precipitation treatment prior to the actual creep testing [39, 40]. Then, the Fe-Mo alloys that they investigated showed an enhanced creep lifetime, due to the dynamic precipitation of the Laves phase at the creep-induced damage [89].

All in all, the outcomes portray a great potential connected with the substitution of creep-resistant steels with self healing steels, but at the same time, it is clear that the ideal composition to get a proper combination of good mechanical properties on an absolute scale and a significant life time extension by the autonomous and timely healing of creep loading induced damage has not been reached yet. The project on damage formation and healing in Fe-W model alloys presented in this Thesis aims to contribute to the database required to define the optimal creep steel composition.

4

Self-healing of creep-induced cavities in Fe-W alloys

Tungsten is essentially known for its high strength and yield point at elevated temperature, and its high creep resistance. When combined with iron, the Fe-W alloys do not only show the enhancement of aforementioned properties, but also show a higher melting point and heat resistance capacity [53, 76]. The precipitation of the $(Fe,Cr)_2(Mo,W)$ Laves phase has been discovered in high-Cr steels, that contained traces of Mo and W after a long elevated temperature exposure. Tungsten thereby shows precipitation capabilities in the iron lattice, which can serve as a repairing mechanism in high-temperature alloys [89].

By comparing Fe-W alloys to the Fe-based alloys which were investigated in the self healing capability (metioned in the previous chapter) it can be said, that the Fe-W alloys are characterized by a better solid-solution strengthening than Fe-Mo alloys, which makes them a better choice for creep resistant alloys. On the other hand, the diffusivity of tungsten is slightly lower than that of molybdenum in the bcc iron matrix, which can be a limiting factor for Fe-W self healing [76, 89]. All in all, Fe-W is expected to show a self healing performance that is nearly as efficient as Fe-Au alloys, which showed a preferential precipitation at creep-induced grain-boundary cavities and a significant cavity filling, that increased with the increasing volume of defects [24].

The aim of this chapter is to evaluate the results of the second phase precipitation as a self healing mechanism at creep-induced damage in the binary Fe-W alloys by means of various experimental and computational techniques. This chapter commences with the details of the Fe-W alloys design, which is followed by the description of creep tests, used to induced damage and precipitation in the alloys, then, the experimental methods used to study the self healing effect in these alloys, i.e. scanning electron microscopy and X-ray tomography, are presented. The chapter is divided into separate sections with independent results for each of the undertaken experimental procedures. The chapter ends with conclusions on all the obtained results and recommendations for the future Fe-W investigations.

4.1. Design of the Fe-W alloys

In order to design an alloy for the purposes of this project, several factors had to be taken into consideration. First is the solubility of tungsten in bcc iron matrix. According to the literature, W is soluble in α-Fe up to 35.5 wt.% at the peritectic temperature of 1548°C. The literature also confirms that iron and tungsten form two stable intermediate phases (μ - Fe_7W_6 and δ - FeW) and an intermetallic phase - Fe_2W, known as the λ-phase or the Laves phase [53].

Secondly, before the alloys' concentration could be chosen, the atomic size factor in Fe-W had to be considered. When taking into account the precipitation of the second phase as a self healing mechanism, the preferable precipitate nucleation has to be examined in the chosen binary alloy. Of course, a heterogeneous, rather than homogeneous, nucleation of precipitates is desired in Fe-W alloys. A homogeneous precipitation in the bulk does not contribute to the healing of the induced damage. In order to find the favourable nucleation sites for precipitates in Fe-W, the total change in Gibbs free energy for nucleation of precipitates had to be elaborated. The equation is as follows:

$$\Delta G = \frac{4\pi}{3} r^3 (\Delta G_V + \Delta G_S) + 4\pi r^2 \gamma, \tag{4.1}$$

where ΔG_V is the change in chemical potential per unit volume, ΔG_S is the change in elastic energy density due to strain, γ is the interfacial energy and r is the nucleus radius [86].

When the solute atoms are larger in radii than the solvent atoms, the energy for the bulk nucleation of precipitates is significantly increased, due to the increase in elastic strain of the lattice (large ΔG_S). Such an energy barrier is too large for the solute atoms to form and grow nuclei in the bulk, and they start to migrate throughout the lattice to nearby lower energy sites. The lower energy sites for precipitation are dislocations, defects or grain boundary cavities. At these locations, the strain fields generated around the nuclei are changed, which leads to a decrease in the energy barrier for nucleation because of the decrease in ΔG_S. This reduction in Gibbs free energy, in case of precipitate nucleation on dislocations, can be approximated by [86]:

$$\Delta G_d = -4\mu b r_A^3 \epsilon / R_d, \tag{4.2}$$

where b is the Burgers vector, μ is the shear modulus, R_d is the distance of the nucleus to the dislocation core, r_A is the solvent radius and ϵ is the relative size difference of a solvent and solute atom radii, which is equal to

$$\epsilon = (r_B - r_A)/r_A, \tag{4.3}$$

where r_B is the solute radius [86].

The significant size difference between the radii is likely to promote heterogeneous precipitation, which can result in a self healing mechanism by precipitation at open-volume defects. The atom radius of W is bigger than that Fe in the bcc matrix. Their relative size difference is equal to $\epsilon \approx 10\%$.

4.1.1. Composition of the Fe-W alloys

When the heterogeneous precipitation in Fe-W alloys was established using the atomic size factor, the composition of the metallic samples designated for further testing could be chosen. In order to accomplish it, Fe-W binary phase diagram had to be studied. The diagram is depicted in Fig. 4.1 and was rendered using thermodynamic database by the ThermoCalc software. The concentration of tungsten in the samples had to be chosen taking into account the testing temperatures and the fraction of the second phase at these temperatures. The temperature of exposure has to adapt to the real service temperature of currently used industrial creep-resistant steels. Usually, metallic elements subjected to creep deformation during work operate in temperatures of around $\frac{1}{3}$ to $\frac{1}{2}$ of T_m. Furthermore, in order to investigate the second phase precipitation, a sufficient amount of this phase has to precipitate during temperature exposure, otherwise the results of healing might be unsatisfactory and prone to inaccuracy.

The Fe-W composition was calculated at the equilibrium of α-phase and $\alpha + \lambda$ phases for temperatures between 500 and 600°C (see Fig. 4.1). The results are presented in Table 4.1. It can be observed, that in order to obtain a the second phase precipitation in Fe-W alloys at elevated temperatures, their concentration of tungsten must be at least ~0.5 – 1 wt.%, depending on the given temperature range.

Table 4.1: Equilibrium phase concentrations of the Fe-W system in α-phase.

Temperature [°C]	Fe [wt.%]	W [wt.%]
500	99.51	0.49
550	99.30	0.70
600	99.03	0.97

Considering all the mentioned requirements and restrictions, two materials were chosen: Fe-4wt.% W and Fe-6wt.% W. The concentration of tungsten in Fe-4wt.% W corresponds to the tungsten supersaturation of 1 at.% (at 550°C) in this alloy and was chosen in order to establish a relatively high driving force for the solute atoms to fill and precipitate the grain-boundary cavities in the early stages of the alloys' creep deformation. On the other hand, the concentration of tungsten in Fe-6wt.% W corresponds to the tungsten supersaturation of 2 at.% (at 550°C) and was chosen to evaluate the influence of a higher driving force for solute precipitation, compared to Fe-4wt.% W, on the creep cavity filling. The higher tungsten concentrations were not chosen as the increasing W concentration in the Fe-W alloys increases the solutionizing temperature of the λ-phase.

The alloys were produced by Goodfellow. The received materials slightly differed in composition and contained traces of other elements, but they certainly fell into the category of high purity alloys. The exact chemical compositions of the two Fe-W systems determined by X-ray fluorescence (XRF) are presented in Table 4.2. The fact that the alloys were of high purity was advantageous for the precipitation behaviour of the Laves phase in the materials. High-purity alloys lack the precipitation of other particles, like carbides (such as $M_{23}C_6$ or MC) or nitrides, which hinder the precipitation of the second phase.

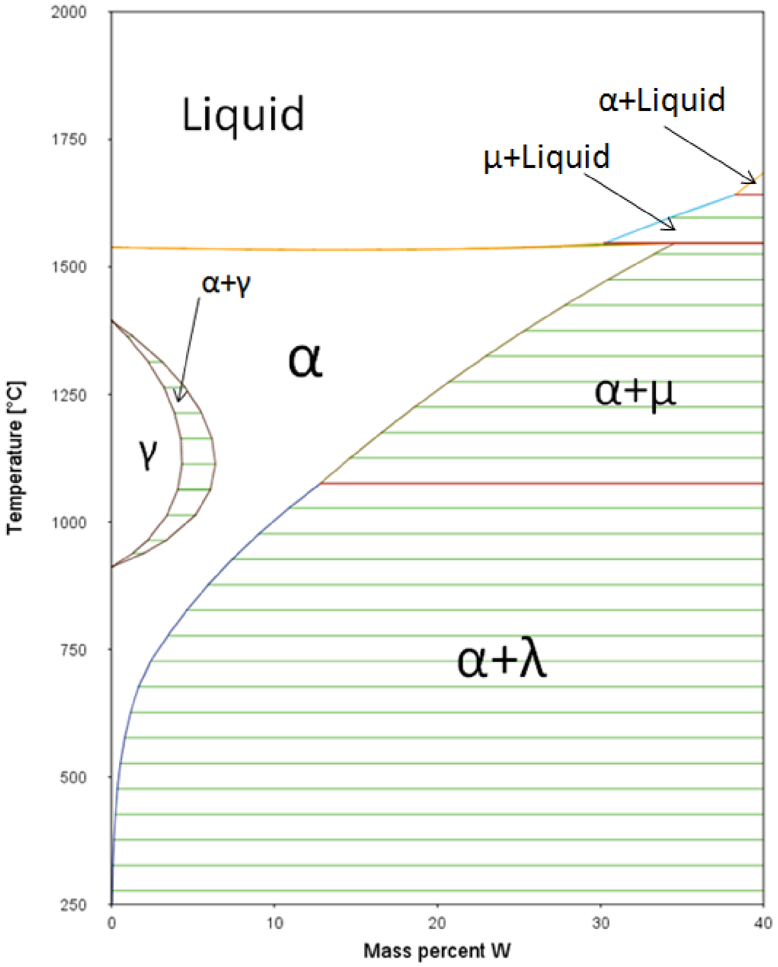

Figure 4.1: Phase diagram of Fe-W obtained from the Thermocalc software. The depicted concentration of W is chosen to present the full range of tungsten solubility in iron (0 – 35.5%). Phases: α - ferrite, γ - austenite, λ - Laves phase, μ - stable intermediate phase of Fe_7W_6.

Table 4.2: The chemical compositions of the chosen Fe-W alloys [wt.%].

Alloy	W	Si	S	Zn	Fe
Fe4W	3.800	0.020	0.026	0.195	Balanced
Fe6W	6.013	-	-	-	Balanced

4.2. Sample preparation

When the alloys were ordered and delivered, they were received in sheets of dimensions 10×10×0.5 mm, in height, width and thickness respectively. Subsequently, they were machined by spark erosion into small dogbone-shaped samples. The shape of the sample with its dimensions is depicted in Fig. 4.2. The motivation for choosing such a shape of specimens has to do with the desired failure site, which is the region with a reduced uniform cross-section of the dogbone-shaped sample. The curved profile of the "dogbone" concentrates the applied stress locally at the edges of the gauge section. Additionally, the smooth fillets do not cause stress concentrations in the transition zones, which allows the specimens to fail in the gauge section during tensile deformation. The purpose of the blank holes in the samples is connected with their mounting procedure inside the creep tester. It has been proven, that the locally raised stress concentration at the hole edges (caused by bolts during creep testing) does not cause the samples to fail in their grip sections.

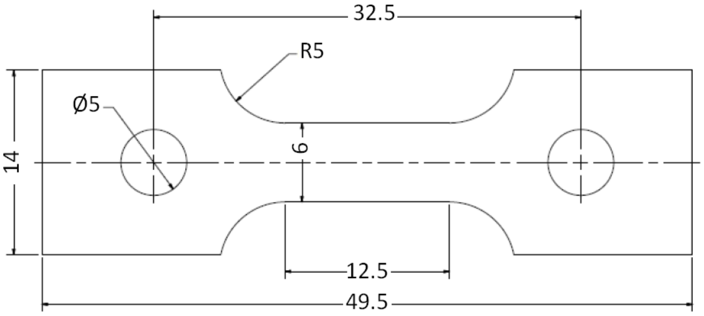

Figure 4.2: Schematic representation of the creep sample shape with its dimensions [mm].

4.2.1. Solution heat treatment

In order to bring the materials into a supersaturated solid solution, the samples had to be annealed for 24 hours at 900 and 1000°C (temperature for Fe4W and Fe6W, respectively). A supersaturated state corresponds to a full dissolution of tungsten atoms in the bcc iron matrix and a relatively defect-free alloy. The chosen temperatures and time are the safe choices for the dissolution of the pre-existing Laves particles in the as-received alloys. The temperatures correspond to the α-phase region above the solvus line, that separates α-phase and the dual phase of α+λ (see Fig. 4.1). To obtain supersaturated alloys in room temperature, the samples had to be rapidly water-quenched after annealing. The created solid solution contains more dissolved tungsten in the iron martix than possible, under equilibrium conditions. Therefore, quenching is the only option to sustain this state, as solute atoms do not have the time to precipitate in the iron matrix.

The entire heat treatment procedure was done using an electric high-temperature vertical tube furnace, where samples were inserted, inside an evacuated silica tube filled with 200 mbar of ultrahigh purity argon. The silica tube was attached to a high-temperature resistant nickel-chromium-aluminum wire and inserted in the middle of furnace tube in a free-hanging position. The centre of the furnace was chosen for its temperature stability. Quenching was done by a free fall of the silica tube into a room temperature water in a metal bucket. When the wire was cut, the silica tube fell into a bucket and broke due to the impact with the bottom.

4.2.2. Grain size

In order to have a closer look at the samples' microstructure prior to creep testing, optical microscopy was used. The samples were priory sanded, polished, etched using 2% Nital solution and cleaned in ethanol in ultrasonic bath. The surfaces of both of the materials were captured on micrographs and the grain size measurements were performed on the optical images using the ImageJ software. The micrographs of the Fe4W and Fe6W surfaces, together with the histograms of their grain size distribution are depicted in Fig. 4.3. As can be seen in Fig. 4.3a (Fe4W) and Fig. 4.3c (Fe6W), the alloys resulted in a supersaturated solid solution with an equi-axed ferritic structure and without any segregation. The diameter of a grain was calculated by measuring a diameter of a circle that has the same surface area as the grain in question. This quantity is named "equivalent diameter" or "EqDiameter". In the Fe6W alloy the average grain diameter is almost five times bigger than that of Fe4W. The total number of grains in the Fe4W alloy is four times greater than in the Fe6W one, which is connected with the grain size. From the standard deviation of grain diameters, it can be concluded that the grain size in the Fe6W alloy varies more than in the Fe4W alloy.

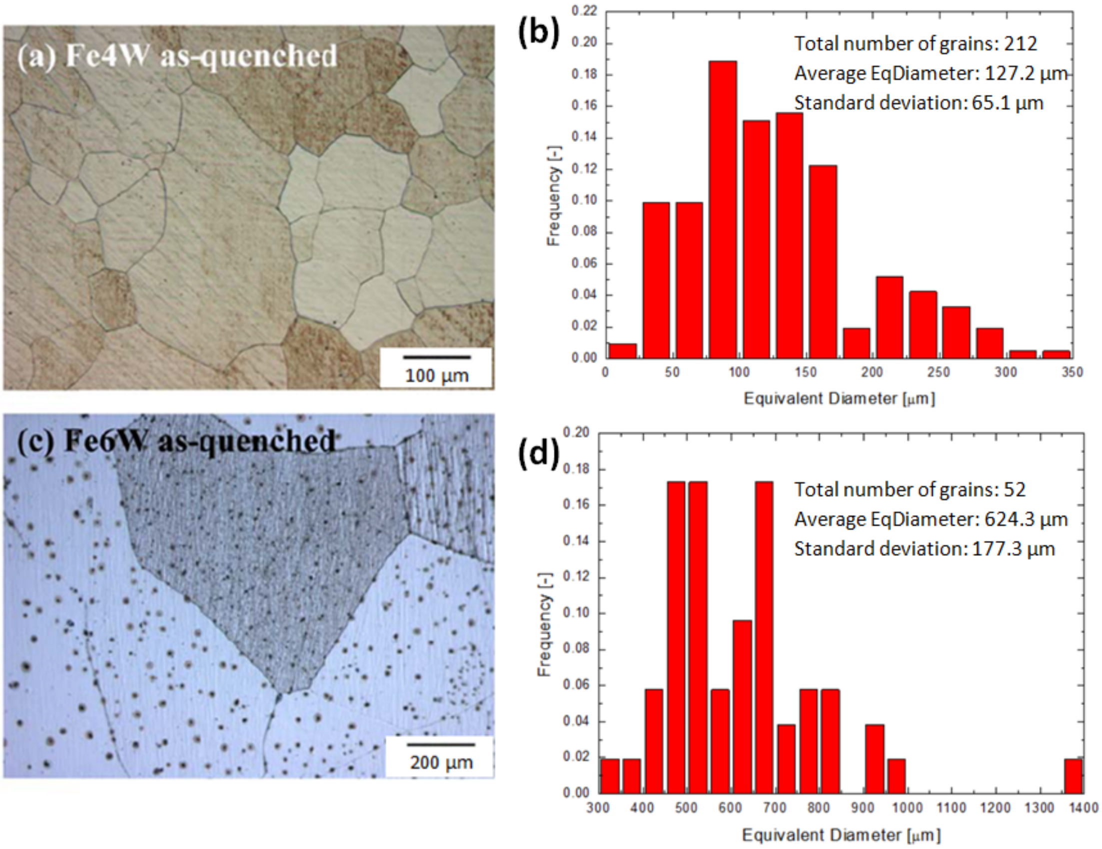

Figure 4.3: Optical microscopy images of the surface of (a) the solutionized Fe4W alloy with (b) its grain size distribution and (c) the solutionized Fe6W alloy with (d) its grain size distribution, after the solution heat treatment. The black dots on the surface of the Fe6W alloy have been examined and appeared to be surface dirt/contamination (not precipitated particles).

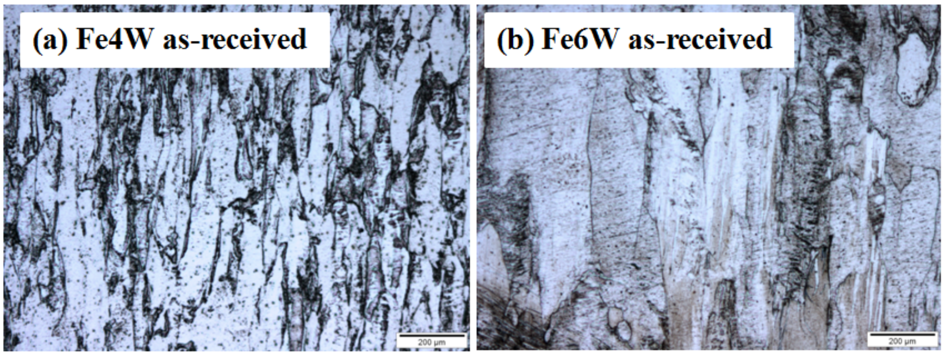

Figure 4.4: Optical microscopy images of the surface of (a) the as-received Fe4W alloy and (b) the as-received Fe6W alloy.

For the sake of monitoring the grain size and shape development before and after annealing, optical microscopy was performed on the samples prior to solution heat treatment. The optical images of the Fe-W alloys before the heat treatment are depicted in Fig. 4.4. From Fig. 4.4 it can be observed, that the shape of the grains visibly differs from the ones included in Fig. 4.3. The elongation of the grains is caused by the cold-rolling process (during sheet manufacturing). In order to compare the sizes of the as-received grains with solutionized ones, their surface area had to be taken into account. The measurement of an equivalent diameter would have led to inaccurate conclusions as the closest approximated shape of the as-received grains is an ellipse, instead of a circle. The average surface area of the grain for the Fe4W alloy was equal to 14,000 μm^2 and 16,000 μm^2 for the as-received and solutionized samples, respectively. For the Fe6W alloys, the average surface area of the grain was around 32,000 μm^2 and 33,000 μm^2 for the as-received and solutionized samples, respectively. All in all, the surface area of the solutionized grains was only slightly larger than the received ones, but their shape significantly differed. The slightly increased surface area of grains is connected with the full dissolution of pre-existing phases and coarsening of solutionized grains. The change in grain shape during annealing is associated with grain boundary migration and grain boundary area reduction, due to the reduction of a material's internal energy [13].

4.3. Creep tests

When the preliminary grain size measurements were performed, all the samples could be used in creep tests.

4.3.1. Set-up and sample mounting

The creep testing was performed using a home-build creep tester. The tester consists of a vacuum chamber furnace that is installed on a universal load frame Instron 5567 with a 1 kN load cell. Both of the arms of the load frame go inside the chamber. The chamber's entrance inlets are sealed in order to sustain a vacuum pressure during experimentation. To mount a sample, the chamber of the furnace has to be disassembled, which is possible due to the design that allows to dismantled it into two halves. The described parts can be seen in Fig. 4.5. Before a sample can be inserted inside the chamber, its mounting to the load frame arms has to be performed properly. Bolts have to go through sample's blanked holes to attach it to the load frame. A metallic bolt has a relatively high thermal conductivity in chosen testing temperature, which can cause a rapid heat transfer to the grips of a sample. Therefore, bolts are supplied with an alumina tube (Al_2O_3) before their insertion. Alumina has a significantly lower thermal conductivity in the chosen testing temperature and prevents a sample from local temperature increase, local softening and premature failure.

When the sample is mounted inside the tester, vacuum is applied to the chamber, both by an incorporated furnace pump ($<1\times10^{-4}$ mbar) and a turbo-pump ($<2\times10^{-5}$ mbar). The purpose of the vacuum is to prevent oxidation of metal during creep testing, which might compromise results. When vacuum is present, high temperature of the order of 500-600°C, and a constant load of the order of 250-450 N can be applied and have to be sustained through the entire test. The temperature readout is recorded by the thermocouples attached to an experimented sample and the inside wall of the chamber. The wires of the thermocouples lead to the destined attachment spots that go outside of the furnace, where the thermocouple adaptors are installed. Temperature is controlled by the LabView software on the set-up's computer. Force of the load frame is controlled by the Instron Bluehill software on the set-up's computer. The creep test parameters are also established and controlled using the Instron Bluehill software. The selection of the load is done in accordance with the stress that is desired to be achieved in the gauge section of a sample. Therefore, the cross-section of a sample in its gauge section has to be priory calculated.

Every creep test is performed in the same exact manner. Firstly, the zero position zero of the load frame has to be found by regulating and adjusting the frame. Subsequently, a preliminary test, without any load, has to be performed in order to establish stable temperature and vacuum pressure. Then, a creep test can be commenced. During creep tests the load and the frame displacement readouts are stored every required time step during the test. Initial creep tests are usually undertaken to evaluate creep mechanisms and lifetimes in certain conditions. Then, the well-established and reproducible creep tests can be performed to produce either deformed or failed samples. The results of the creep test on the Fe-W alloys are presented in the following section.

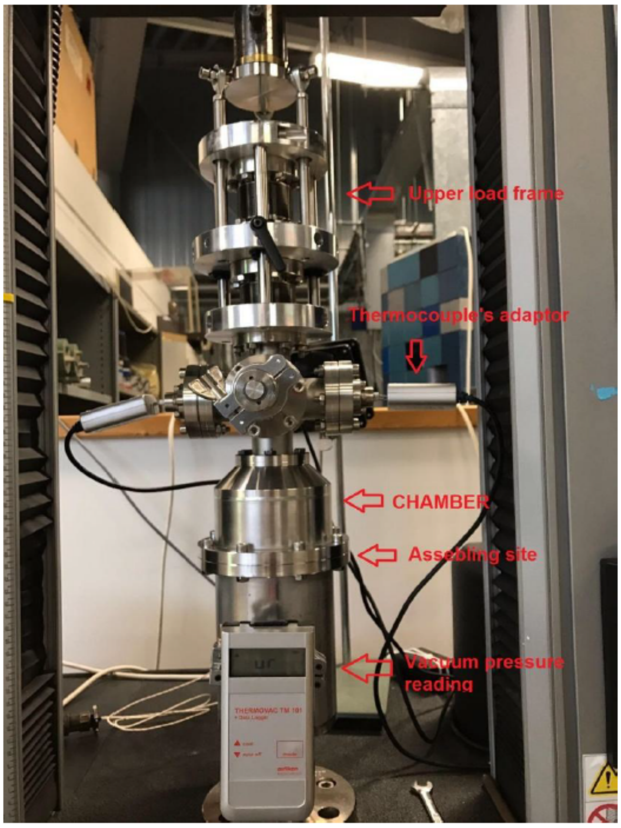

Figure 4.5: Front view of the creep tester mounted on an Instron 5560 load frame.

4.3.2. Creep behaviour at constant temperature

For creep data analysis, it is essential to introduce the Shelby-Dorn equation for the steady-state creep regime [88]:

$$\dot{\varepsilon}_{SS} = A d^m \sigma^n \exp\left(-\frac{Q}{RT}\right), \tag{4.4}$$

where A is a microstructure-dependent constant, Q is an apparent activation barrier, m is the grain size exponent, n is the stress exponent, σ is the applied stress, d is the grain diameter, R is the gas constant and T is the temperature. Using this equation an estimation of the stress exponent can be established, which defines the creep deformation mechanism governing the alloys.

Firstly, the samples were tested at constant temperature (550°C and 580°C for the Fe4W and Fe6W alloys, respectively) for varying stresses. The obtained creep curves from the tests of the Fe4W and Fe6W alloys are presented in Fig. 4.6a and Fig. 4.7a, respecitively. From Fig. 4.6a, it can be observed, that all the Fe4W samples show the expected three-stage creep behaviour, except for the test at 100 MPa (black curve) which was interrupted due to the long length of the test (1113 hours). Furthermore, it can be seen, that the instantaneous strain increases and the lifetime decreases with increasing applied stress for all the samples. From Fig. 4.7a it can be observed, that the creep behaviour of Fe6W samples showed unexpected results as the influence of the increasing applied stress was not consistently changing the deformation behaviour of the samples. For instance, the time to failure of the sample subjected to 120 MPa was higher compared to the sample subjected to 110 MPa, which defies the general creep behaviour. Furthermore, multiple tests on the Fe6W alloys were interrupted due to their long length. This behaviour for the Fe6W alloys imposes difficulties with the repeatability of the creep tests.

Thanks to the obtained strain data for the Fe-W samples, the steady-state creep rate $\dot{\varepsilon}_{SS}$ of each deformation could be derived. Since the strain rate during steady-state creep is directly proportional to the applied stress with the power of the stress exponent ($\dot{\varepsilon}_{SS} \propto \sigma^n$), the stress exponent could be calculated from the experimental creep data. The plots with trendline fittings used for the calculation of the stress exponents are included in Fig. 4.6b (for the Fe4W alloys) and in Fig. 4.7b (for the Fe6W alloys). For the Fe4W alloys the stress exponent is equal to $n = 3.6 \pm 0.2$, which assigns the creep deformation mechanism to a combination of diffusional and dislocation creep, that is believed to govern the α-Fe solid solution [58, 81, 88]. The case of the Fe6W alloys is quite complicated as the stress exponent is equal to $n = 15.2 \pm 3.2$, which falls into the category of dislocation creep in dispersion-hardened alloys [26]. Since the Fe6W alloys were not dispersion-hardened, a plausible explanation for such a high stress exponent is the alloys' grain size that is larger than the thickness of the sample. Due to the large size of the grains, the creep deformation of the Fe6W alloys can be approximated to the creep of a single crystal. In such a case, the creep mechanism governing the deformation of the Fe6W alloys cannot be established by the power-law creep equation (Equation 4.4). In a single crystal, the deformation is governed by dislocation multiplication, motion and interactions with solute atoms, as well as, by the orientation of the crystal planes. In polycrystalline materials, the presence of grain boundaries restricts the movement of slip planes and the transport of solute in the grains, making the deformation more predictable and the creep mechanism distinguishable [50].

From the creep curves, one more essential parameter could be calculated, i.e. the stress exponent for the lifetime, which was used to define the time to rupture of the alloys at a given stress. For the calculation of this exponent, Monkman-Grant equation was used: [74]:

$$t_R \cdot \dot{\varepsilon}_{SS} = C, \tag{4.5}$$

where t_R stands for rupture time f a material and C is a material's constant. From Monkman-Grant relation and Sherby-Dorn equation (Equation 4.4), it can be observed, that the rupture time is inversely proportional to the applied stress with the power of the stress exponent. Therefore, a new exponent can be introduced, which is the aforementioned stress exponent for the lifetime m_{t_R}. This exponent simplifies the relation between the rupture time and the applied stress. Thereby, the rupture time is directly proportional to the applied stress with the power of the stress exponent for lifetime ($t_R \propto \sigma^{m_{t_R}}$). For the Fe4W alloys the stress exponent for lifetime is equal to $m_{t_R} = -3.8 \pm 0.9$, which was calculated using the plot from Fig. 4.6c. For the Fe6W alloys the exponent was not calculated, due to the lack of creep lifetime data.

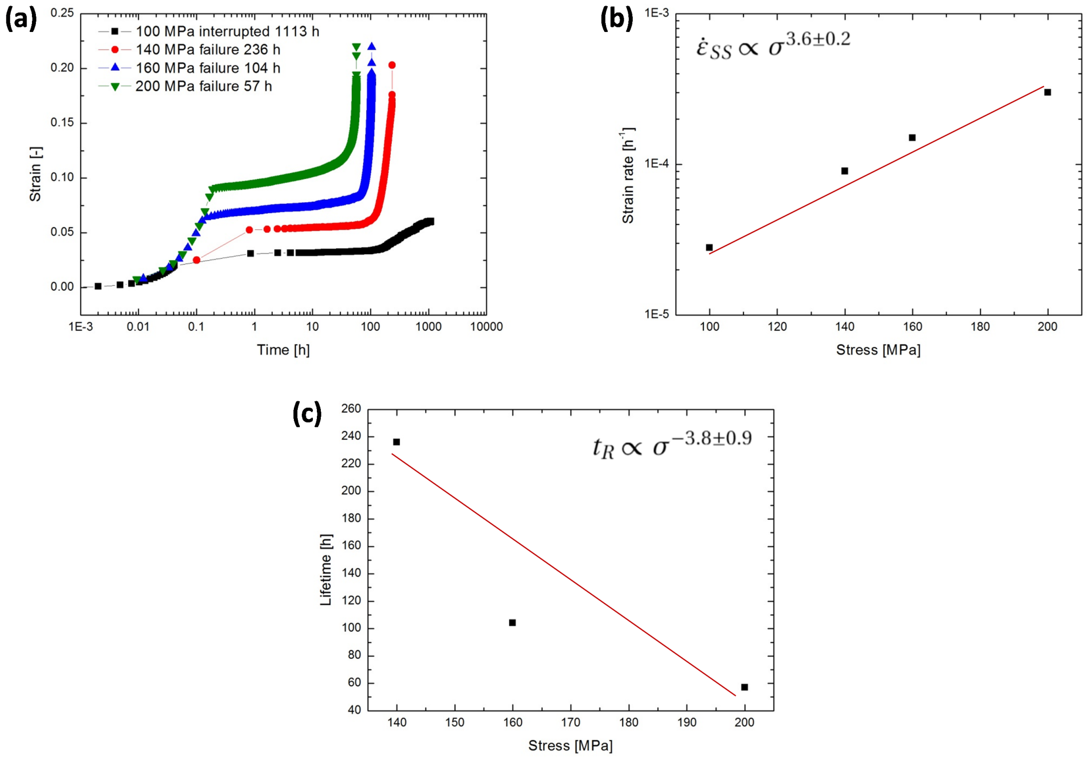

Figure 4.6: (a) Creep curves of the Fe4W samples for a varying applied stress at 550°C, (b) steady-state creep rate as a function of applied stress derived from the creep curves and (c) applied stress versus the creep lifetime plot obtained from the creep tests on the Fe4W samples.

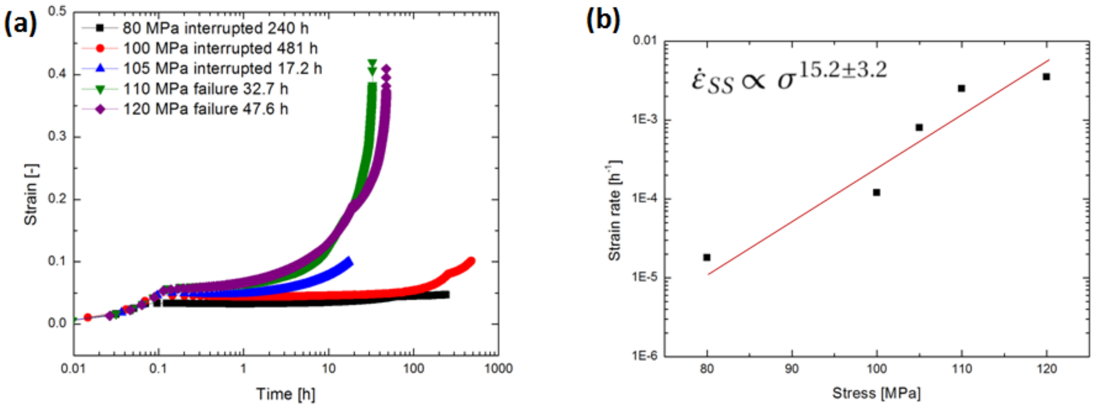

Figure 4.7: (a) Creep curves of the Fe6W samples for a varying applied stress at 580°C and (b) steady-state creep rate vs. the applied stress derived from the creep curves.

Using all the calculated parameters of the Fe4W alloys, the expected creep lifetime and the creep rate could be estimated at any applied stress. Therefore, the Fe4W alloys could be subjected to interrupted creep in selected stress conditions at 550°C. The purpose for this procedure was connected with X-ray tomographic investigation of the self healing mechanism during different stages of the alloys' creep lifetime. Due to the unpredictability of the Fe6W alloys, the samples made from this material were left out of the investigation, and were subjected to the grain reduction procedure, described in the next section.

4.3.3. Creep behaviour at constant stress

According to [76], the activation energy for tungsten self-diffusion in α-iron is equal to $Q = 312 \pm 27$ kJ/mol. The activation energy of solute self-diffusion is usually assumed to be the activation energy for diffusional creep [2]. The experimental activation energy can be estimated using Sherby-Dorn equation (Equation 4.4) when alloys are tested in varying temperature at the same subjecting stress. This process was performed on the Fe4W alloys at 550, 560 and 575°C with an applied stress of 140 MPa. The obtained creep curves are presented in Fig. 4.8a. The activation energy was derived from the steady-state creep rate versus $1000/T$ (T – temperature of exposure) plot (Fig. 4.8b), that shows the Fe4W alloys' temperature dependencies at the constant applied stress. The Fe4W alloys' experimental activation energy for creep is equal to 1588 kJ/mol, which is five times larger than the theoretical activation energy for tungsten self-diffusion in α-iron. The reason for such a large activation energy for creep can be connected with the fact, that creep deformation of the Fe4W alloys is not only governed by volume diffusion creep mechanism, but a combination of diffusion and dislocation creep mechanisms. Therefore, the experimentally calculated activation energy cannot be considered as the activation energy of W self-diffusion in the bcc-Fe matrix.

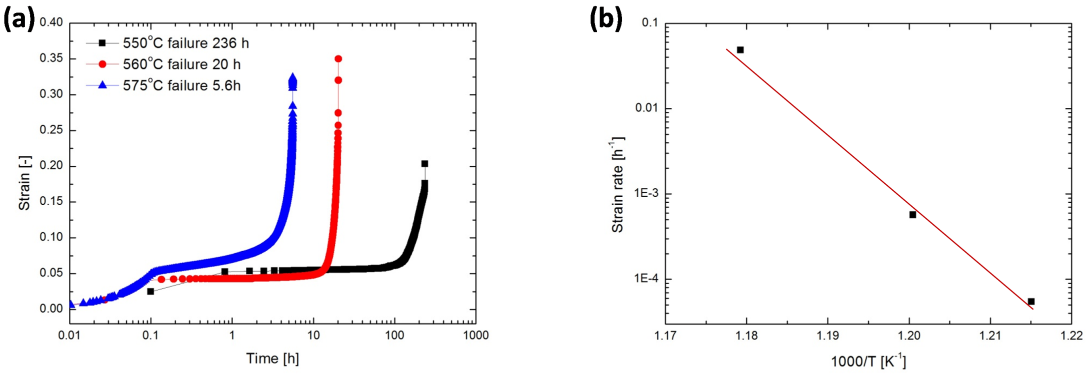

Figure 4.8: (a) Creep curves of the Fe4W samples for different temperatures of exposure at a stress of 140 MPa and (b) a plot of steady-state creep rate versus $1000/T$ used for the calculation of the creep activation energy of the Fe4W alloys.

4.4. Grain size reduction

The large grain size of the Fe6W alloys was the reason for the unexpected results of their creep testing. Therefore, an attempt to decrease the grain size of the Fe6W alloys was undertaken. Such a procedure involved a sequence of sample annealing with consecutive quenching. First, the samples were annealed at the temperature of the austenitic phase formation (around 1100°C, see Fig. 4.1) and were subsequently rapid water-quenched. The second annealing procedure involved annealing of the samples at the temperature of their solid solution heat treatment (1000°C) and subsequent rapid water-quenched. Thanks to the first procedure, a nucleation of the γ-phase inside the α-phase can be achieved, which is expected to take place within the grains (see Fig. 4.9). Then, after the second procedure, the parts of the austenitic phase are expected to transform into the α-phase, creating new grains. Despite the expectations of the grain size reduction in the Fe6W alloys, the results of the annealing processes were unsuccessful (see Fig. 4.10). From Fig. 4.10 it can be seen, that not only the grain size was not reduced, but also the desired microstructure was not found on the surfaces of the alloy. Therefore, either there was not enough time for the γ-phase to nucleate during the first process or the γ-phase was formed and instantly transformed back to the original α-phase during the second process. Due to these unsatisfactory results, an alternative process for the grain size reduction is advised.

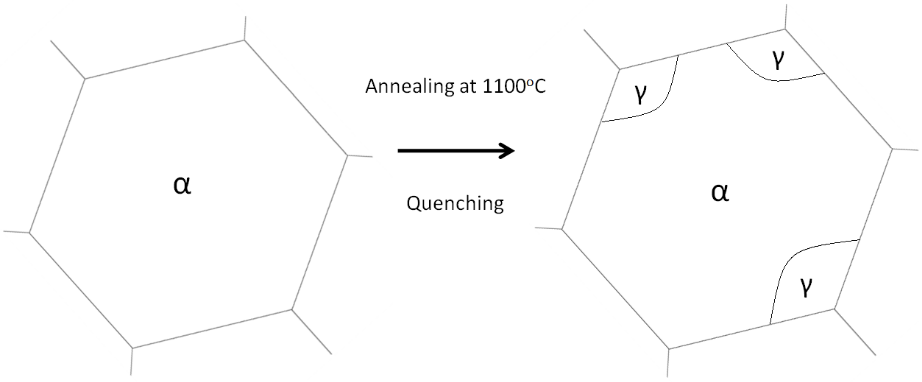

Figure 4.9: Schematic representation of the expected Fe6W alloy mictrostructure after the phase transformation from α to α+γ.

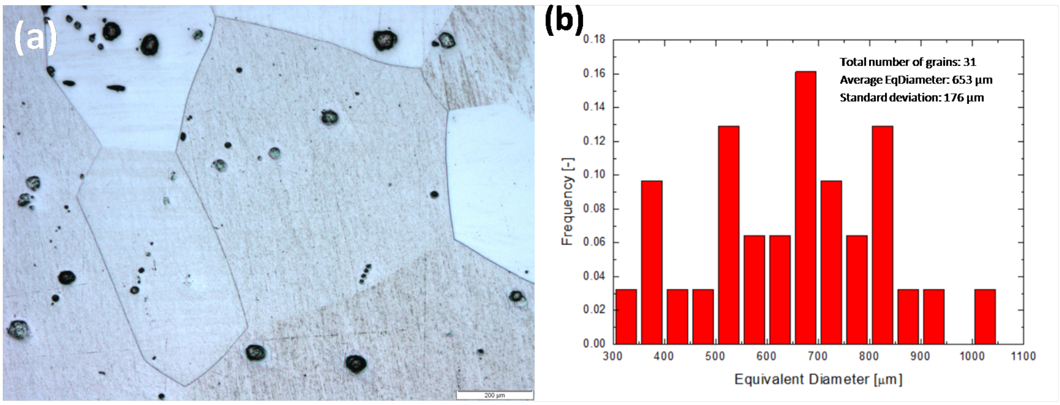

Figure 4.10: (a) Optical microscopy image of the surface of the Fe6W alloy that underwent a grain size reduction process, together with (b) the grain size distribution after the attempted reduction.

4.5. Microstructure after creep

The self healing effect in alloys can be studied by the means of electron microscopy, which may result in a direct visual proof of creep damage filling by the second phase precipitation. Therefore, the microstructure of the Fe-W alloys were analyzed by a JEOL JSM 6500F Scanning Electron Microscope with a field emission electron gun, equipped with detectors for secondary and back-scattered electrons, as well as, an energy dispersive detector. The electron beam energy and current were 15 keV and 80 μA, respectively. Before every scanning process, the samples had to be conditioned (same procedure as for optical microscopy) and cleaned in ethanol in an ultrasonic bath.

4.5.1. Microstructure of Fe-4W alloys

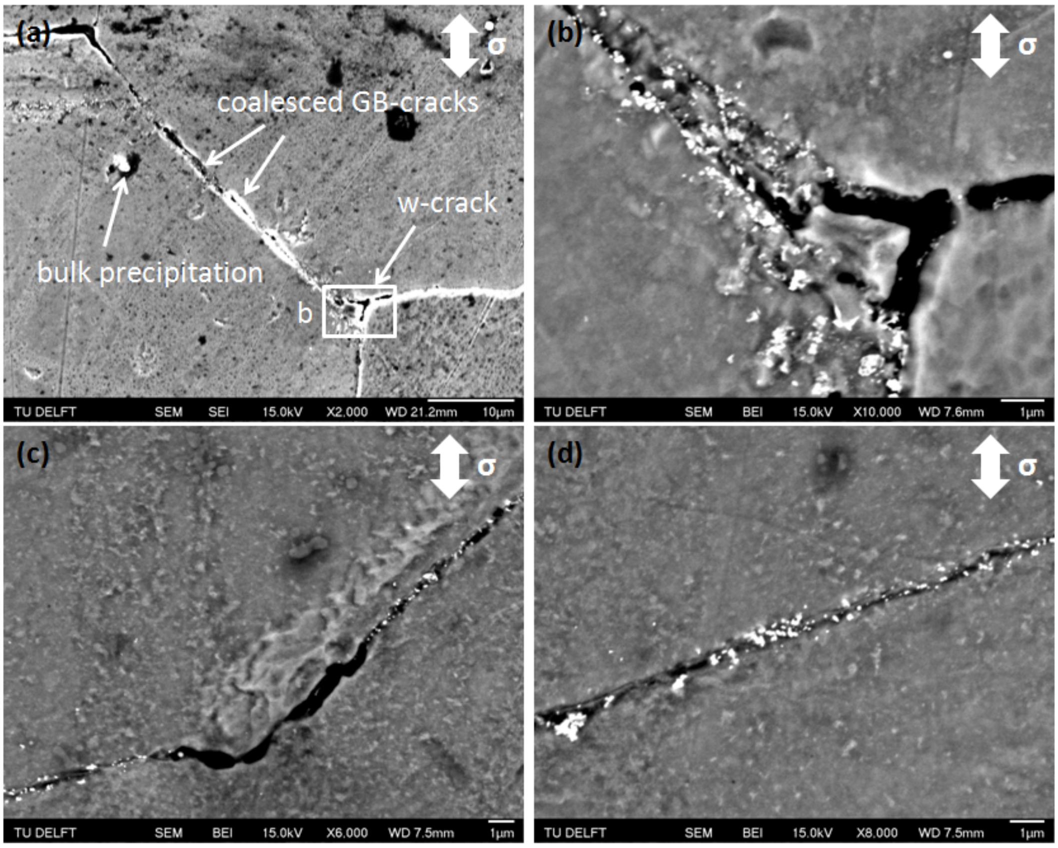

Figure 4.11: Back scattering SEM images of the surface of the Fe4W alloy after creep failure (at 140 MPa at 550°C. (a) Image with a magnification of 2,000× that shows different creep damage and bulk precipitation. (b) Image with a magnification of 10,000× that shows a precipitated wedge crack. (c-d) Images with a magnification of 6,000× and 8,000×, respectively, that show coalesced precipitated cavities along a grain boundary.

Fig. 4.11 shows a back-scattering scanning electron microscopy (SEM) micrograph of the surface of the Fe4W alloy after creep failure at 140 MPa and 550°C. In Fig. 4.11a creep cavities, such as cavities along grain boundaries and grain-boundary triple junction wedge cracks on stress-affected grain boundaries, can be observed. The creep damage in the Fe4W alloy developed to the extend at which the cavities coalesced, forming micro-sized cracks. The density ofW-rich precipitates is relatively low, and therefore the cavities are only partially filled. Nonetheless, a site-selective precipitation of tungsten in the Fe4W alloys can be confirmed. Fig. 4.11b-d show back scattering SEM images of creep damage in the Fe4W alloy in higher magnifications. It can be observed, that most likely, the solute depletion into the cavities takes place from the bulk of the material. Furthermore, it can be seen, that the solute atoms segregate at the edges of the cavities, where they nucleate and grow into precipitates, which confirms the heterogeneous precipitation at creep-induced damage in the Fe4W alloys.

As mentioned previously, the Fe4W alloys are subjected to interrupted creep tests, when their rupture time is well-established. Therefore, for the sake of comparison with the Fe4W alloys after creep failure, SEM micrographs of the Fe4W alloy's surface after interrupted creep at 140 MPa and 550°C are presented in Fig. 4.12. The creep deformation of this alloy was interrupted at the half of the rupture time ($t = 0.5t_R = 52$ h).

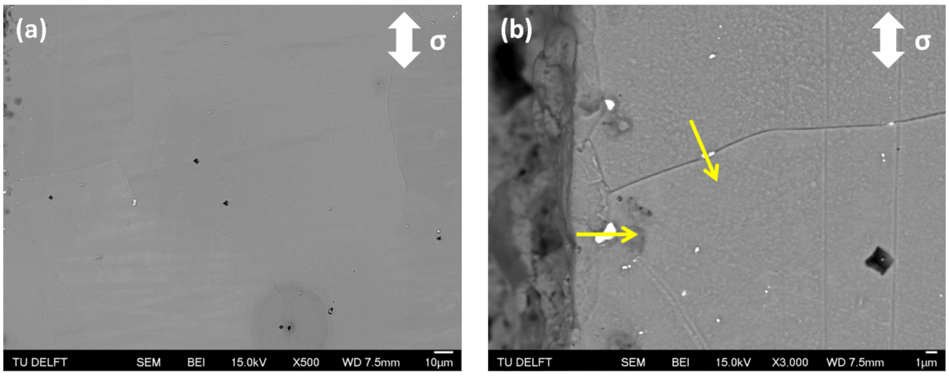

Figure 4.12: Back scattering SEM images of the surface of the Fe4W alloy after interrupted creep ($t = 0.5t_R = 52$ h) at 140 MPa and 550°C. (a) Image with a magnification of 500× that shows precipitated cavities along grain boundaries. (b) Image with a magnification of 3,000× that shows a different surface region with the precipitated cavities along grain boundaries. Yellow arrows indicate the direction of the EDS scans.

Fig. 4.12 shows a back-scattering SEM micrographs of the surface of the Fe4W alloy after interrupted creep ($t = 0.5t_R = 52$ h) at 140 MPa and 550°C. In Fig. 4.12a precipitated creep cavities along grain boundaries can be observed. Fig. 4.12b shows a different surface region of the Fe4W alloy, where fully filled grain-boundary cavities can be seen. The precipitated grain-boundary cavities are isolated and show a higher filling ratio compared to the cavities observed on the surface of the Fe4W alloy after creep failure, where no fully filled damage can be seen (see Fig. 4.11b-d). From Fig. 4.12b it can be concluded, that the cavities did not coalesce and therefore, the volume of damage is lower compared to the one observed on the surface of the Fe4W alloy after creep failure. The decreased damage volume leads to high filling ratios of the isolated cavities as the solute atoms have a limited open-volume surface to precipitate to.

Energy-dispersive X-ray spectroscopy (EDS) line scans were performed across two precipitated cavities depicted in Fig. 4.12b (the directions of the scans are indicated by the yellow arrows). It was observed, that the tungsten atomic concentration increases to a value of 33 at.%, when the scans go through the middle of the precipitation. This concentration matches the expected atomic percentage of tungsten in the Laves phase (Fe_2W).

4.5.2. Microstructure of Fe-6W alloys

Despite the fact, that the Fe6W alloys showed unexpected results during creep testing, due to the large grain size, their microstructure was examined by means of scanning electron microscopy. The results are depicted in Fig. 4.13.

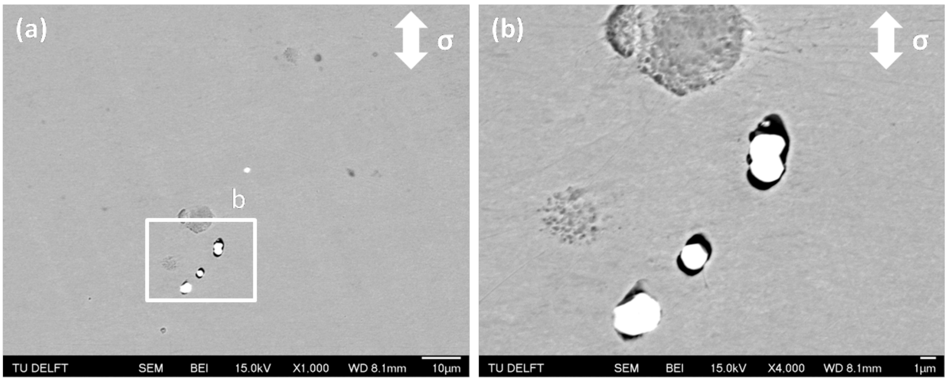

Figure 4.13: Back scattering SEM images of the surface of the Fe6W alloy after creep failure at 120 MPa at 580°C (a) An image with a magnification of 1,000× bulk precipitates with nucleated voids around them. (b) A closer look of (a) in a magnification of 4,000×.

Fig. 4.13 shows back-scattering SEM micrographs of the surface of the Fe6W alloy after creep failure at 120 MPa and 580°C. Unfortunately, grain boundaries did not show any precipitation. However, bulk precipitates were found on the alloys surfaces, which are depicted in Fig. 4.13a and, in higher magnification, in Fig. 4.13b. I can be observed, that around the bulk precipitation, voids are nucleated. Since the bulk precipitates are the undissolved second phase, which remained after the solid solution heat treatment, the defects around the particles can be assigned to the decohesion of precipitates from the cavity surfaces, that took place during creep deformation of the Fe6W sample.

4.6. X-ray tomography

Scanning electron microscopy is a 2-dimensional imaging technique and it imposes limitations when a precise investigation of creep cavity filling and the exact locations of healed sites is desired. Therefore, for a more extensive study of the self-healing effect in Fe-W using X-ray nano-tomography has been employed.

4.6.1. Background and underlying physics

X-ray nano-tomography (usually called nano-CT: Computerized Axial Tomography) is a radiographic imaging technique with an ability to render 3-dimensional representation of the internal structure of optically opaque materials. Its spatial resolution capabilities can reach tenths of nanometeres, and it allows a non-destructive testing of materials, with a minimal specimen preparation [52]. Nowadays, due to the popularity of X-ray tomography that boomed 20 years ago, a lot of facilities offer this technique of material investigation. The tomographs differ from laboratory tomographs to synchrotron tomographs, with or without in-situ devices [8]. The technique used for the investigation of Fe-W alloys was synchrotron X-ray nano-tomogrpahy. Therefore, this particular method is described, but the basic principles of the technique are applicable for all the available set-ups.

Synchrotron radiation is prodcued by the bending of a high-energy electron beam by a magnetic field. The advantage of a sychrotron X-ray source is that the emitted light is significantly greater in brightness, compared to the one emitted by conventional X-ray sources. Such a high flux of the X-ray beam helps to acquire detailed images of materials that possess relatively low variations in absorptivity. Furthermore, synchrotron tomographs allow X-ray energy to be tuned to a narrow energy band, which can result in a monochromatic X-ray beam that enhances the accuracy of the images, by resolving the energy dependence on X-ray absorption [8, 52]. Synchrotron tomography can be based on two different approaches of the interpretation of X-ray transmitted beam [56]:

X-ray tomography based on phase contrast

Synchrotron X-ray tomography can be based on the phase contrast detection method. In this X-ray tomography, the X-rays are considered as electromagnetic waves. When X-ray waves pass through an object, not only they are attenuated (decreased in amplitude), but also their phase is changed. This is due to the complex refractive index of the material, which can be represented as follows [3]:

$$n = 1 - \delta + i\beta, \tag{4.6}$$

where δ is the decrement of a real part of the refractive index and β is known as an absorption coefficient. The complex refractive index is determined by the electron density of a material and is directly proportional to the decrement of a real part of the refractive index.

The X-ray electromagnetic wave can be described as [3]:

$$\Psi(z) = B_0 \mathrm{e}^{inkz} = B_0 \mathrm{e}^{i(1-\delta)kz} \mathrm{e}^{-\beta kz}, \tag{4.7}$$

where δkz is the phase shift (k being the angular wavenumber and z being the direction of wave propagation normal to the surface of the medium) and $\mathrm{e}^{-\beta kz}$ is the exponential decay factor decreasing the amplitude of the wave, $B_{0.}$

In more general terms, the total phase shift of the X-ray beam traveling a distance z at specific sample locations, represented by the coordinates x and y, can be estimated using the following equation [3]:

$$\Phi(x, y) = -\frac{2\pi}{\lambda} \int_0^z \delta(x, y, z)\,dz, \tag{4.8}$$

where λ is the wavelength of the incident X-ray beam.

When an object is illuminated by the X-ray photon beam, located at a fixed position, the changes of phase in X-ray beam are recorded (for each angular position of the sample) by a out-of-plane moving detector, while the sample is rotating about its single axis (see Fig. 4.15). By measuring the phase change across the entire object at different positions of a detector, a higher image quality, compared to X-ray tomography based on attenuation (in the case when the material has low variations in absorptivity), can be obtained. However, such a technique requires a homogeneous and spatially coherent beam. Otherwise, the images can result in an ambiguous representation of the internal structure [14, 41].

A recent development in the phase contrast X-ray tomography offers an even more reliable representation of scanned objects for low variations in attenuation coefficients. This technique is called holotomography and uses a variation of several specimen-source distances (for each angular position of a sample) to measure the phase shift and attenuation of the electromagnetic waves. This method produces near-field unravelled Fresnel diffraction patterns (i.e. interference between non-affected and diffracted components of the beam), which can be reconstructed and combined into phase maps (see Fig. 4.14). The phase maps are reconstructed via phase retrieval procedure that uses iterative algorithms to extract amplitude and phase contrast from the images, captured at different sample-source distances, in order to render one reconstructed 2-dimensional tomograph. This technique allows to obtain a quantitative distribution of the phase. The reconstructed tomographs reveal the electron density and absorptivity distribution inside the material, which is useful in distinguishing details of the internal structure, i.e. phase edges. The drawback is that this technique is connected with high acquisition time, as a large number of images has to be recorded [14–17].

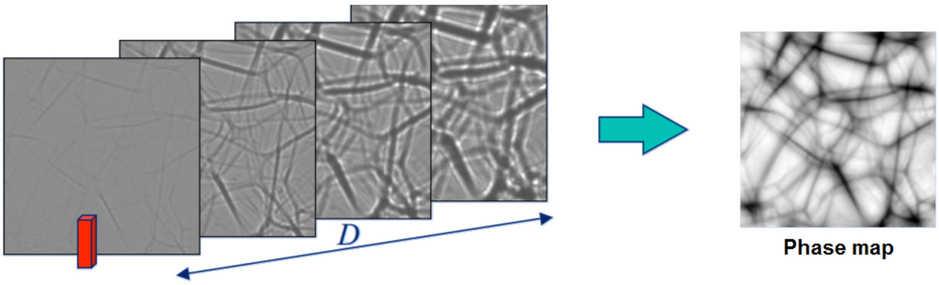

Figure 4.14: Schematic representation of the synchrotron X-ray phase contrast holotomography. Fresnel patterns are recorded at several sample-detector distances (left-hand side), reconstructed, and recombined into phase maps - (right-hand side) to show the distribution of the phase contrast. Note, that the tomographic projections are taken at a single angular position of the sample [14].

X-ray tomography based on attenuation

Synchrotron X-ray tomography can also be based on the detection of the attenuation of the beam transmitted through an object. This procedure is done by illuminating a sample with a beam of high energy X-ray photons, which interact with matter. X-ray photons can penetrate a sample, be: (i) scattered by energetic electrons, depositing no energy or (ii) be absorbed by it, either depositing all their energy and exciting electrons from atoms or depositing a part of their energy simultaneously exciting an electron and resulting in a photon with reduced energy (Compton effect). The absorption type depends on electron binding energies with the nuclei. The interactions strongly increase with increasing number of electrons (i.e. with atomic number) [38, 64]. In other words, the bigger the atomic number of atoms, the bigger the number of interactions of X-ray photons with matter, which results in a larger number of absorbed photons and/or photons with decreased energy. The number of absorbed photons and the decrease in energy of scattered photons, decrease the intensity of the X-ray incident beam. As mentioned before, the intensity of the X-ray beam is the amplitude of X-ray electromagnetic waves. Therefore, considering the complex refractive index presented in Equation 4.5 and a scalar wave function from Equation 4.6, the total amplitude decay of the X-ray beam traveling a distance z at specific sample locations, represented by the coordinates x and y, can be represented using the following equation [14]:

$$B(x,y) = \frac{2\pi}{\lambda}\int_0^z \beta(x,y,z)dz, \tag{4.9}$$

knowing that $\beta = (\lambda/4\pi)\mu$, an attenuation coefficient μ, which depends on the atomic number of a material, can be incorporated into Equation 4.9.

The attenuated X-ray electromagnetic waves are recorded by a out-of-plane moving detector across the entire sample (for each angular position of the sample), while the object in question is rotating about its single axis [14], which is exactly the same measuring procedure as in the phase contrast tomography, which is schematically represented in Fig. 4.15.

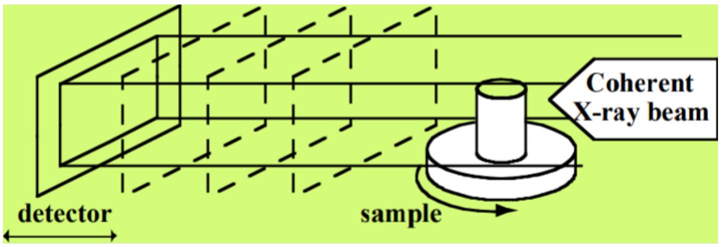

Figure 4.15: Schematic representation of a synchrotron X-ray phase contrast and attenuation tomography [14].

A difference between the attenuation X-ray tomography and phase contrast X-ray holotomography in case of a reconstructed scan is presented in Fig. 4.16. As it can be observed, areas with little differences in absorptivity are not visible in the absorption scans (left-hand side), while they are revealed for the phase contrast scans (right-hand side).

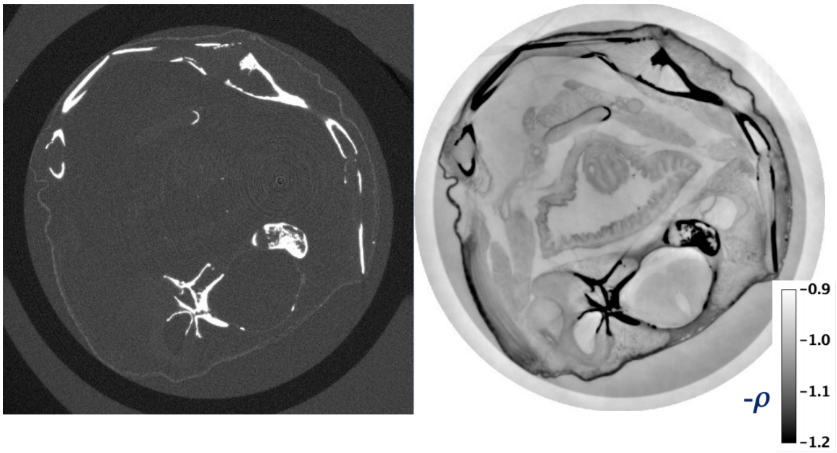

Figure 4.16: Reconstructed tomography scans of a frog for attenuation X-ray tomography (1 scan, left-hand side) and X-ray holotomography (3 holotomographic scans after phase retival, right-hand side). ρ stands for the atomic number density [14].

A difference between the phase contrast tomography and holotomography is presented on reconstructed 3-dimensional scans in Fig. 4.17. As it can be observed, holotomographs reveal absorption differences in the material structure (left-hand side), which cannot be visible for conventional phase contrast tomographs (right-hand side).

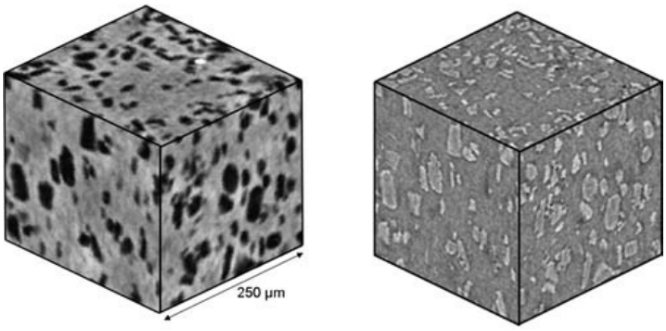

Figure 4.17: Three-dimensional tomographic reconstructions of a metal composite consisting of an aluminum matrix and 20 vol.% Al_20_3 particles. Left-hand side - holotomography, right-hand side - phase contrast tomography [6].

4.6.2. Reconstruction of tomographic images

To produce a tomographicaly reconstructed scan, every defined angular position of the sample has to be recorded and the projections have to be "stitched" together. This method is applicable for each of the above-mentioned tomography techniques. In order to perform a tomographic reconstruction of a scan, analytical reconstruction algorithms have to be implemented. Numerous methods exist, but they all take into account two assumptions. Namely:

- the projection slices are infinitely thin
- for any detector and source position, all photons travel in the same straight line.

In such a way, the difference between voxel and pixel disappears during reconstruction [42]. This information is used by the algorithm to produce a tomographic scan. Since the description of reconstruction techniques is beyond the scope of this work, a brief overview of two most popular methods is presented.

1. **Filtered Back Projection Reconstruction**: it is an analytical reconstruction algorithm that applies a convolution filter to discard blurring. It applies simultaneous equations on the projection sums at differing angles to compute the values of either attenuation coefficients or electron density (or both) within a cross-section of an object. The simultaneous equations are essential to result in a correct values of the aforementioned parameters [8, 83]. To render an image, the different values of the absorptivity and/or electron density are given in greyscale intensity values and each of these values comprises one pixel on a tomographic scan.

2. **Fourier Slice Theorem**: this theorem states that: "the Fourier transform of an object's projection at any angle equals a line taken in the same orientation of the two-dimensional Fourier transform of the same object" [44]. Using this information, all projections taken from different angles can be represented on one polar coordinate grid. The values of frequencies are then assigned to greyscale intensity values and each of them comprises one pixel on a tomographic scan.

4.6.3. Experimental details for the synchrotron X-ray nano-tomography

With the theory lied down, all the specifications of the precise morphological study of the Fe-W samples can be described. The technique used for the study on the Fe-W alloys was a synchrotron hard X-ray holotomography instrument based on phase contrast with high spatial resolution. The instrument is located at beamline ID16A at the ESRF (Grenoble, France). The high energy monochromatic coherent X-ray beam of 33.6 keV was selected for this experiment. Fresnel diffraction patterns were recorded at four different source-sample distances for one tomographic projection and the phase maps were reconstructed by phase retrieval process using the GNU Octave software [24].

Bar-shaped samples were prepared by machining the gauge sections of the creep samples using spark erosion (see Fig. 4.18). If the sample was fractured, the machining was done beneath the broken site of the gauge section.

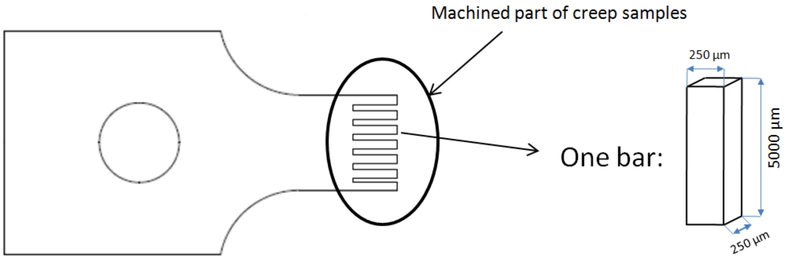

Figure 4.18: Schematic representation of the cut and machined creep sample used in the X-ray holotomography (left-hand side). Bar-shaped sample mounted in the X-ray tomography set-up (right-hand side).

The bar-shaped sample was mounted with its longest dimension upwards in the sample holder. It was scanned, while rotating about its z-axis. The projections were recorded by a detector with a 2048×2048 binned pixels array. One tomographic scan performed 1500 projections, with an exposure of 1 second for the resolution of 100 nm. The measurements were conducted under sustained high vacuum to prevent any unnecessary X-ray transmission losses and X-ray scattering from air (which is the reason of the enhanced background on tomographs). The projections were tomographicaly reconstructed via a filtered back projection reconstruction algorithm method using the ESRF PyHST software package [24]. A schematic representation of the X-ray nano-tomography procedure is presented in Fig. 4.19.

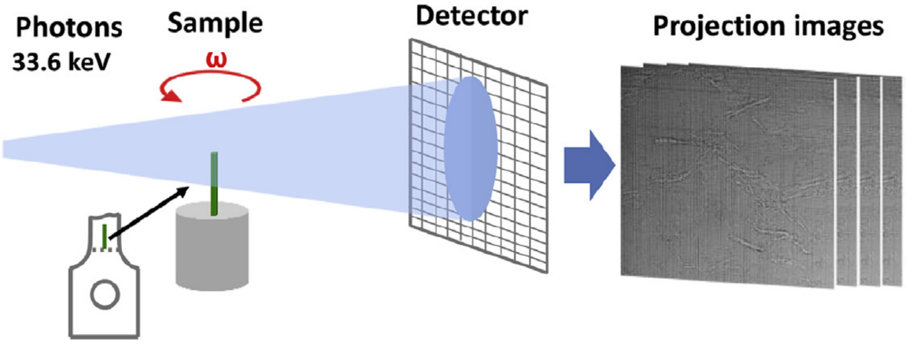

Figure 4.19: Schematic diagram of the synchrotron X-ray holotomography imaging process [24].

4.6.4. Analysis of the Fe-W tomographic data

From scanning electron microscopy images, combined with energy-dispersive spectroscopy, we know that the phases present in the Fe-W samples are: the Fe-W alloy matrix (bcc structure), empty creep cavities and W-rich precipitates (33 at.% W and 67 at.% Fe). During the data analysis, the W-precipitates and cavities were of most interest, as they directly define the self healing activity in the alloy. Since electron density of tungsten is much higher than that of iron and vacuum, and because the electron density of iron is much higher than that of vacuum, the phase contrast differences between the phases is easily recognizable on the tomographic scans. Which means that the dark features can be assigned to precipitates, while the bright features correspond to cavities. The contrast in the scans is dominated by phase contrast, due to the free propagation of the X-ray beam in the tomographic set-up [24].

3D rendering of the Fe-W samples

Knowing the differences in composition for the expected phases, a 3-dimensional reconstruction of the tomographic scans could be performed. In order to do this, the Avizo Fire 8.1 software was used. Firstly, all the scans for a particular sample were loaded by the programme, which layered them according to their sequence and rendered a voxel intensity histogram (see Fig. 4.20). Thanks to the back filtered projection reconstruction, all the electron density values recorded in the cross-sections of the Fe-W sample were given in different greyscale intensity values. One voxel (which is equal to the volume of 100×100×100 nm) has its assigned grayscale value, which is equivalent to a phase shift recorded by a detector. Segmentation of precipitates and cavities with assigned greyscale intensity threshold values could be achieved by means of the Avizo Fire software, threshold filters and an extensive study of local electron density variations in the FeW alloys (done by H. Fang [24]). This procedure resulted in 3-dimensional rendering of the scanned samples, which represent the division of the three material phases in three different colors. An example of such a rendering can be seen in Fig. 4.21.

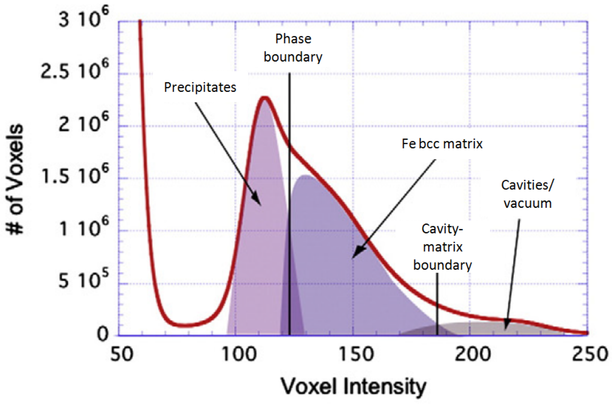

Figure 4.20: Exemplary histogram depicting the number of voxels appearing in particular greyscale intensity values (named as voxel intensity) [52]. A voxel intensity histogram represents the frequency of all the greyscale intensity values that appear on all the layered scans.

Processing of 3D renderings of the Fe-W samples

For a further data analysis, the 3-dimensional render volumes had to be split into smaller boxes, called regions of interest (ROI). This procedure is strictly connected with computer RAM capacity, which could not handle an analysis performed on the entire sample. All the ROIs include both the cavities and precipitates. In order to investigate the filled parts of cavities, appropriate Avizo Fire 8.1 functions had to be used, due to the fact, that the partially filled cavities were disconnected from the whole cavities as a result of the smoothing filters used during thresholding processes. The functions employed were dilating the cavity and precipitate particles by 3 pixels in face (6×3 pixels), corner (8×3 pixels) and side (12×3 pixels) directions to establish their connectivity. If the dilated precipitate particles had a corner, face or side contacts with cavity particles, they were assumed to belong to a one precipitate-cavity structure. This process was done to have a visual confirmation of precipitate-cavity interconnection. After this procedure, the structures were smoothed for the second time and saved as separate precipitates and cavities binary images. Fig. 4.22 shows exemplary binary images that were filtered from a single tomographic scan from one of the regions of interest. After binary image rendering, used for quantitative data analysis, each of the reconstructed particles was labeled and analyzed to obtain their volume and position.

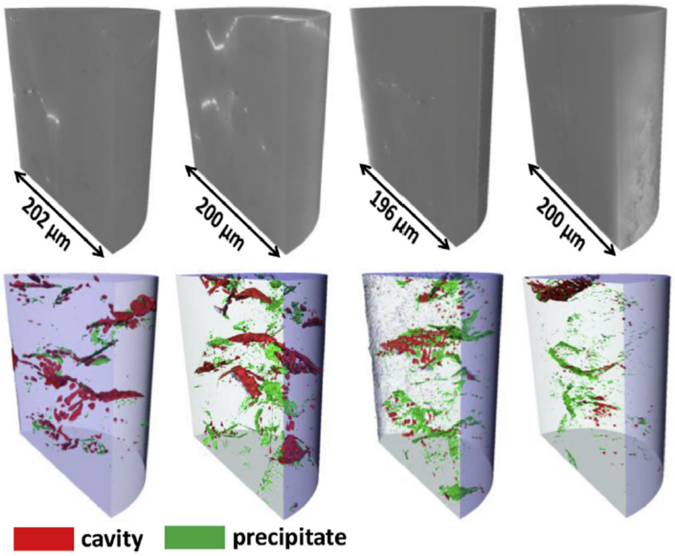

Figure 4.21: 3-dimensional renderings of the tomographic scan reconstruction of four different Fe-Au samples. Cavities are marked in red and precipitates in green [24].

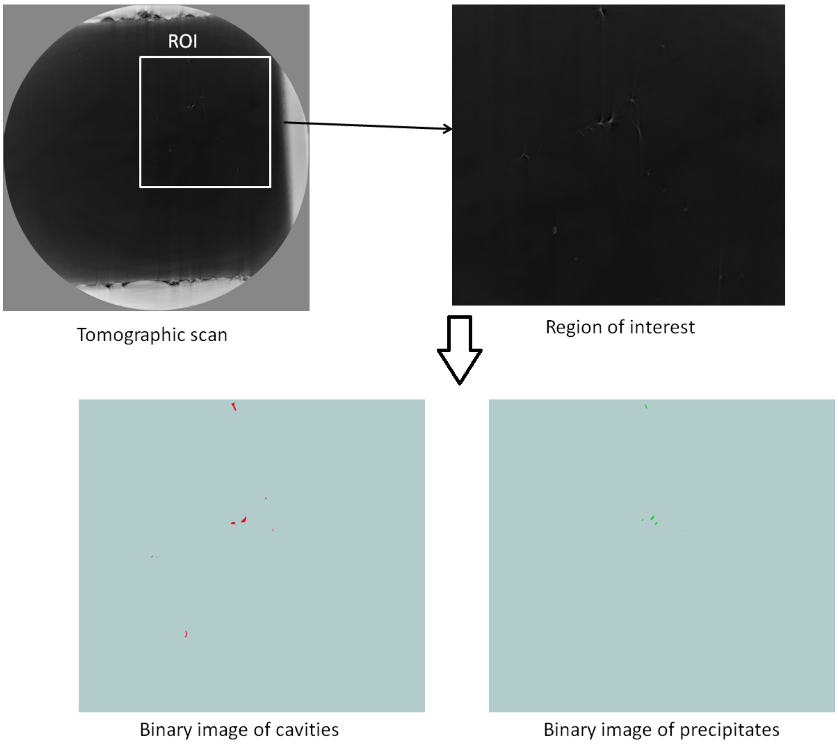

Figure 4.22: A sequence of filtering for 3-dimensional tomographic reconstruction shown on a single tomographic scan. When the tomographic scans are layered and reconstructed (Fig. 4.21, upper row) using Avizo Fire 8.1, and when the thresholds are applied (Fig. 4.21, bottom row), ROIs can be selected and cropped from original tomographic scans. After second layering, thresholding and reconstruction, particles are dilated and structures are established. Binary images of cavities and particles can be rendered for each tomographic slice.

Quantitative data analysis and shape classification of the Fe-W

Using the binary images, a quantitative data analysis could be performed by the MATLAB software with the DIPimage toolbox. The DIPimage programme dilates the binary images of particles and checks the connectivity of the structures. Images are treated by the DIPimage as matrices with values 1 and 0 (see Fig. 4.23). The dilated matrix of precipitates is multiplied by the dilated matrix of cavities, which results in the values of 1 in their overlaps. Dilation is only used to establish the cavity-precipitate connection for filling ratio calculation, while other parameter calculations are performed on original binary images. In previous research it has been proven, that if the 3-dimensional representations of precipitates and cavities lie separately within a radius of 300 nm (specifically for 100 nm resolution of X-ray tomography), they belong to the same precipitate-cavity structure [70].

After the computation for all the binary images, the parameters needed for the shape classification of particles were calculated. One voxel was set to be equal to a volume of $100 \times 100 \times 100$ nm. Hence, the results of all the parameters were directly rendered in metric units. The filling ratio of the particle-cavity structures was calculated using the following equation:

$$FR = \frac{V_{precipitate}}{V_{cavity} + V_{precipitate}}, \tag{4.10}$$

where $V_{precipitate}$ is the total volume of precipitates in contact with the cavity and V_{cavity} is the unfilled volume of the cavity.

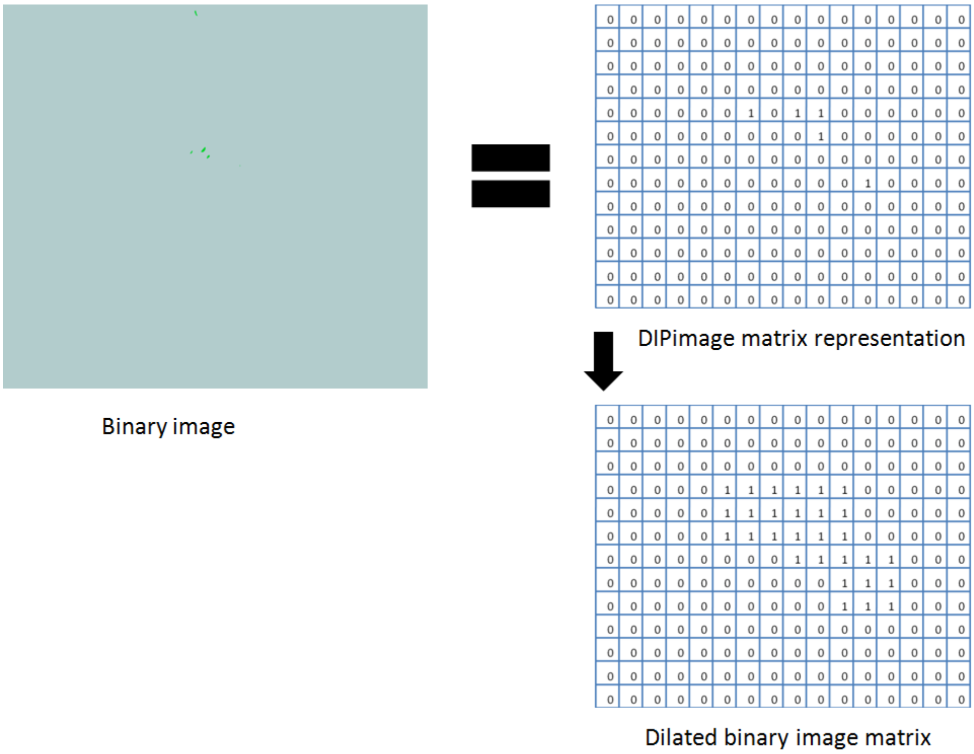

0	0	0	0	0	0	0	0	0	0	0	0	0	0	0	0
0	0	0	0	0	0	0	0	0	0	0	0	0	0	0	0
0	0	0	0	0	0	0	0	0	0	0	0	0	0	0	0
0	0	0	0	0	0	0	0	0	0	0	0	0	0	0	0
0	0	0	0	0	0	1	0	1	1	0	0	0	0	0	0
0	0	0	0	0	0	0	0	0	1	0	0	0	0	0	0
0	0	0	0	0	0	0	0	0	0	0	0	0	0	0	0
0	0	0	0	0	0	0	0	0	0	0	1	0	0	0	0
0	0	0	0	0	0	0	0	0	0	0	0	0	0	0	0
0	0	0	0	0	0	0	0	0	0	0	0	0	0	0	0
0	0	0	0	0	0	0	0	0	0	0	0	0	0	0	0
0	0	0	0	0	0	0	0	0	0	0	0	0	0	0	0
0	0	0	0	0	0	0	0	0	0	0	0	0	0	0	0

0	0	0	0	0	0	0	0	0	0	0	0	0	0	0	0
0	0	0	0	0	0	0	0	0	0	0	0	0	0	0	0
0	0	0	0	0	0	0	0	0	0	0	0	0	0	0	0
0	0	0	0	0	1	1	1	1	1	1	0	0	0	0	0
0	0	0	0	0	1	1	1	1	1	1	0	0	0	0	0
0	0	0	0	0	1	1	1	1	1	1	0	0	0	0	0
0	0	0	0	0	0	0	0	1	1	1	1	1	0	0	0
0	0	0	0	0	0	0	0	0	0	1	1	1	0	0	0
0	0	0	0	0	0	0	0	0	0	1	1	1	0	0	0
0	0	0	0	0	0	0	0	0	0	0	0	0	0	0	0
0	0	0	0	0	0	0	0	0	0	0	0	0	0	0	0
0	0	0	0	0	0	0	0	0	0	0	0	0	0	0	0
0	0	0	0	0	0	0	0	0	0	0	0	0	0	0	0

Figure 4.23: Schematic example of the DIPimage representation of a binary image before and after dilation.

The resulting parameters from the DIPimage were used for the shape classification of the particles (note that connected particles are assumed to be a one shape). The shape classification was based on quantitative data analysis done by Fang et al. [24] and Isaac et al. [48]. The shape of the particle can be represented by its shape complexity (Ω_d, where d is the dimensionality of the particle), which is a dimensionless parameter that establishes the irregularity of the shape. For 3-dimensional particles ($d = 3$), the complexity parameter can be represented as:

$$\Omega_3 \equiv \frac{A}{\pi^{1/3}(6V)^{2/3}}, \tag{4.11}$$

where A is the surface area of the particle and V is the volume of the particle. Using this equation, the surface area of the particle, A, is normalized by the surface area of a sphere with the same volume as the object, V.

Furthermore, using the diameters of the particle's equivalent ellipsoid (an ellipsoid with the same moment of inertia as the real particle), the flatness and the elongation parameters can be calculated. The flatness is defined as:

$$F = \frac{b}{c}, \tag{4.12}$$

while the elongation is defined as:

$$E = \frac{2a}{b+c}, \tag{4.13}$$

where a, b and c are the equivalent ellipsoid major, intermediate and minor semi-axes, respectively.

The flatness and elongation parameters, together with the complexity parameter, are used to characterize the shape of the particle. The shape classification can be established based on Table 4.4 (the classification was defined by Fang et al. [24]). The combination of these parameters is an unique and unambiguous quantitative approach to describe the morphology of the particles [24].

Table 4.3: Classification of different shapes based on the elongation (E), flatness (F) and 3-dimensional complexity parameter (Ω_3) [24].

Class	E [-]	F [-]	Ω_3 [-]
Sphere	-	-	$\Omega_3 \leq 1.15$
Ellipsoid	<5	<5	$1.15 < \Omega_3 < 2.5$
Rod	≥5	<5	$1.15 < \Omega_3 < 2.5$
Sheet	-	≥5	$1.15 < \Omega_3 < 2.5$
Complex object	-	-	$\Omega_3 \geq 2.5$

4.6.5. X-ray tomography of the Fe-W alloys: results and discussion

Two creep samples were analyzed using the aforementioned methods: two Fe4W alloys subjected to creep deformation at 160 MPa and 550°C. The first was subjected to the creep interrupted at the half lifetime ($t = 0.5t_R = 52$ h, called the $0.5t_R$ Fe4W sample/alloy in this chapter), which corresponds to the halted steady-state creep stage of the sample. The second one was subjected to the full creep failure ($t = t_R = 104$ h, called the t_R Fe4W sample/alloy in this chapter). The scanned samples resulted in the 3-dimensional cubic reconstructions with the dimensions of $321.5{\times}321.5{\times}321.5$ μm^3. Each reconstruction is divided into 4 regions of interest (ROI). An exemplary ROI, after local reconstruction, is presented in Fig. 4.24.

The quantitative analysis of the ROIs resulted in the determination of the volumes and filling ratios of the individual cavities in the samples. The damage volume varies from $3{\times}10^{-3}$ to $2{\times}10^3$ μm^3, while the filling ratio varies over the entire range, which means, that the empty, partially filled and fully filled cavities can be found in the samples. The classification of the shapes resulted in the determination of spherical, ellipsoidal, rod-like and complex shapes (see Table 4.4). Examples of all the shapes found in the alloys are presented in Fig. 4.25, where the filling ratios FR, precipitated volumes $V_{precipitate}$, total cavity volumes V_{cavity} and samples (where the cavities were found) are assigned to each of them.

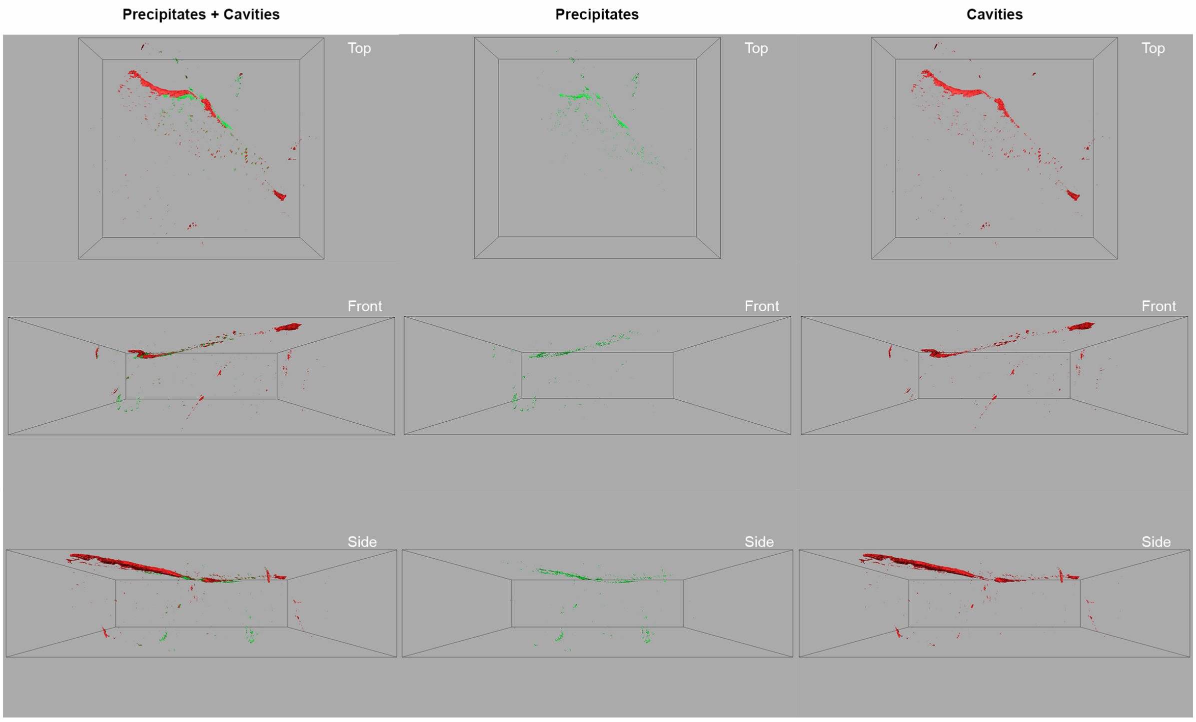

Figure 4.24: Three-dimensional reconstruction of one the slices (regions of interest) from the Fe4W alloy after creep failure (t_R) at 550°C and 160 MPa, rendered using the Avizo Fire 8.1 software. From the left side by columns: a combination of cavities and precipitates, separated precipitates, and separated cavities. The dimensions of the ROI: $80{\times}321.5{\times}321.5$ μm^3.

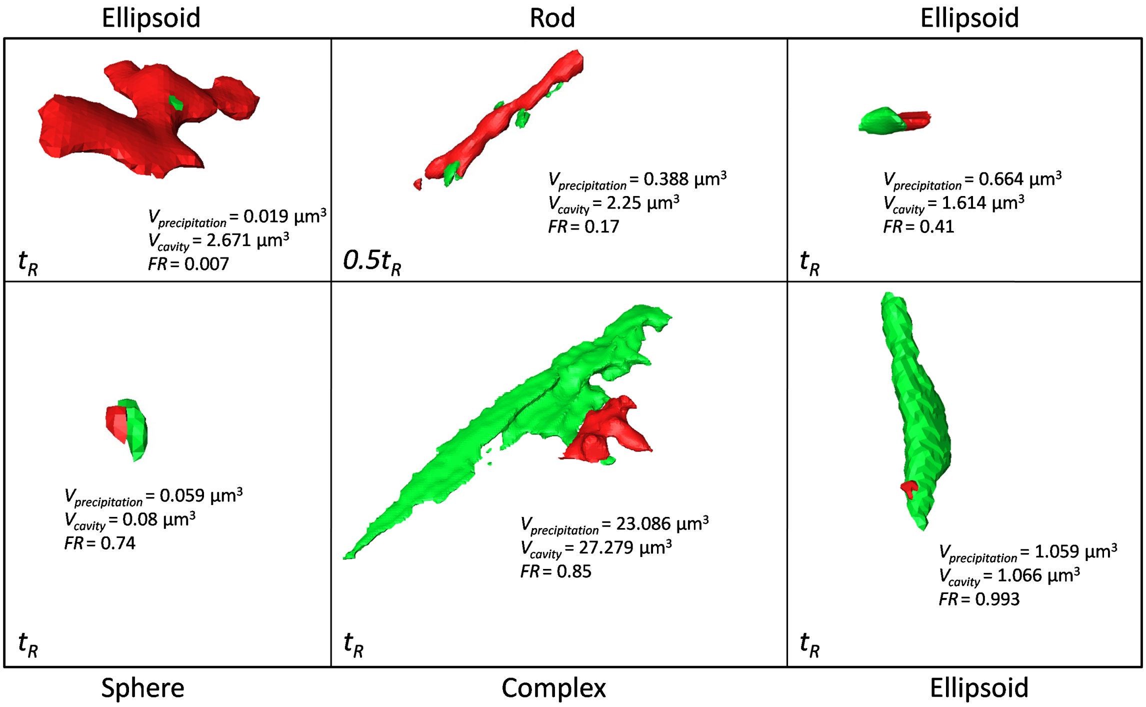

Figure 4.25: Examples of the classified precipitated cavities found in the analyzed Fe4W alloys after creep at 550°C and 160 MPa. The precipitated volumes ($V_{precipitation}$, marked in green), total cavity volumes (V_{cavity}, marked in red are the unfilled parts of the cavities), the cavity filling ratios (FR) and the Fe4W sample types (t_R or $0.5t_R$) are included in the figure.

Self healing efficiency of the Fe4W alloys

The plots of the filling ratio as a function of the cavity volume for both Fe4W samples are presented in Fig. 4.26 and Fig. 4.27. Each data point corresponds to the individual cavity, found in the $0.5t_R$ and t_R Fe4W alloys. From the figures the filling ratio distribution in the samples can be observed. For the $0.5t_R$ Fe4W sample (Fig. 4.26), the fully filled cavities comprise roughly 12% of all the cavities, while the empty cavities 62%. The average damage volume in this sample is equal to $V_{cav,av} = 1.45$ µm^3, while the average filling ratio to $FR_{av} = 0.16$. For the t_R Fe4W sample (Fig. 4.27), the fully filled cavities comprise roughly 47% of all the cavities, while the empty cavities 42%. The average damage volume in this sample is equal to $V_{cav,av} = 3.9$ µm^3, while the average filling ratio to $FR_{av} = 0.52$.

Using Fig. 4.27, an approximation for the lowest detectable cavity volume for the given resolution limit (100 nm) is established and equals $V_{min,cav} = 3 \times 10^{-3}$ µm^3. The same approximation is performed for the critical cavity volume and it results in $V_{critical,cav} = 20$ µm^3. The critical cavity volume corresponds to the maximum volume of damage that can be fully precipitated. Furthermore, from Fig. 4.26 and Fig. 4.27 it can be observed, that for the given resolution, the partial filling of the cavities cannot be determined when the filled volume is below 10^{-2} µm^3.

The self healing kinetics is controlled by a relative rates of damage formation and healing. The healing by precipitation is triggered by the nucleation of damage and is believed to become active when the cavity reaches a characteristic size V_0. Fang et al. [24] established two different cases of the cavity growth followed by precipitation: (i) the cavity growth associated with the filling by the precipitates, that takes place without linkage with other cavities and (ii) the cavity growth that links other cavities after it reaches a specific volume.

For the first case, it is assumed that the filling is activated for a cavity volume V_0. Subsequently, the cavity volume V_{cav} grows following a power law, with a simultaneous solute atom diffusion to it. Therefore, using this mindset, a filling ratio of a growing cavity (without coalescence) can be calculated using the following equation, established by Fang et al. [24]:

$$FR = \frac{k_{prec}}{k_{cav}}\left(1 - \frac{V_0}{V_{cav}}\right), \tag{4.14}$$

where k_{prec} and k_{cav} quantify the combined effect of stress and local conditions (e.g. the grain size).

Using this equation, the evolution of the filling ratio of cavities in the Fe4W alloys could be established. The value of k_{prec}/k_{cav} was chosen to be equal to 1.1, as it corresponds to the full filling for $V_{cav} = V_0$ [24]. The cavity volumes V_{cav} match the volumes of the cavities found in the samples. The chosen nucleation start volume of the cavity in the $0.5t_R$ Fe4W alloy is 3×10^{-2} μm^3. In the t_R Fe4W alloy, the chosen nucleation start volumes are: 2×10^{-2} μm^3, 2×10^{-1} μm^3 and 2 μm^3 (note: each filling ratio evolution path is established for the same growth rate). The approximated filling ratio evolution paths for the Fe4W alloys, tested at 550°C and 160 MPa, are marked by orange solid curves in Fig. 4.26 and Fig. 4.27. From these paths, it can be observed, that the filling ratio continuously increases with increasing cavity volume until the cavity is fully filled. Additionally, by comparing Fig. 4.26 and Fig. 4.27 it can be observed, that filling ratio of the $0.5t_R$ Fe4W alloy would not match the one of the t_R Fe4W alloy if it was subjected to the full creep deformation, due to the highly developed sizes of the defects, which almost approach the critical volume size.

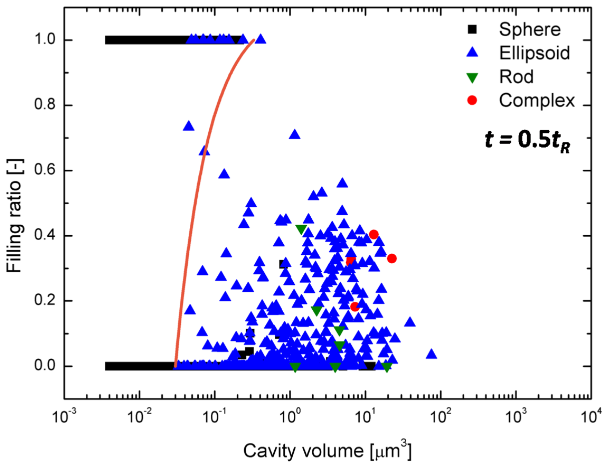

Figure 4.26: Filling ratio versus cavity volume for the $0.5t_R$ Fe4W alloy after interrupted creep at 550°C and 160 MPa. Each data point corresponds to the individual cavity found in the internal structure of the alloy. The orange curve indicates the predicted filling ratio evolution route for the cavity which the nucleation start volume is equal to 3×10^{-2} μm^3.

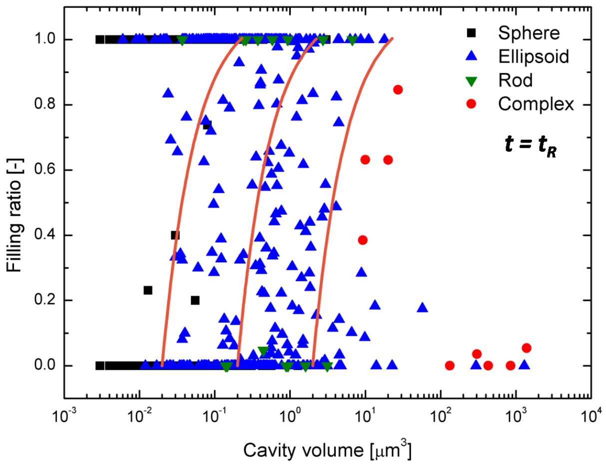

Figure 4.27: Filling ratio versus cavity volume for the t_R Fe4W alloy after creep at 550°C and 160 MPa. Each data point corresponds to the individual cavity found in the internal structure of the alloy. The orange curves indicate the predicted filling ratio evolution routes for the cavities which the nucleation start volumes are: 2×10^{-2} μm^3, 2×10^{-1} μm^3 and 2 μm^3.

Thanks to the obtained quantitative data, it has been established, that the t_R Fe4W sample shows a higher average filling ratio and average damage volume compared to the $0.5t_R$ Fe4W sample, but also a bigger amount of fully filled cavities and a higher filling ratio for the partially filled cavities. These filling ratios for the individual cavities of a specific volume are depicted in Fig. 4.28. The first conclusion that appears after seeing the data gathered in Fig. 4.28, is that by subjecting the Fe4W sample to creep deformation for a longer time, a higher filling of the damage can be achieved. This statement is only partially correct. During longer temperature exposure, the solute atoms have indeed more time to precipitate to damage, especially given that tungsten is characterized with relatively low diffusivity in α-iron (around 10^{-22} m^2/s at 550°C [76]). Although, such a big difference between the filling ratios of the cavities in the $0.5t_R$ and t_R Fe4W samples cannot only be caused by the difference in the duration of creep deformation, and has to be influenced by other factors. The reasons for the higher filling ratio of the t_R Fe4W compared to the $0.5t_R$ Fe4W sample could be: (i) the resolution limit of the X-ray tomography, which enables to detect the partially precipitated damage only above the volume of 10^{-2} μm^3, (ii) a highly developed volume of the defects and/or coalescence of the cavities in the $0.5t_R$ Fe4W sample (a big volume growth or nucleation causes an abrupt filling ratio decrease).

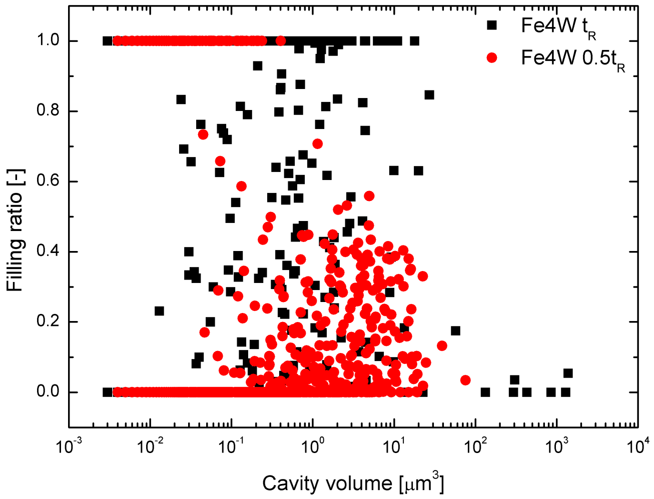

Figure 4.28: Filling ratio versus cavity volume for the t_R (in black) and $0.5t_R$ (in red) Fe4W alloys after creep at 550°C and 160 MPa.

Influence of grain-boundary orientation

It has been found, that the number of rod-shaped and complex shaped cavities is comparable in both samples. These shapes of the cavities correspond to the cavities that are created by the coalescence of multiple defects. It has also been noticed, that the ellipsoidal cavities of a higher volume constitute a high fraction of cavities in the $0.5t_R$ Fe4W sample. The cavity coalescence and big cavity volume are the reasons for the low filling ratios in the $0.5t_R$ Fe4W alloy. This is caused by the orientation of the grain boundaries along which the cavities are located. Namely, the grain boundaries parallel to the applied stress are less likely to accommodate a high rate of cavity growth or a nucleation of a big defect than grain boundaries transverse and inclined to the applied stress (or grain-boundary junctions where the diffusional void nucleation is enhanced by the opening of the junction [61]) because the production of vacancies for void growth takes place by tension across the grain boundary [46]. In Fig. 4.29 examples of two different kinds of creep damage locations are presented. These locations are: (i) grain boundaries parallel to the applied stress σ and (ii) grain boundary junction with inclined grain boundaries and a transverse grain boundary to the applied stress σ. These examples are taken from the three-dimensional reconstruction of the t_R Fe4W (rendered by Avizo Fire 8.1) as this sample possesses a bigger variety of grain-boundary orientations compared to the $0.5t_R$ Fe4W sample. Although, the grain boundaries are not perfectly transverse or parallel to the applied stress, they do show the dependency of grain boundary orientation on the cavity shape, which is showed in Table 4.4.

As the flatness parameter is mainly used in distinguishing the sheet-shape of the cavity, it has been ignored in shape classification of the cavities considered in Table 4.4. From the table it can be seen, that the cavities are comparable in their average complexity parameter $\Omega_{3,av}$, therefore, the shape classification can only be based on their average elongation parameter $E_{av.}$ The cavities located at the grain-boundary junction (with transverse and inclined grain boundaries) have the highest average elongation parameter, which confirms the presence of many complex and elongated cavities. This observation confirms the fact, that inclined and transverse grain boundaries, and grain boundary junctions, are the locations for cavities that are complex in shape and large in volume, which is caused by cavity coalescence, high cavity growth rate or nucleation of a big volume cavity. This further confirms that the grain boundary orientations other than parallel to the applied stress are the most favourable locations for cavity growth in the alloys.

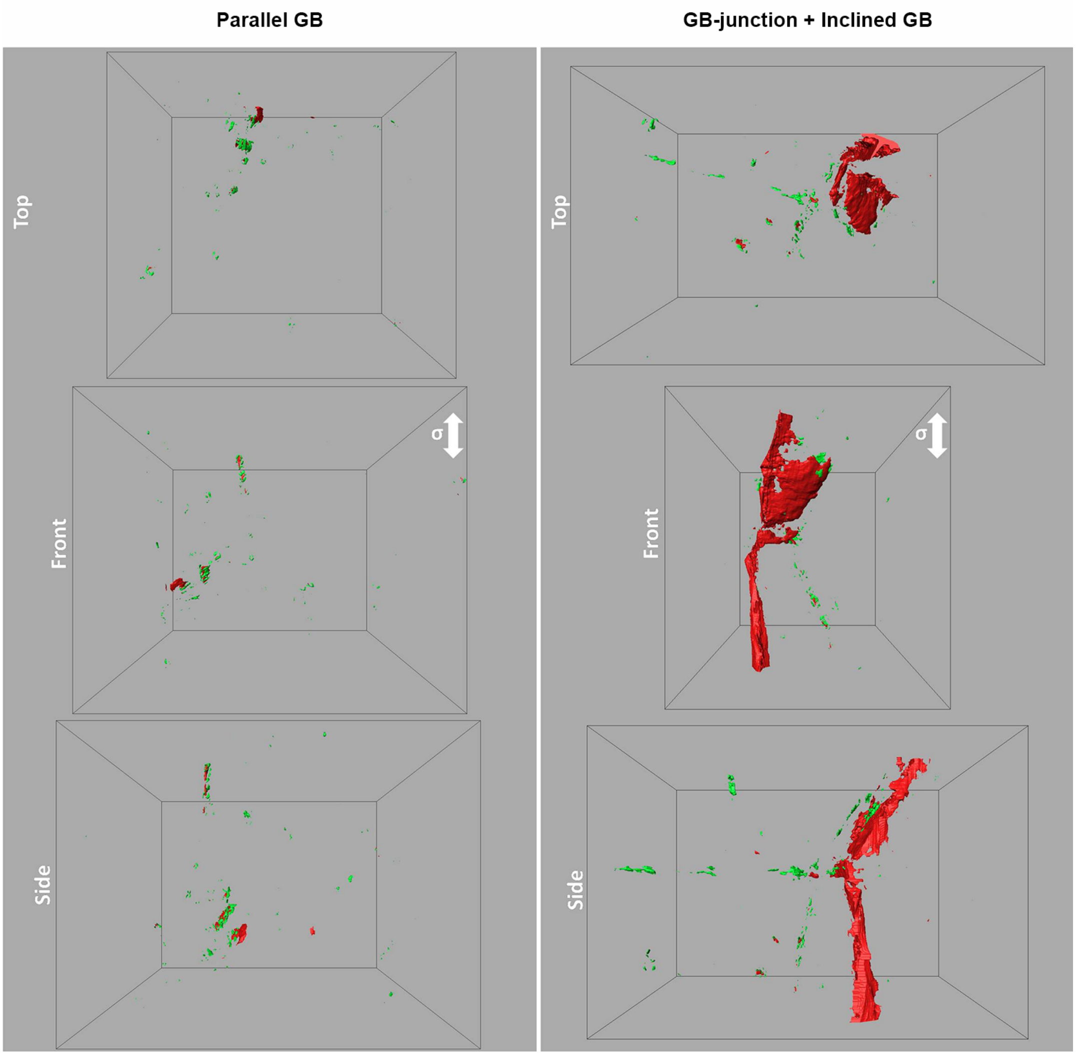

Figure 4.29: Three-dimensional reconstruction of two regions of interest from the Fe4W alloy after creep failure (t_R) at 550°C and 160 MPa, rendered using the Avizo Fire 8.1 software. From the left side by columns: a ROI containing a grain boundary parallel to the applied stress (σ), and a ROI containing a grain-boundary junction with grain boundaries inclined and transverse to the applied stress (σ).

Table 4.4: The average flatness parameters E_{av} and complexity parameters $\Omega_{3,av}$ for all the grain-boundary types depicted in Fig. 4.29.

GB type	E_{av} [-]	$\Omega_{3,av}$ [-]
Parallel GB	2.52	1.40
GB-junction + inclined/transverse GB	2.85	1.42

Cavity shape evolution

Increasing volume of a cavity leads to its shape evolution. The shape development of the cavities goes through the following path: sphere/ellipsoid → sheet/rod/complex. It is rare for the cavities to follow a different sequence with their increasing volume. It is strictly connected with cavity growth during creep deformation. Cavities grow as spheres (lens-shapes – equilibrium shape), when their growth is controlled by grain-boundary diffusion or as ellipsoids (crack-like shape – a non-equilibrium shape), when their growth is controlled by cavity surface diffusion. Subsequently, the cavities grow and coalesce into sheet-like, rod-like or complex defects.

Fig. 4.30 shows four separate plots of filling ratio as a function of cavity volume for the individual cavities of specific shapes found in the internal structures of the t_R and $0.5t_R$ Fe4W samples. In Fig. 4.30a-b it can be observed, that there is a higher number of ellipsoidal cavities compared to the number of spherical cavities, in the samples, which suggests that the growth of the damage in the Fe4W alloys is governed by cavity surface diffusion. In Fig. 4.30c-d it can be observed, that rod-like and complex shapes in the Fe4W samples are of a higher volume, which can indisputably be regarded as the coalescence of spherical or ellipsoidal cavities.

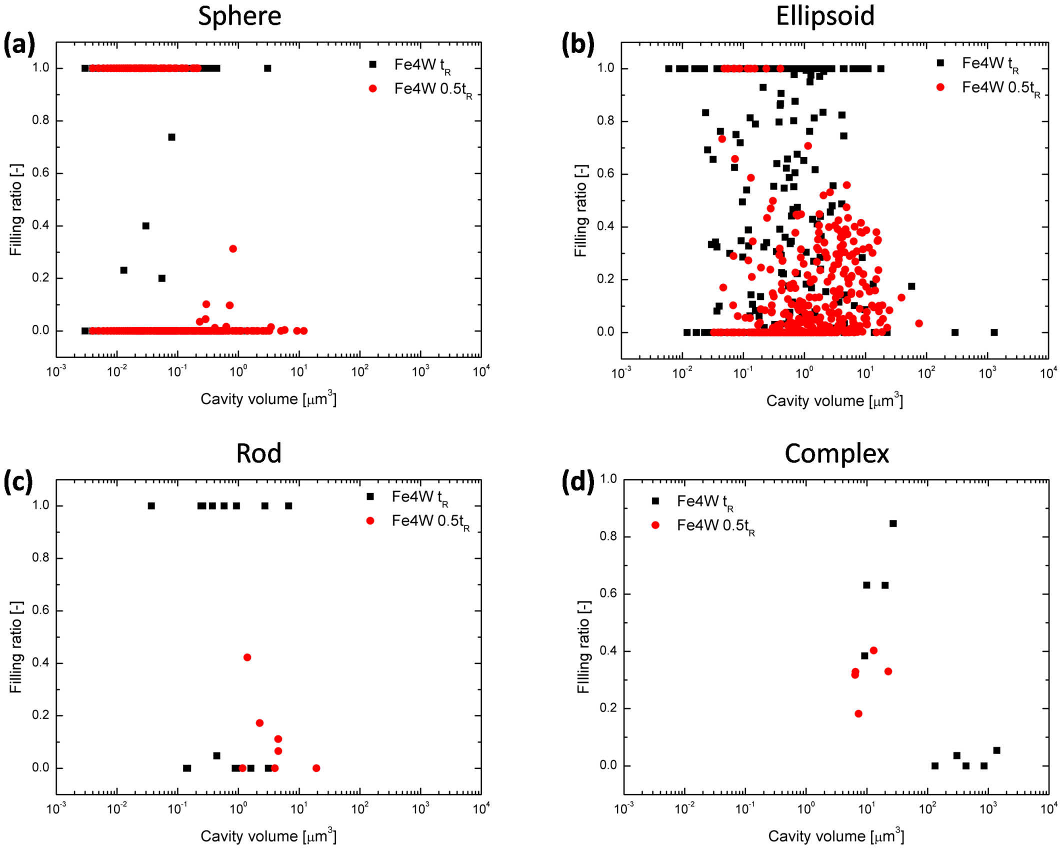

Figure 4.30: Filling ratio versus cavity volume plots of the t_R (marked in black) and $0.5t_R$ (marked in red) Fe4W samples after creep at 550°C and 160 MPa, with the division into damage shapes. (a) Spheres, (b) ellipsoids, (c) rods and (d) complex shapes.

From Fig. 4.30 it can also be observed, that the most favourable morphology for self healing are the spherical and ellipsoidal shapes. These shapes show the highest average filling ratios and the highest percentage of full filling for both t_R and $0.5t_R$ samples. This is connected with the fact, that these are the shapes of the cavities that activate the precipitation by their nucleation. The more complex shapes do not show full filling ability, which is strictly connected with the fact, that their existence is caused by cavity linkage, so their high cavity growth and a sudden volume change cannot possibly be matched by the rate of solute diffusion.

4.7. Conclusions and recommendations

It has been proven, that autonomous full and partial repair of creep-induced cavities by the precipitation of the second phase in Fe-W alloys is achievable. It has been found, that the cavities which are nucleated and grown on the grain boundaries of Fe4W alloys can be effectively healed if their volume does not exceed the critical cavity volume, $V_{critical,cav} = 20\ \mu\text{m}^3$. Furthermore, by means of the simplified model of the filling ratio evolution, it has been proven that the filling ratio of the cavities increases with the increasing volume of a defect as long as no cavity linkage is accommodated. It has been observed, that the sample subjected to creep failure shows a higher cavity filling by the precipitation of the second phase than the one subjected to interrupted creep deformation ($t = 0.5t_R$). This result has been attributed to a more pronounced cavity coalescence/cavity growth and a nucleation of big defects in the sample subjected to the interrupted deformation. This phenomena are influence by the grain-boundary orientation. The visual inspection of the rendered cavity-precipitate structures in both samples proves that the sample after interrupted creep possesses numerous grain boundaries more favourable for coalescence, big volume nucleation and accelerated cavity growth. It has also been found that the growth of the cavities in the Fe4W alloys is most likely governed by cavity surface diffusion as the majority of the cavities take form of the crack-like non-equilibrium shape. Furthermore, from the experimental testing, proceeding the Fe-W alloys' tomographic data analysis, several additional conclusions can be made. Namely:

- The current solution heat treatment of the alloys does not fully dissolve all the second phases, which is indicated by the presence of bulk precipitation in the tested samples.
- The grain size becomes the dominant factor influencing the creep deformation of the alloys when the grain size diameter is greater than the thickness of a sample.
- Fe-W shows no bulk precipitation during creep deformation, which proves that the energy barrier for homogeneous precipitation, caused by the big sizes of tungsten atoms, is relatively high in Fe-W alloys.
- The creep mechanism governing the deformation of Fe-W alloys is a combination of volume diffusion creep and dislocation creep, which was proven by the calculated stress exponent and activation energy for the Fe4W alloys.
- The volume diffusion is predominantly governing the solute transport to the creep-induced damage, which was revealed by SEM micrographs that show the segregation of small precipitates at the edges of the cavities.
- The small amount of bulk precipitates induce void nucleation in the bulk of the material, which might decrease the strength of the material.

The following recommendations for future work with Fe-W alloys can be made based on the outcomes of this project:

- In order to dissolve all the bulk precipitates in Fe-W alloys, a different approach to the solution heat treatment of the samples has to be applied, which most possibly involves longer annealing time and/or increased temperature.
- In order to obtain reproducible creep tests for the Fe6W alloys, an effective grain reduction procedure has to be found, which most probably involves recrystallization of the grains and/or the reduction of samples' thickness or improved primary production conditions.
- In order to investigate the stress and temperature influence on the filling ratio of cavities and cavity volume sizes in Fe-W alloys, X-ray tomographic processing has to be performed on the samples priory subjected to creep deformation in different conditions.
- In order to examine the concentration of tungsten on the filling ratio of cavities, different compositions of Fe-W alloys have to be introduced into the experimental procedure.
- In order to more precisely evaluate the grain boundary type and orientation influence on the filling ratio of the cavities, and cavity volume and shapes, more in-depth investigation of the reconstructed cavity-precipitate structures has to be undertaken. This procedure has to involve the exact reconstruction of grain boundaries present in the alloys, using the provided tomographic scans.

5

Influence of ageing processes on Fe-W alloys

In the previous chapter, the self-healing effect that takes place during creep deformation has been described. A mechanical load was used to induce damage inside the material, while, at the same time, the temperature and stress were controlling the solute atom diffusion and the subsequent second phase precipitation. In contrast, this chapter intends to describe the precipitation of a second phase at indentation-induced surface micro-deformations, which takes place during the heat treatment of the iron-tungsten alloys. The most important difference, with the situation for high-temperature creep is that all damage was introduced to the samples as performed at room temperature with a subsequent elevated temperature exposure. This chapter aims to evaluate the precipitation of the second phase at defects by diffusion of solute atoms in elevated temperature, when an external stress is removed. Furthermore, this chapter also aims to establish the changes of the alloys' properties during the ageing process. This evaluation entails the measurements of mechanical parameters, such as hardness.

In the beginning, the hardness testing of the alloys is introduced to assess the change of the materials' strength during interrupted heat treatment, which can indirectly convey information about solute diffusion and precipitation in the alloys. The chapter continues with the study of deformation-induced defects, their surface precipitation after ageing and a detailed explanation of its nature. The chapter finishes with conclusions and recommendations.

5.1. Hardness measurements

Hardness can be defined as a resistance of a material to a local plastic deformation [77]. Vickers micro-hardness measurements were performed, using a micro-hardness tester, on four iron-tungsten samples: Fe4W and Fe6W as-quenched, and Fe4W and Fe6W as-quenched and tensile pre-strained at room temperature with $\epsilon = 0.32$. These tests (under the load of 0.5 N) were conducted every time the samples were subjected to an interrupted ageing. The procedure of their ageing is described in the following subsection. The exact composition of the samples is presented in Table 4.1. The as-quenched state of the samples refers to their prior solution heat treatment with the subsequent rapid water-quenching, described in the previous chapter. In this chapter, the as-quenched samples are called undeformed samples, while the as-quenched and pre-strained samples are called deformed samples.

5.1.1. Heat treatment of hardness samples

Ageing of the samples was performed to investigate the hardness development of the Fe-W alloys over ageing time. For this purpose, an electrical vacuum furnace with an external turbo-pump was used. The furnace heats using Eddy current by a time-dependent magnetic field from a solenoid coil [33]. The vacuum that can be reached by the furnace is slightly below 5×10^{-4} mbar, while the turbo-pump is able to decrease it down to 2×10^{-5} mbar. The vacuum is used to avert the oxidation of the alloys during the heat treatment.

In order to prevent the samples from moving inside the chamber of the furnace, due to a produced magnetic field, a metallic holder with a ceramic insert was employed to serve as a sample support. Another purpose of such a holder is to obtain an even temperature distribution over the samples during the ageing process. Whereas, the purpose of a ceramic insert is to limit the contact between the metallic wedge and the samples. To control the temperature inside the chamber of the furnace, an Eurotherm controller was used, that was connected to a thermocouple type K with two ends, one laying near the metallic holder, and the second one hanging in the ambient air outside the furnace [33].

The total ageing time was established to be 200 hours and the process was interrupted at selected times for hardness measurements. The times at which the measurements were taken are marked on the hardness versus age time plots in Fig. 5.1 and Fig. 5.2. Every time the furnace was heated up to a temperature of 580°C with a heating rate of 10°C/min. The maximum temperature was reached approximately after 55 minutes. Each time the process was halted, the cooling of the furnace was done under sustained vacuum by letting it equalize with room temperature, which lasted approximately 2.5 hours.

5.1.2. Hardness results and discussion

Interrupted Vickers micro-hardness measurements yielded results that are visible in Fig. 5.1 (Fe4W alloys) and Fig. 5.2 (Fe6W alloys). The broad standard deviation of the measurement points is assigned to the measured hardness, that significantly changes with the position of the micro-indentation. Sometimes a grain boundary, a precipitate, a prior indent (higher hardness) or the inside of a grain without any defects (lower hardness) was indented.

From Fig. 5.1 and Fig. 5.2 it can be observed, that higher hardness of the deformed samples, compared to the undeformed ones, is registered. This can be attributed to strain hardening due to multiplication of dislocations, which decreases the average separation distance between dislocations. This also increases the resistance to dislocation motion, together with the imposed stress required to deform an alloy, which results in greater hardness values [12].

Furthermore, in the early stages of the ageing process constant hardness values are registered for the deformed samples. This continues until 8 and 10 hours of ageing, for Fe4W and Fe6W, respectively. The so-called plateau in hardness (the constant hardness over ageing time) is rarely found. Usually the hardness increases and reaches a peak (peak-ageing), before a decay (overageing), due to precipitation hardening and subsequent precipitation coarsening. The hardness plateau in case of the Fe-Mo alloys was assigned by Zhang [86] to a balance between precipitation hardening and a counteracting dislocation recovery. The previously introduced dislocations (by tensile deformation) are migrating into grain boundaries, where they can be annihilated, but at the same time, their motion is being impeded by the solute atoms clustering at the dislocations.

In Fe-W alloys, the diffusion of tungsten atoms in the α-Fe matrix is relatively slow compared to the rate of dislocation recovery in the matrix. Therefore, the dislocation impeding is only effective in the case of a high dislocation density (i.e. the deformed samples) – when tungsten atoms require shorter distances to diffuse and segregate at dislocations. At a certain point, when the dislocation density decreases, the dislocation recovery gradually stops being compensated by precipitation hardening and the hardness of the deformed samples drops (red fitting curves - Fig. 5.1 and Fig. 5.2). It reduces to the time at which it coincides with the hardness of the undeformed samples, i.e. the initial state before deformation [11, 19, 21]. Another explanation for the hardness reduction of the deformed samples could be the coarsening of precipitates (overageing) and the consequent material softening, but is unlikely as the undeformed samples do not show any hardness decrease after the same ageing time, which would be expected in this case [11].

The constant hardness (black fitting curves - Fig. 5.1 and Fig. 5.2) in the case of the undeformed samples is caused by a lack of diffusion or dislocation motion events inside the material. Meaning, that the diffusion through the iron matrix is too low ($D = 5.92 \times 10^{-21}$ m^2/s at 580°C [76]) to mobilize and agglomerate the tungsten atoms at the dislocations, which prevents precipitation hardening. Moreover, supersaturated metals are characterized to be defect-free, or at least low in dislocation density, which makes a major dislocation recovery impossible to take place. Additionally, no overageing effect at such an early stage of annealing can appear (too few particles).

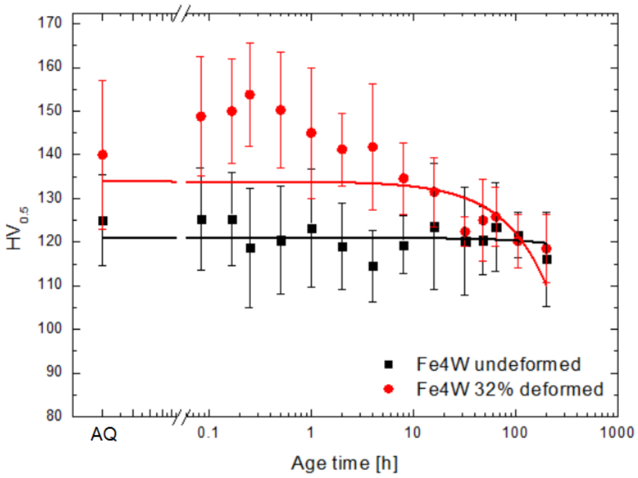

Figure 5.1: Hardness of the Fe4W undefromed and the Fe4W deformed samples as a function of the ageing time. The alloys were aged for 200 h at 580°.

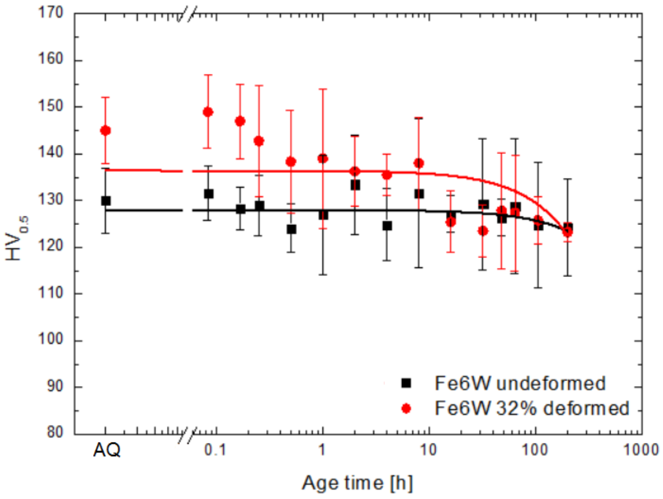

Figure 5.2: Hardness of the Fe6W undeformed and the Fe6W deformed alloys as a function of the ageing time. The alloys aged for 200 h at 580°.

5.2. Precipitation of tungsten at micro-indented sites

Scanning electron microscopy (SEM) images of the micro-indented (using the hardness tester) and aged (for 140 h at 600°C) creep Fe-W sample, that was supersaturated before creep fracture, revealed an interesting phenomenon. Namely, a precipitation of nano-particles of a secondary phase on the surface of the indentation (see Fig. 5.3). Energy-dispersive spectroscopy (EDS) spot analysis showed various results of the composition of the nano-precipitates. The results can be seen in Fig. 5.4. In Fig. 5.4c it can be observed, that the composition of the small precipitates is not conclusive, as the concentration of tungsten in the phase varies from 8 to 18 wt.%. A phase with the observed compositions is not predicted by the iron-tungsten phase diagram. The only conclusion that can be made from these results is that the nano-precipitate is most likely a Fe_2W Laves phase (62 wt.% W and 38 wt.% Fe), but the spatial resolution of EDS equipment is too low to pick up the exact composition of such a small particle. In other words, the probed volume of the material below the precipitate, which X-rays are emitted from, is simply too bulky and contains too much α-Fe matrix compared to the amount of the secondary phase. As a result, the composition of the precipitate is averaged over a bigger volume than its actual size [25]. In order to gain a greater knowledge of the precipitation at the micro-deformed sites, several other samples from Fe-W material were tested and investigated.

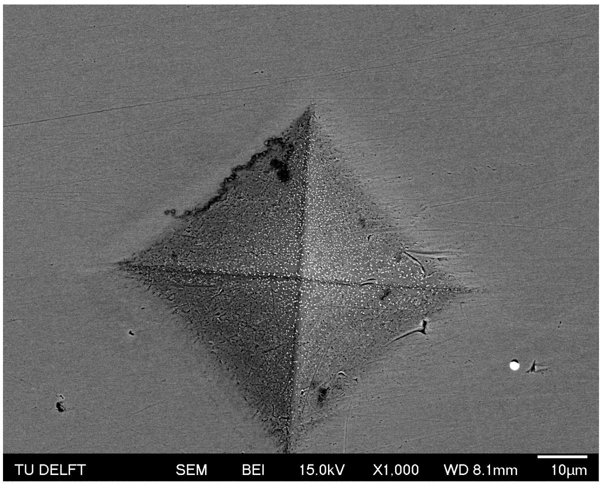

Figure 5.3: A back scattering SEM image (magnification of 1,000×) of the second phase precipitation (bright cuboid shapes inside the indentation) at the indentation site in the Fe6W fractured creep sample after aging at 600°C.

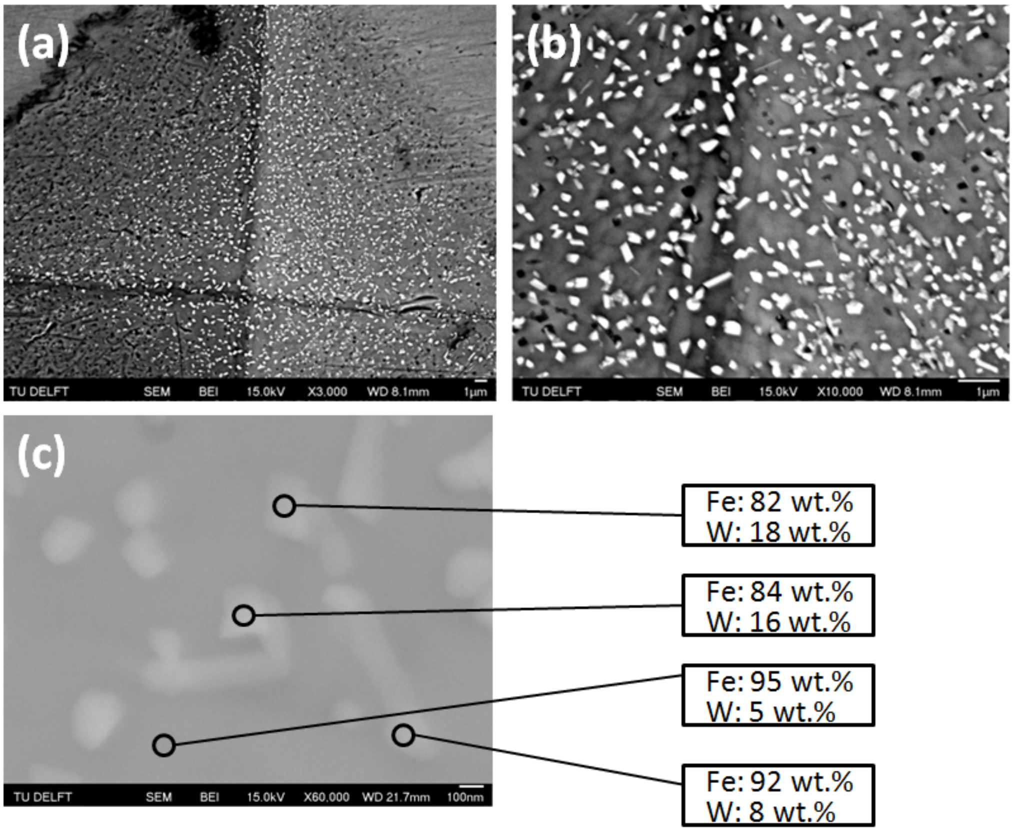

Figure 5.4: Back scattering SEM pictures of the Fe6W sample from Fig. 5.3, (a) with a magnification of 3,000×, (b) 10,000× and (c) 60,000×, combined with the results from EDS composition obtained from four different surface precipitation spots.

5.2.1. Precipitation at indentation

The alloys chosen for this investigation were the same as the ones used for the hardness tests: Fe4W and Fe6W undeformed, and Fe4W and Fe6W deformed. Then, all samples were subjected to plastic deformation by micro-indentation (using a micro-hardness tester with the load of 0.5 N) and aged for 140 hours at 600°C. Due to deformation, the dislocations density inside the grains increases. Given that the alloys are supersaturated, the nucleation of new dislocations during plastic deformation attracts the solute atoms to their cores, where they segregate. As mentioned in the third chapter, the reason for solute atoms to migrate to defects, such as dislocations, is associated with the reduction in the energy of elastic distortion of the lattice. The incorporation of solute atoms into the crystal lattice by supersaturation results in an elastic distortion of the atomic bonds. In order to reduce this energy, solute atoms tend to move from a tightly-packed crystal lattice to more lower-density defects. Additionally, an ageing process enhances the migration of solute atoms to matrix mismatches and/or defects as it provides the necessary energy for the solute atoms to diffuse through the lattice into these sites [10, 18, 45].

An excellent example of solute migration, and a subsequent precipitation of a second phase at indentation sites has been presented by Zhang in the Fe-Au-B-N alloy [86]. As it can be seen in Fig. 5.5, the precipitation of a new phase appeared at the surface of a Knoop indentation, which was induced prior to the ageing process, that lasted 64 hours at 550°C. In the Fe-Au-B-N alloy, the increased bulk diffusion by dislocations causes the precipitation of Au-rich particles. Dislocations, introduced by the indentation, speed up the local response in the deformed areas as they attract the solute and serve as short-circuit diffusion paths into open-volume defects, where the solute can precipitate [71, 86]. A similar behaviour is expected from Fe-W alloys.

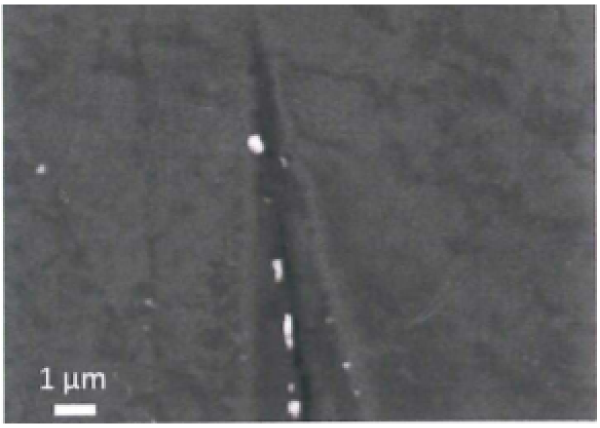

Figure 5.5: Back-scattering SEM image of the Fe-Au-B-N alloy with a Knopp indentation after ageing for 64 h at 550°C [86].

5.2.2. Results and discussion

The 'fresh' indentations on Fe4W and Fe6W alloys can be seen in Fig. 5.6 and Fig. 5.7, respectively. From the micrographs, it can be seen that there is no precipitation at the deformed sites. The back scattering SEM images of the indentations were also taken after the ageing process and are presented in Figures 5.8-11.

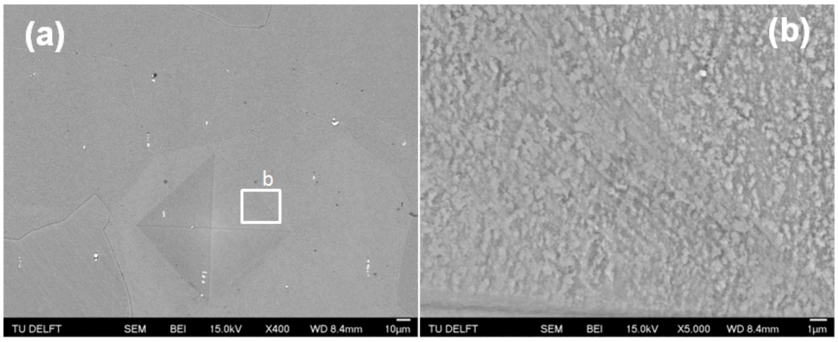

Figure 5.6: Back scattering SEM images of the freshly indented Fe4W undeformed sample with the magnification of (a) 400× and (b) 5,000×.

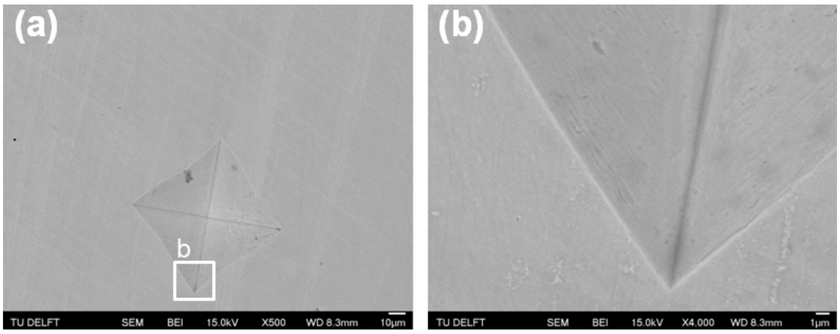

Figure 5.7: Back scattering SEM images of the freshly indented Fe6W undeformed sample with the magnification of (a) 500× and (b) 4,000×.

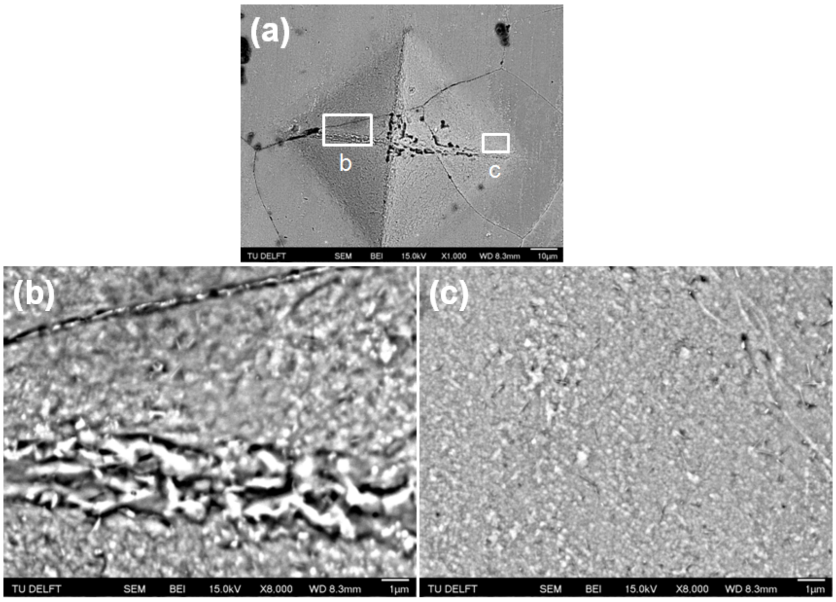

Figure 5.8: Back scattering SEM images of the indented undeformed Fe4W sample (after ageing for 140 hours at 600°C) with the magnification of (a) 1,000× , (b) 8,000× and (c) 8,000×.

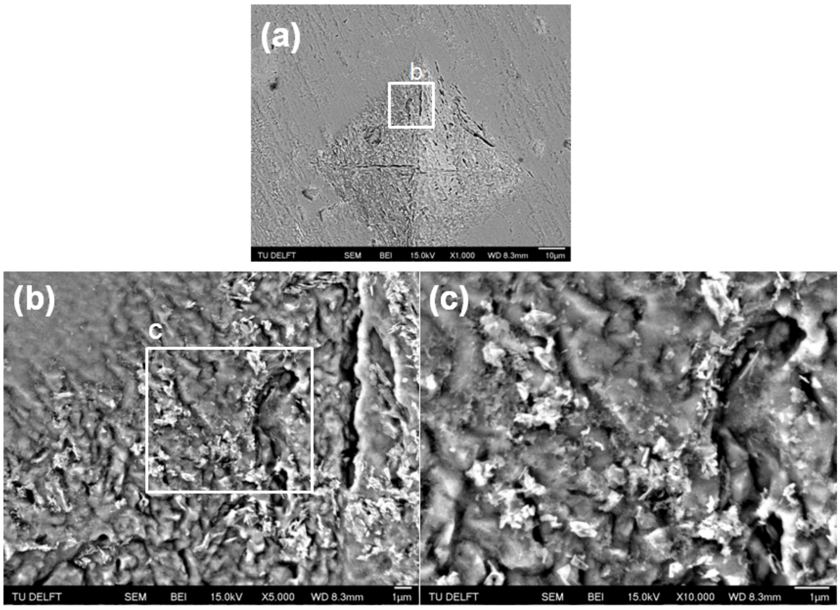

Figure 5.9: Back scattering SEM images of the indented aged undeformed Fe6W sample (after ageing for 140 hours at 600°C) with the magnification of (a) 1,000×, (b) 5,000× and (c) 10,000×.

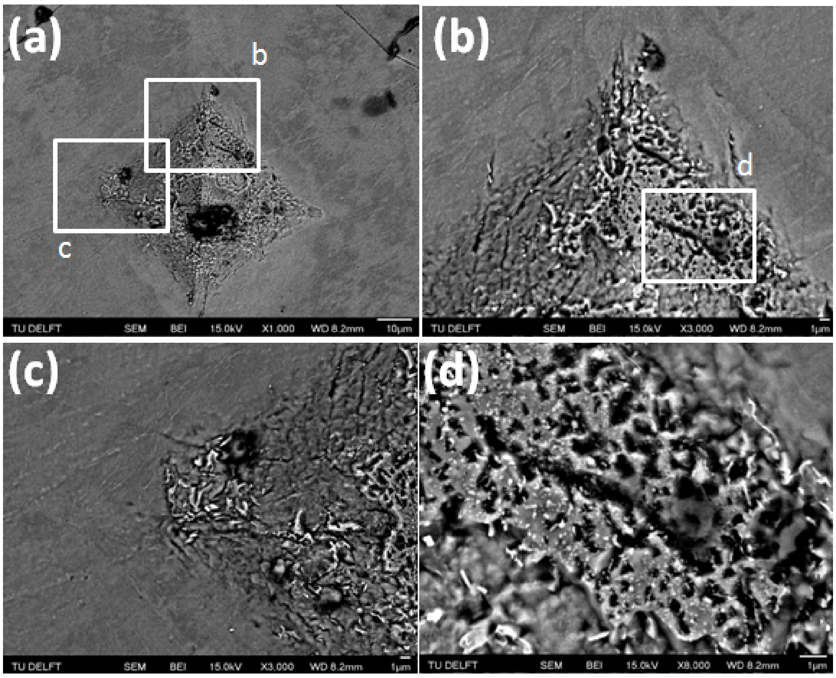

Figure 5.10: Back scattering SEM images of the indented deformed ($\epsilon = 0.32$, $\dot{\epsilon} = 1.33 \times 10^{-4}$ s^{-1}) Fe4W sample (after ageing for 140 hours at 600°C) with the magnification of (a) 1,000×, (b) 3,000×, (c) 3,000× and (d) 8,000×.

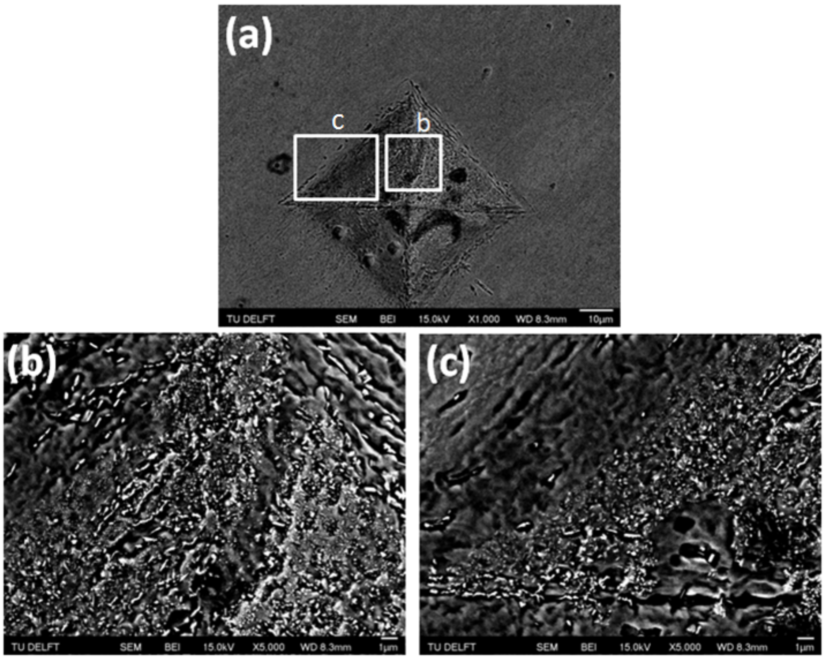

Figure 5.11: Back scattering SEM images of the indented aged deformed ($\epsilon = 0.32$, $\dot{\epsilon} = 1.33 \times 10^{-4}$ s^{-1}) Fe6W sample (after ageing for 140 hours at 600°C) with the magnification of (a) 1,000×, (b) 5,000× and (c) 5,000×.

From the figures above, several observations can be made:

- When comparing the samples before and after the ageing process, it is apparent, that the precipitation of the small particles is visible only after the high temperature exposure.
- The precipitation of the second phase takes place exclusively inside the indentations and it is nowhere visible in the bulk of the material.
- The precipitates tend to form cuboid shapes if they have no big defects to precipitate into (see Fig. 5.3).
- There is no obvious link connecting the different tungsten concentrations to the precipitation at the indentations.
- From the visual inspection it can be observed, that the greater dislocation density of the deformed samples does not affect the precipitation after ageing.

The micrographs showed the presence of multiple defects inside the indentations, that were not in those locations before indenting. This observation is pointed out in the book "Dislocations in Solids" by Nabarro and Hirth, where it is concluded as "not resolved very well" [60]. However, thanks to this observation, the presence of small cuboid-like precipitates (Fig. 5.3) could be interpreted as a second phase precipitation at nano-defects induced by micro-indentation. This theory is supported by the presence of black spots that lie in the vicinity of the nano-precipitates, which could be unfilled nano-defects. Their existence was originally assigned to precipitate chip-offs, caused by sample cleaning (an ultrasonic bath cleaning). Another interesting explanation for the small cuboid-shaped precipitates could be the solute atom agglomeration at dislocations, their dislocation diffusion to the surface of the indentation, and the subsequent precipitation and coarsening to the observed size [9].

When seeing that all the samples show precipitation at the indentation sites, the question about the phase structure and composition emerges. EDS spot measurements and EDS line scans were performed on the samples, but were abandoned as they did not show any conclusive results. They were as inconclusive as the scans done for the sample presented in Fig. 5.3. Therefore, X-ray diffraction (XRD) was conducted on one of the materials (the undeformed indented Fe4W sample before and after ageing, Fig. 5.6 and Fig. 5.8). In such a way, the crystal structure of the precipitated phase could be assessed, which can result in the identification of the phase composition and structure, if the investigated phase is known. As can be seen in Fig. 5.12 (red curve), two small peaks at the diffracted angles (2θ) of 37.900° and 41.840° appeared for the crystallographic planes with Miller indices of {110} and {103}, characteristic for a Laves phase Fe_2W (with a hexagonal $MgZn_2$ structure) [20]. However, the intensities of the peaks do not match the ones obtained from the data sheets for Fe_2W (marked as α, the characteristic peak for α-Fe). Therefore, the structural data obtained from X-ray diffraction is not entirely clear and conclusive and nothing can be said with certainty about the composition and structure of the micro-indentation precipitates. On the other hand, no other phases have been identified and previous studies on these materials clearly confirm, that only the precipitation of Fe_2W is observed after ageing at 600°C [20].

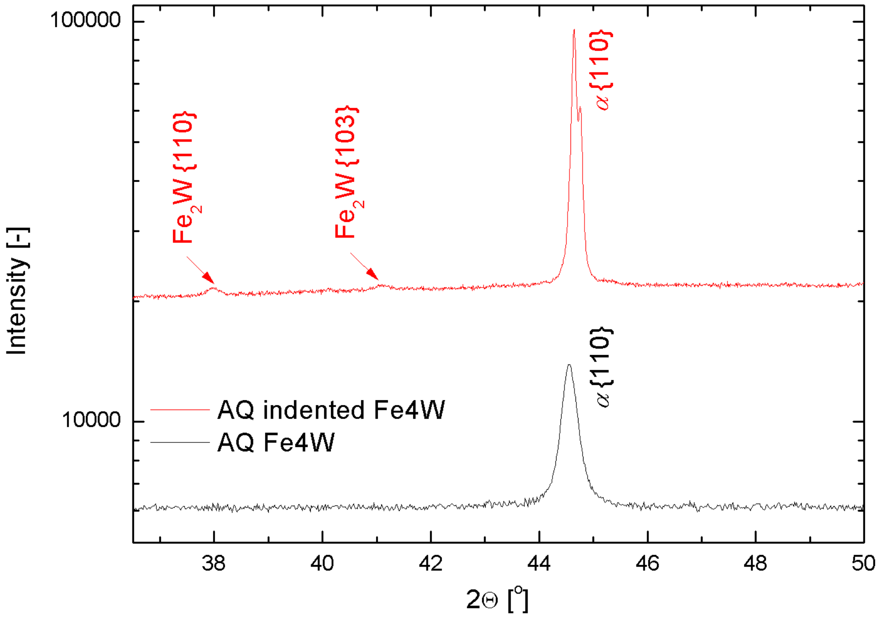

Figure 5.12: XRD spectra for the undeformed indented Fe4W sample after ageing at 600°C for 140 h (red) and for undeformed indented Fe4W before ageing (black).

5.3. Conclusions and recommendations

It was found that, the solute atoms are able to impede moving dislocations when the dislocation density is relatively high (after tensile deformation). However, these solute-dislocation interactions are hindered after ageing for several hours at 600°C, when the dislocation density is decreased by the dislocation recovery process. This observation also confirms the slow tungsten diffusion in bcc-iron [76]. These phenomena were observed during hardness measurements of the deformed and the undeformed Fe-W alloys, and were confirmed by the lack of peak-ageing and the presence of the hardness plateau. The slow diffusion of tungsten and the big sizes of the grains (see Fig. 4.4) contribute to the constant hardness of the alloys after 200 hours of ageing. There is no precipitation hardening in the materials, due to the long diffusion paths and the low rate of the solute transport into the grain boundaries.

The studies on the precipitation at micro-indentations after ageing showed the precipitation of Fe_2W phase at the surface defects induced by local deformation. This results are compliant with the ones obtained during creep deformation of the Fe-W alloys, where the preferential precipitation sites are the grain-boundary defects. This observation confirms that the homogeneous precipitation in Fe-W alloys is unattainable.

The influence of the applied stress on the precipitation at the defects cannot be assessed as the SEM micrographs revealed the second phase particles for both the creep and the aged samples. Understandably, the amount of the precipitated second phase could not be compared between the creep and the aged alloys, due to the lack of quantitative analysis on the aged samples. Therefore, the influence applied stress on the precipitation of the second phase at defects still remains unsolved.

The following recommendations can be made for future research:

- In order to thoroughly investigate the micro-indentation defects, a more sophisticated characterization technique is advised (TEM or X-ray tomography). Such a technique could help to reveal the spatial shapes of the defects and precipitates, which can lead to a more detailed explanation for their presence.
- In order to observe the more extended hardness development of Fe-W alloys subjected to high temperature, a longer ageing of all the samples is advised.
- In order to assess the influence of the subjecting stress on the rate of precipitation, a new research with quantitative analysis, comparing the precipitation during ageing to the precipitation during creep deformation is advised.

6

Finite element calculations on the self-healing of a creep cavity by solute diffusion

So far, the self-healing effect has been presented and evaluated by means of experimental work. The mechanism of nucleation, growth and subsequent filling of creep cavities is not always straightforward, as could be seen in the previous chapters. Although, the shapes of the nucleated cavities, in the initial stages, do not always resemble the ideal shape that is the subject of theoretical studies, the ideal representation helps to understand the possible events taking place, when a (lens-shaped) cavity is created on a grain boundary in a supersaturated alloy, that is subjected to creep deformation.

The aim of this chapter is to convey the knowledge gained on the diffusional flow of solute atoms (self healing process) to a lens-shaped creep cavity, by means of finite element modelling. The choice of the lens-shaped cavity was driven by the fact, that it is the equilibrium shape of a creep-induced intergranular cavity, that can be usually encountered in creep-resistant steels. Such a defect is frequently nucleated on grain boundaries oriented transversely to the applied stress and is propagated by diffusive creep cavity growth mechanisms. The goal of this chapter is to evaluate the diffusional character of solute atoms during creep cavity filling, and the time that it takes the solute to fill the entire creep cavity, depending on four varying parameters: the volume and grain boundary diffusion coefficients, the creep cavity radius and the distance separating a cavity from a neighbouring one that lies on the same grain boundary. The calculations do not focus on one particular material (like for instance, the iron-tungsten system), but are more general to extend their usefulness for future self-healing research on metals. More details are presented in the following sections. Firstly, the current understanding of cavity filling by diffusional mechanisms is presented. This is followed by the chosen approach and the results obtained from the computations. The chapter finishes with conclusions and recommendations for future experimental and modelling research.

6.1. Creep cavity diffusional filling kinetics

The subject of creep cavity nucleation and growth has been outlined at the beginning of this work. This section solely focuses on the void filling by volume and grain boundary solute diffusion. Since in the modelling only one cavity (that has neighbouring cavities along the same grain boundary) is considered, the simplest case of concentration-driven diffusion was taken into account. The transport of solute by diffusion can be represented by Fick's first law of self-diffusion. In order to adjust the equation to a three-dimensional α-iron matrix, the diffusional flux (an amount solute atoms that diffuses through an unit of surface area in an unit of time) is defined as follows: [43]:

$$\vec{J} = -\frac{D}{\Omega}\vec{\nabla}c, \tag{6.1}$$

where D is the diffusivity, Ω is the atomic volume of the solute atoms (in the model: the atomic volume of a bcc iron atom) and c is the solute concentration in atomic fraction [80].

Then, the integrated flux of the solute from the bulk material to the cavity can be assessed at the surface of the cavity edge by using the following equation:

$$\frac{dN}{dt} = -\oiint_S \vec{J} \cdot \vec{dS}. \tag{6.2}$$

where S stands for the surface of the cavity and N for a number of atoms diffusing into the cavity through its surface over time t.

In the model a continuous diffusion of solute atoms to the grain boundary and the cavity was considered. The flux into the cavity was determined at the entire cavity edge. This means that, the solute transport from the volume and the adjoining grain boundary was investigated. Additionally, the volume diffusion towards the grain boundary was determined. The volume and the grain boundary were supersaturated with solute at the beginning of every simulation. In reality, the diffusion of solute atoms is driven by the supersaturation and is assisted by the applied stress, temperature, pressure or other external forces. For simplicity, in the model only the concentration gradient ($\vec{\nabla} c$) as the driving force was considered. The kinetic energy that activates the motion of matter was provided by the applied temperature (included in the diffusivity) and the stress state in the material was ignored.

In the model the formation of a secondary phase was not taken into account, just the segregation of solute atoms in the cavity. In reality, the growth of a cavity during creep deformation is inevitable, due to the atomic transport from the cavity surface and the diffusion of vacancies. However, in the model the cavity propagation was ignored and a fixed volume and shape of the cavity and the grain boundary was assumed. This approximation is not fulfilled in practice during creep deformation, but strongly simplifies the calculations.

Although, in the FE model several key mechanisms that take place during diffusional void filling were omitted and most of the phenomena were simplified, the most important and the most contributing mechanism of cavity filling, i.e. the solute volume diffusion, was considered. This made it possible to estimate the time for the full volume filling of a creep cavity, together with the assessment of the parameters controlling it.

6.2. FE model specifications

As stated before, the model was based on a cavity that is created during creep deformation transversely to an applied stress. An example of such a defect is presented in Fig. 6.1. On the left-hand side, a real microscopy image, where a cavities appeared at a grain boundary, can be seen. On the right-hand side, a simplified drawing of a grain with multiple cavities, which are assumed to form in lens-shapes [69]. In the model only one cavity embedded on a boundary was taken into consideration, but also the existence of neighbouring voids was considered, as the box radius corresponds to the half of the intercavity spacing (dashed rectangle, Fig. 6.1). Due to the fact, that the cavity is in the form of a lens-shape, the simulation box had to be represented as a cylinder (Fig. 6.2a). The box shows a rotation symmetry, which is schematically depicted in Fig. 6.2b. In the cylindrical coordinate system the radius is r and the height is z. When cut in half, the lens-shape is called a spherical cap (Fig. 6.2b). The shape originates from two phenomena [69]:

1. The surface diffusion, that maintains the uniform curvature during cavity growth, causes the free surfaces of the cavity to be spherical segments.

2. The surface tension forces establish the angles between the cavity and cavity-matrix interfaces to satisfy equilibrium conditions.

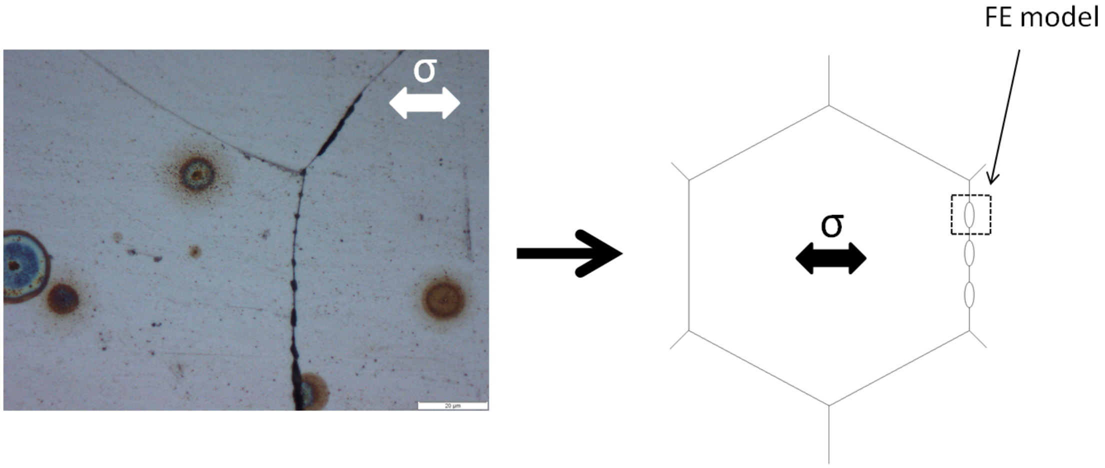

Figure 6.1: Left-hand side: a real optical microscopy picture of the Fe4W alloy's surface, after interrupted creep ($0.75t_R$) at 550°C and 140 MPa, with grain boundaries and cracks, along one of them. Right-hand side: a schematic representation of an exemplary grain with multiple cavities along the grain boundary. The arrow indicate the direction of the applied stress (σ). The dashed lines indicate a region of interest used for the FE model.

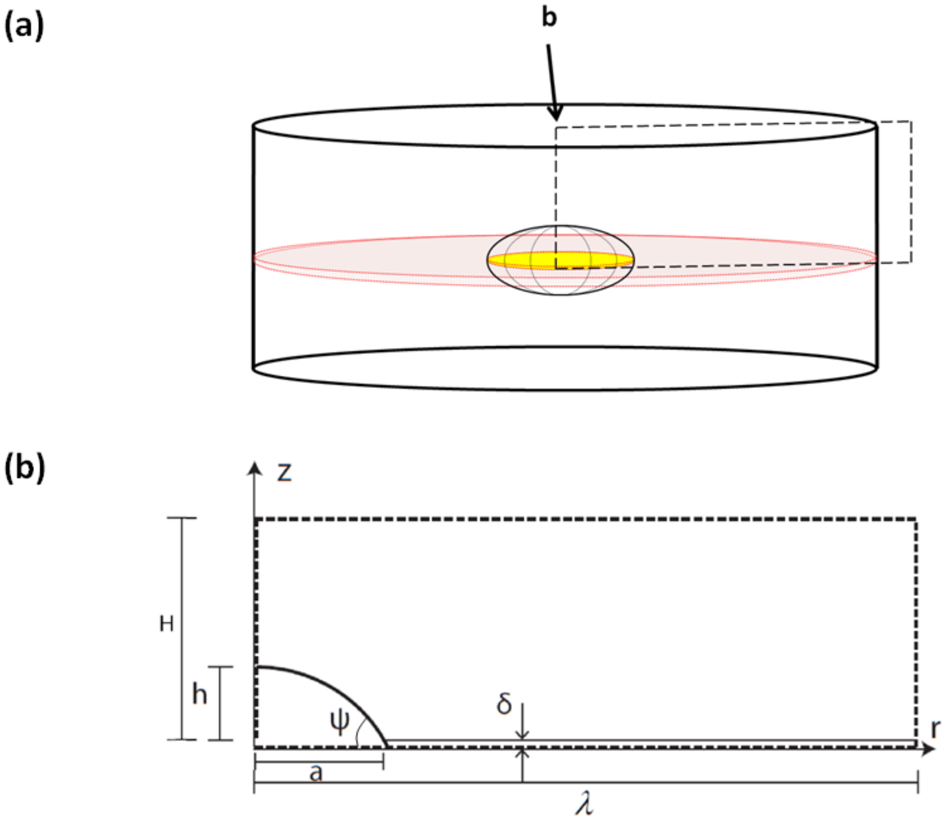

Figure 6.2: (a)A cylindrical sample volume containing a grain boundary (in red) with a lens-shaped cavity studied in the FE simulation. (b) Simulation box used in the FE model [80]. The dimensions of the simulation box are presented in Table 6.1.

Table 6.1: A list of all parameters used to define the simulation box, together with their symbols and values. The height of the spherical cap h directly scales with its radius a with: $h/a = (1 - \cos(\psi))/\sin(\psi)$ [80].

Parameter	Symbol	Value
Grain boundary thickness	δ	0.5 nm
Height of the spherical cap (half cavity)	h	38.5 nm
Height of the simulation box	H	2 μm
Radius of the spherical cap	a	50 nm
Opening angle of the cavity	ψ	75°
Radius of the simulation box	λ	adjustable

The volume of the cavity presented in Fig.6.2b was calculated using the following equation,

$$V_{cav} = \frac{4}{3}\pi a^3\left(1 - \frac{3}{2}\cos(\psi) + \frac{1}{2}\cos^3(\psi)\right). \tag{6.3}$$

This volume at the complete filling is equal to the number of atoms N multiplied by the atomic volume $\Omega = 0.0117\ \text{nm}^3$:

$$V_{fill} = N \cdot \Omega. \tag{6.4}$$

With all of the requirements and parameters for the model, the mesh was generated and the boundary conditions were set. The chosen mesh is presented in Fig. 6.3. The different coarsening densities of the mesh are connected with the fact, that one wants to achieve a better estimation of the solute diffusional flux around the surface of the cavity (hence, the greater density of mesh blocks) than in the bulk of the material.

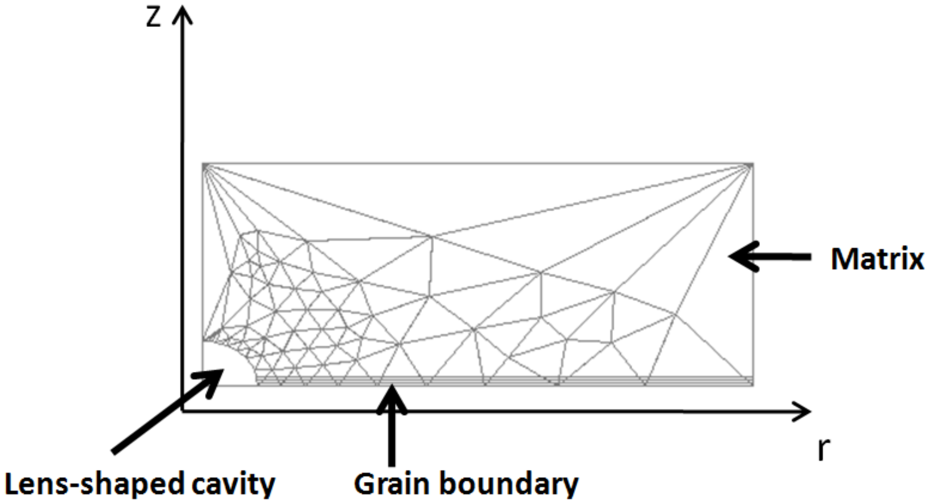

Figure 6.3: Mesh used in the FE simulation of the creep cavity filling by solute diffusion.

The two boundary conditions set for the model are:

1. The solute concentration on the inside of the surface of the cavity was set to be constant at a value of $c_1 = 0.0001$.
2. At the edges of the simulation box the diffusional flux was set to be zero.

Additionally, the starting parameters had to be defined and were as follows:

1. The solute concentration in the material was set to the nominal concentration: $c(r \geqslant a) = c_0 = 0.01$.
2. The radius of the simulation box, λ, was equal to a half of the intercavity spacing.

Furthermore, the simulation was programmed to stop when a sufficient amount of solute was diffused into the cavity. At this point, the volume of the cavity was fully filled with solute atoms: $V_{fill} = V_{cavity.}$

6.3. FE simulation results and discussion

The concentration profile for this model was adapted to be comparable to earlier results for the Fe-Au alloys, studied by Zhang [86]. The FE calculation, in case of Fe-Au, were performed in the same manner as hereby presented ones, but considered a spherical shape of a cavity. By comparing both results, a conclusive statement on the influence of the cavity shape on solute diffusion healing can be made.

In order to investigate the character of the diffusional solute process for the model, multiple combinations of diffusion coefficients for the volume (D_V) and the grain boundary (D_{GB}), as well as, the cavity radius (a) and the box radius (λ) (which defines the spacing between the other neighbouring cavity) were selected. The intercavity spacing was varied to evaluate the impact of a proximity of a neighbouring cavity, along the same boundary, on the diffusional flux of solute. Therefore, the two key variables for the model were: the intercavity ratio (λ/a) and the diffusivity ratio (D_{GB}/D_V). The character of the diffusional flux and the time of cavity filling was investigated in terms of diffusivity and size effects. The intercavity ratio took the values of λ/a = 2, 3, 5, 10, 20, 50, 100, 200, 400, while the diffusivity ratio (D_{GB}/D_V) was varied over 18 orders of magnitude. Examples of the obtained concentration profiles, at full cavity filling, are shown in Fig. 6.4. Three different behaviours of concentration profiles could be distinguished, which correspond to three different diffusion flux fields.

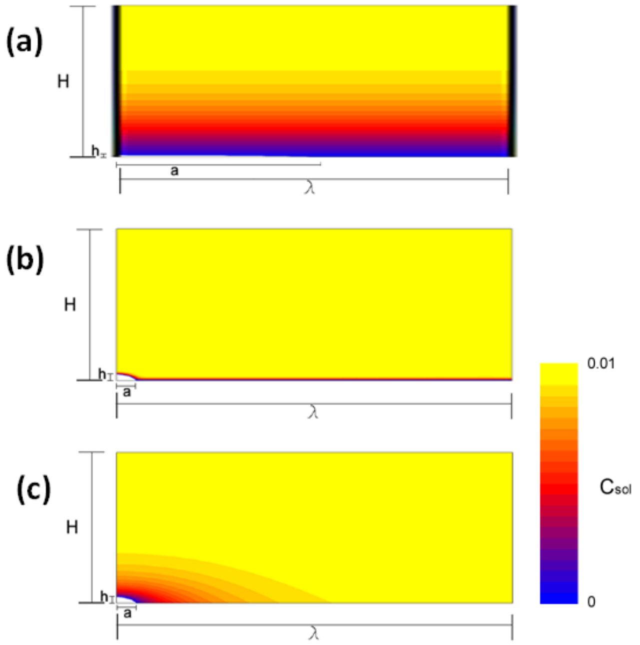

Figure 6.4: FE solute concentration profiles at full cavity filling for (a) $\lambda/a = 2$, $D_{GB}/D_V = 1$, (b) $\lambda/a = 20$, $D_{GB}/D_V = 10^8$, (c) $\lambda/a = 20$, $D_{GB}/D_V = 10^3$ [80]. The data are shown for a supersaturation of $\Delta c = 0.01$.

The three types of concentration profiles observed at the full cavity filling are:

1. 1D diffusion field: as depicted in Fig. 6.4a, takes the character of a planar diffusion field. The solute atoms are fed both to the cavity and the grain boundary at the same rate only from one direction (z-direction). This phenomenon happens when there is an insufficient amount of solute atoms available inside the grain boundary. All the solute atoms are immediately diffused into the cavity from the grain boundary and the cavity, together with the boundary, is filled with the solute atoms from the volume of the material. This type of diffusion field can be observed for small intercavity ratios ($\lambda/a < 50$), and it is independent of the diffusivity ratio. For the 1D diffusion field the solute transport to the cavity is solely controlled by the volume diffusion.

2. 2D diffusion field: as depicted in Fig. 6.4b, the concentration gradient is focused on the grain boundary. This means, that the fast transport of solute through the grain boundary into the cavity is accommodated. This phenomenon happens when the solute in the grain boundary is sufficient to fill the cavity,

and takes place for high diffusivity ratios ($D_{GB}/D_V >> 1$) and high intercavity ratios ($\lambda/a \geqslant 50$). In 2D diffusion field the solute transport to the cavity is controlled by the grain boundary diffusion.

3. 3D diffusion field: as depicted in Fig. 6.4c, the concentration gradient is observed from every direction. This diffusion profile appears when $D_{GB} \leqslant D_V$. Then, there is hardly any solute supplied to the grain boundary. The 3D diffusion occurs as long as the diffusion profile does not reach the box radius (for $\lambda/a \geqslant 5$). In 3D diffusion field the solute transport to the cavity is controlled by the volume diffusion. The solute is also transported along the grain boundary, but it makes only a small contribution, thus it does not control the solute transport.

The cross-overs from 1D and 3D (or 3D to 1D) are gradual rather than sharp. Therefore, there are diffusion fields at full creep cavity diffusional filling that take the character of a quasi-2D profile. The diffusion profiles can also be analyzed in terms of the cavity filling time (t_{fill}). In Fig. 6.5, the time to full cavity filling is plotted as a function of D_{GB} and D_V for different λ/a ratios. The diffusion profiles were registered at the time when the cavity was fully filled, at which the simulation was stopped.

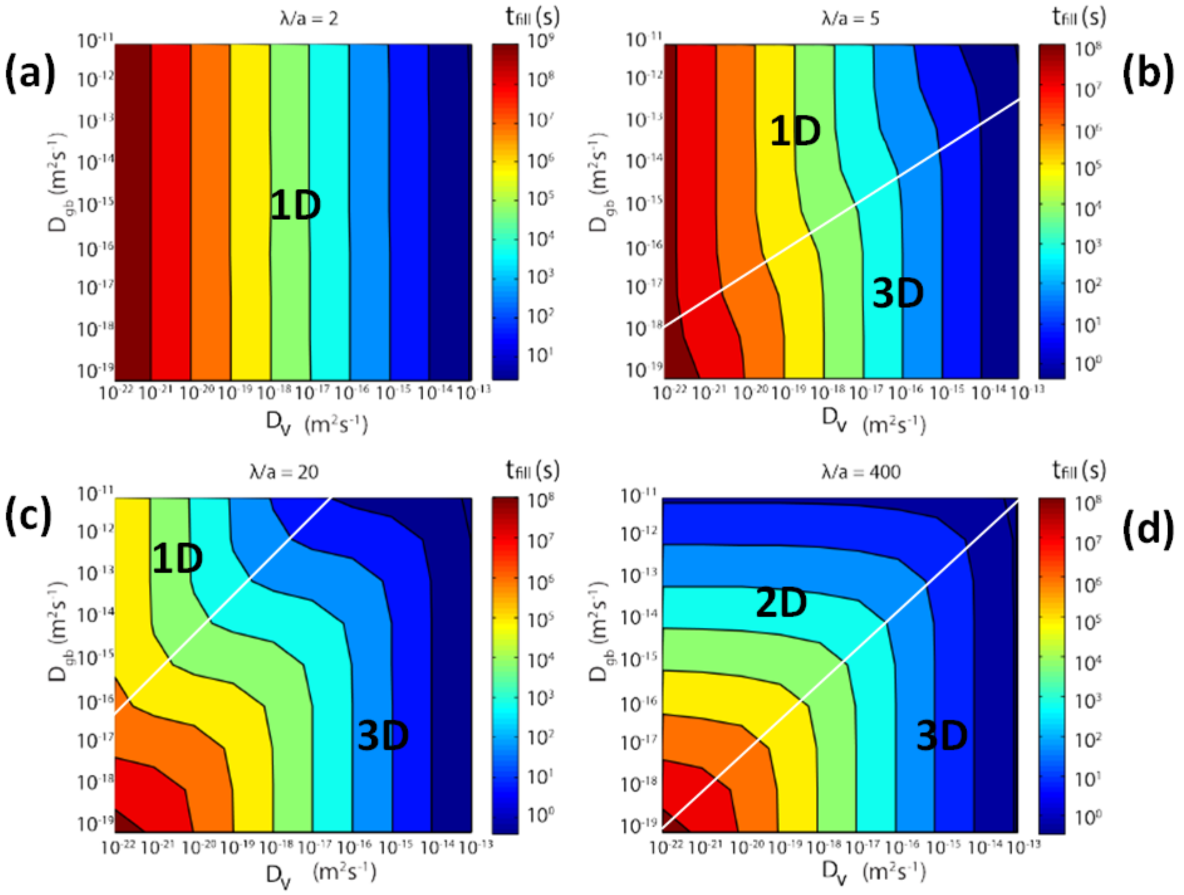

Figure 6.5: Cavity filling time t_{fill} for intercavity ratios of λ/a= (a) 2, (b) 5, (c) 20 and (d) 400 as a function of the volume diffusivity D_V and the grain-boundary diffusivity D_{GB} [80]. The data are shown for a supersaturation of $\Delta c = 0.01$.

Fig. 6.5a shows, that the volume diffusivity solely controls the filling time over the entire range of diffusivity ratios (1D). Fig. 6.5b shows that the volume diffusivity is still the dominating factor controlling the filling time for all values of diffusivity ratios. However, for ceratin D_{GB}/D_V ratios, there is a transition where the grain-boundary diffusion has an impact on the filling time (1D to 3D). The same transition takes place in Fig. 6.5c, with an exception, that it is more pronounced, which shows an even bigger impact of the grain-boundary diffusion on the filling time (such an impact, which is a short period of 2D behaviour, is regarded as a gradual transition from 1D to 3D behaviours – quasi-2D). These grain boundary diffusion impacts on the filling time are the perfect indications of the profile change from 1D to 3D. Such transitions mark the points when the grain boundary is no longer fully depleted at the beginning of a simulation and contributes to the filling of the cavity, without controlling it. Finally, in Fig. 6.5d, a clear transition between 3D behaviour, controlled by D_V, to 2D behaviour, controlled by D_{GB} is observed.

An alternative representation of how grain boundary and volume diffusion influence the time to complete filling of the cavity is presented in Fig. 6.6. From the graph an influence of the diffusivity ratio (with a fixed $D_V = 10^{-22}$ m^2/s) on the filling time can be described as follows:

- $\lambda/a = 2$: Volume diffusion is the primary factor controlling the filling time, so while the grain-boundary increases (increasing the diffusivity ratio), the filling time stays constant. Meaning, that the grain boundary diffusion has no impact on the solute diffusion into the cavity. Solute atoms are instantly depleted from the short grain boundary to the cavity without affecting the diffusion profile and the filling time. This curve depicts 1D diffusion profile without any transitions.

- $\lambda/a = 5$: Volume diffusion is also the primary factor that controls the filling time. However, for intermediate diffusivity ratios, there is a short period of a linear decrease in the filling time with the increasing grain-boundary diffusivity, followed and proceeded by its constant periods. This means, that the diffusion profile changes from 3D to 1D behaviour with a transition (linear decay), which indicates the impact of the grain-boundary diffusivity (quasi-2D). This curve depicts a profile change from 3D to quasi-2D to 1D.

- $\lambda/a = 20$: Volume diffusion is the primary factor influencing the filling time just for small values of diffusivity ratios (3D). At the end, the time curve shows a linear decrease with the increasing grain-boundary diffusivity. The linear decrease is associated with a transition at which the grain-boundary diffusivity impacts the filling time, which is the registered pronounced transition from 3D to 1D (see Fig. 6.5c). The curve depicts a diffusion profile change from 3D to quasi-2D.

- $\lambda/a = 400$: Volume diffusion is again the primary factor influencing the filling time just for small values of diffusivity ratios (3D). At the end, the time curve shows a linear decrease with the increasing grain-boundary diffusivity. The linear decrease is this time associated with the grain-boundary control over the filling time, which is a 2D profile behaviour (see Fig. 6.5d). The curve depicts a diffusion profile change from 3D to 2D.

In summary, when the time curve shows a linear decay over increasing diffusivity ratio, the time to the full cavity filling, together with solute transport, is controlled by grain-boundary diffusion (corresponding to either quasi-2D or 2D profile). When the time curve is constant, the time to the full cavity filling and solute transport are controlled by the volume diffusion (corresponding to either 1D or 3D profile). A combined picture of the influence of changing diffusivity ratio and changing intercavity ratio on the filling time of the cavity is presented in Fig. 6.7.

From the contour plot in Fig. 6.7, the aforementioned filling time control filling time of specific diffusivity ratios for specific intercavity ratios can be observed thanks to the color bar depicting the magnitudes of filling time. The white dots, marked on the figure correspond to the registered cavity filling times for the investigated diffusivities and intercavity ratios. The diffusion influences were registered at times when the cavity was fully filled and the simulations stopped. From the figure it can be observed, that the changing diffusivity ratio (i.e. grain-boundary diffusivity) has little influence on the filling time for small intercavity ratios ($\lambda/a = 2, 5$). With the increasing intercavity ratio, the changing diffusivity ratio begins to contribute to the change of the filling time. For the intermediate intercavity ratios (λ/a = 10, 20), the varying diffusivity ratio has an influence on the filling time for its smaller values, while for its larger values it does not significantly change the magnitude of the filling time. For big intercavity ratios (λ/a = 50, 100, 200, 400), the changing diffusivity ratio has the most significant influence on the filling time as its changing magnitude changes the magnitude of the filling time of the cavity. Fig. 6.7 proves, that the dominance of grain boundary diffusion over the solute transport to the cavity and the filling time of the cavity greatly depends on the length of the grain boundary, along which the cavity lies on. Furthermore, the grain-boundary diffusion can control the filling of the cavity only when its diffusivity is much larger compared to the diffusivity of the volume.

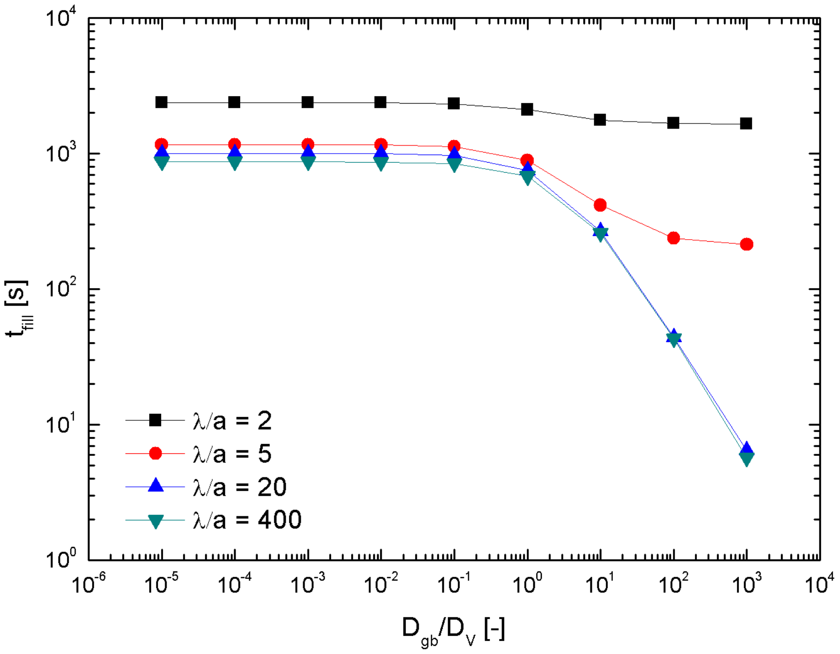

Figure 6.6: Time to complete filling t_{fill} as a function of D_{GB}/D_V for four different intercavity ratios: $\lambda/a = 2, 5, 20, 400$. t_{fill} is plotted at a constant D_V=10^{-19} m^2/s. All data are obtained for a supersaturation of $\Delta c = 0.01$.

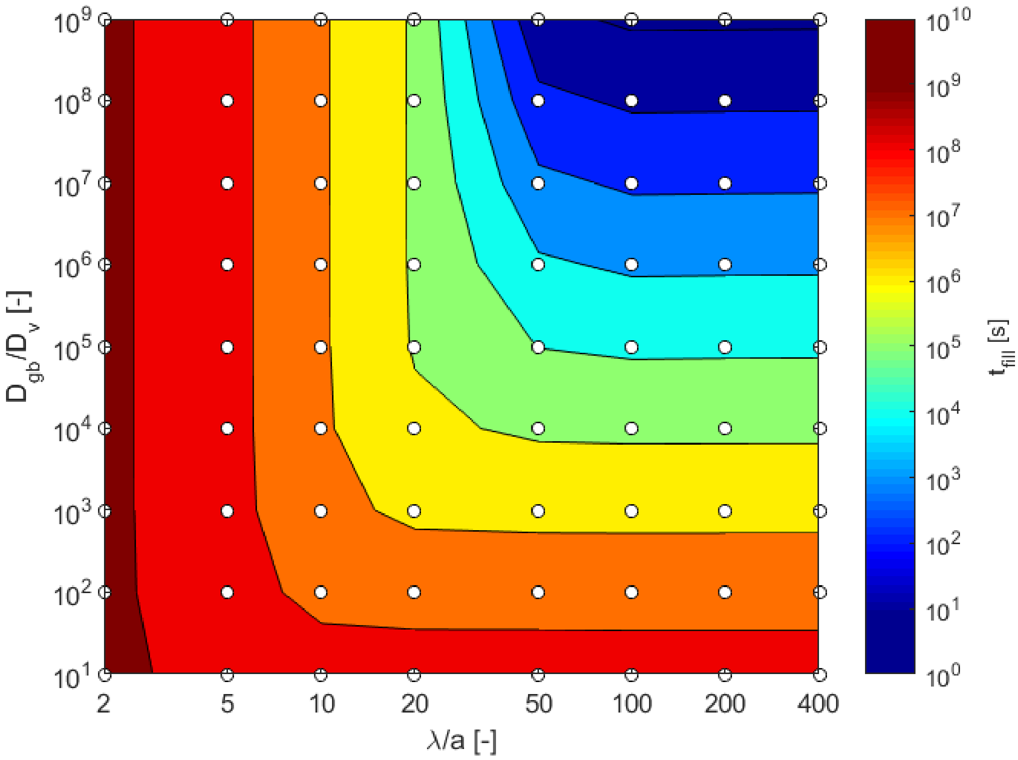

Figure 6.7: Time to complete filling t_{fill} as a function of D_{GB}/D_V and λ/a. t_{fill} is plotted at a constant D_V=10^{-22} m^2/s. All data are obtained for a supersaturation of $\Delta c = 0.01$

6.4. Conclusions and recommendations

The FE simulations of diffusional cavity filling have provided a detailed insight in the behaviour of supersaturated solute transport into a creep-induced cavity, located on a grain boundary oriented transversely to the applied stress. One can learn from these calculations that the filling of the cavity is controlled by the volume diffusion in most of the cases, but is also often affected by the grain-boundary diffusion. The time required for filling depends on two variables, i.e. diffusivity ratio D_{GB}/D_V and intercavity spacing ratio λ/a, which proves that the diffusion mechanisms show size and solute rate effects. For a relatively fast grain-boundary diffusivity, the size factor λ/a determines if the solute, needed for a complete filling, has to be provided into the cavity from the volume or can be entirely drained from the grain boundary.

Moreover, three different diffusion profiles have been distinguished at the diffusive full filling of the grain-boundary cavity. Namely, 1D diffusion profile, which shows the behaviour of the solute transport for small intercavity distances, when the amount of solute in the grain boundary is insufficient. This profile appeared to be independent of the diffusivity. Secondly, 2D diffusion profile, which shows the behaviour of the solute transport when the grain-boundary diffusion is dominant. This profile is controlling the solute diffusion for big intercavity distances when the grain-boundary diffusion is significantly faster compared to the volume diffusion. Finally, 3D diffusion profile, which shows the behaviour of the solute transport when the volume diffusion is dominant over contributing grain-boundary diffusion. This profile is controlling the solute diffusion for big intercavity distances, when the grain-boundary diffusion and the volume diffusion are of a similar rate, as well as, when the grain boundary diffusivity is slightly smaller compared to the volume diffusivity.

By comparing this model to the model established by Zhang [86], there is no noticeable effect of the cavity shape on the diffusion profiles or the filling time. Zhang [86] considered only one inetrcavity spacing ($\lambda/a = 250$) over the same values of diffusivity ratios. The observed behaviours for diffusional flux are quantitatively the same.

From the tomographic reconstructions (described in Chapter 4) it has been found that the average intercavity spacing ratio λ/a in the Fe4W alloys, subjected to creep at 550°C and 160 MPa, is around 2. This is caused by the fact, that the cavities induced during creep deformation are relatively big in sizes and not that distantly apart. The diffusion of tungsten in α-Fe matrix is of the order of 10^{-22} m^2/s at 550°C [76], while the grain-boundary diffusion in high-purity iron is of the order of 10^{-17} m^2/s [47] at the same temperature ($D_{GB}/D_V = 10^5$). These values of intercavity spacing ratio and diffusivity ratio correspond to the 1D concentration profile at full cavity filling (see Fig. 6.4a and Fig. 6.5a). This means, that the solute transport into cavities in Fe4W alloys, during creep at 550°C, is solely governed by volume diffusion, which has also been pointed out in Chapter 4 (Fig. 4.11).

In order to further improve the FE model one can consider the following recommendations. The simulation would be more realistic if the cavity growth mechanism, together with a descriptive model for the precipitation inside the cavity, was included. Furthermore, an incorporation of the external factors controlling the solute transport into the cavity, i.e. stress fields, would improve the results of the cavity filling time and its dependence on the size and diffusivity effect. Finally, a representation of a cavity that is located on an inclined grain boundary (to the applied stress), and an incorporation of the grain boundary sliding effect on its shape, would give a chance to investigate a different diffusion-based solute transport.

Bibliography

[1] F. Abe. Development of creep-resistant steels and alloys for use in power plants. In *Structural Alloys for Power Plants*, pages 250–293. Elsevier, 2014.

[2] F. Abe, T.U. Kern, and R. Viswanathan. *Creep-resistant steels*. Elsevier, 2008.

[3] J. Als-Nielsen and D. McMorrow. *Elements of modern X-ray physics*. John Wiley & Sons, 2011.

[4] M.F. Ashby, C. Gandhi, and D.M.R. Taplin. Overview no. 3 fracture-mechanism maps and their construction for fcc metals and alloys. *Acta metallurgica*, 27(5):699–729, 1979.

[5] ASTM. 2990-01. standard test methods for tensile, compressive, and flexural creep and creep-rupture of plastics. *West Conshohocken: ASTM International*, 2001.

[6] J. Banhart, A. Borbély, K. Dzieciol, F. Garcia-Moreno, I. Manke, N. Kardjilov, A.R. Kaysser-Pyzalla, M. Strobl, and W. Treimer. X-ray and neutron imaging–complementary techniques for materials science and engineering: Dedicated to professor dr. H.-P. Degischer on the occasion of his 65th birthday. *International Journal of Materials Research*, 101(9):1069–1079, 2010.

[7] H.K.D.H. Bhadeshia. Creep-resistant steel, case study, accessed: 29 July 2016. URL `https://www.phase-trans.msm.cam.ac.uk/mphil/MP6-14.pdf`.

[8] J-Y. Buffiere, E. Maire, J. Adrien, J-P. Masse, and E. Boller. In situ experiments with X-ray tomography: an attractive tool for experimental mechanics. *Experimental mechanics*, 50(3):289–305, 2010.

[9] J. W. Cahn. Nucleation on dislocations. *Acta Metallurgica*, 5(3):169–172, 1957.

[10] D. Caillard and J.-L. Martin. *Thermally activated mechanisms in crystal plasticity*, volume 8, chapter 3.2: Dislocations interacting with mobile solute atoms, pages 63–72. Elsevier, 2003.

[11] W.D. Callister and D.G. Rethwisch. *Materials science and engineering*, chapter 11.9: Precipitation Hardening, pages 437–442. John Wiley & Sons NY, 2011.

[12] W.D. Callister and D.G. Rethwisch. *Materials science and engineering*, chapter 7.10: Strain hardening, pages 215–218. John Wiley & Sons NY, 2011.

[13] J.-H. Cho, H.-P. Ha, and K.H. Oh. Recrystallization and grain growth of cold-rolled gold sheet. *Metallurgical and Materials Transactions A*, 36(12):3415–3425, 2005.

[14] P. Cloetens. Tomography and holotomography: School on X-ray micro and nanoprobes, 2007. URL `http://xrm.phys.northwestern.edu/research/pdf_papers/misc/cloetens_holotomography_course_2009.pdf`.

[15] P. Cloetens, J.P. Guigay, W. Ludwig, L. Salvo, M. Schlenker, M. Suéry, and S. Verrier. Holotomography now operational, 1999. URL `http://www.esrf.eu/UsersAndScience/Publications/Highlights/1999/tech-inst/holotom.html`.

[16] P. Cloetens, W. Ludwig, J. Baruchel, D. Van Dyck, J. Van Landuyt, J.P. Guigay, and M. Schlenker. Holotomography: Quantitative phase tomography with micrometer resolution using hard synchrotron radiation X-rays. *Applied physics letters*, 75(19):2912–2914, 1999.

[17] P. Cloetens, R. Mache, M. Schlenker, and S. Lerbs-Mache. Quantitative phase tomography of Arabidopsis seeds reveals intercellular void network. *Proceedings of the National Academy of Sciences*, 103(39):14626–14630, 2006.

[18] A.H. Cottrell and M. A. Jaswon. Distribution of solute atoms round a slow dislocation. *Proceedings of the Royal Society of London. Series A, Mathematical and Physical Sciences*, 199(1056):104–114, 1949.

[19] T.H. Courtney. *Mechanical behavior of materials*, chapter 5.6: Particle hardening, pages 198–205. Waveland Press, 2005.

[20] Pearson's Crystal Data. Powder pattern of 260804 Fe2W - MgZn2 hP12 194, 2016. URL `http://www.crystalimpact.com`. Original document from Pearson's Crystal Data.

[21] R.D. Doherty, D.A. Hughes, F.J. Humphreys, J.J. Jonas, D. Juul Jensen, M.E. Kassner, W.E. King, T.R. McNelley, H.J. McQueen, and A.D. Rollett. Current issues in recrystallization: A review. *Materials Science and Engineering: A*, 238(2):219–274, 1997.

[22] C. Dry. Matrix cracking repair and filling using active and passive modes for smart timed release of chemicals from fibers into cement matrices. *Smart Materials and Structures*, 3(2):118, 1994.

[23] N. Esposito, L.and Bonora. Time-independent formulation for creep damage modeling in metals based on void and crack evolution. *Materials Science and Engineering: A*, 510:207–213, 2009.

[24] H. Fang, C.D. Versteylen, S. Zhang, Y. Yang, P. Cloetens, D. Ngan-Tillard, E. Brück, .S van der Zwaag, and N.H. van Dijk. Autonomous filling of creep cavities in Fe-Au alloys studied by synchrotron X-ray nano-tomography. *Acta Materialia*, 121:352–364, 2016.

[25] Central Facility for Advanced Microscopy and Microanalysis. Introduction to Energy Dispersive X-ray Spectrometry (eds), 2016. URL `http://cfamm.ucr.edu/documents/eds-intro.pdf`.

[26] H.J. Frost and Michael F. Ashby. *Deformation mechanism maps: the plasticity and creep of metals and ceramics*. Pergamon press, 1982.

[27] C. Gandhi and M.F. Ashby. Overview no. 5: Fracture-mechanism maps for materials which cleave: Fcc, bcc and hcp metals and ceramics. *Acta Metallurgica*, 27(10):1565–1602, 1979.

[28] S.J. Garcia, H.R. Fischer, and J.S. Roman. *Self-healing polymer systems: properties, synthesis and applications*. Elsevier Limited, 2014.

[29] R.S. Gates. The role of grain boundary dislocations in grain boundary sliding. *Acta Metallurgica*, 21(7):855–864, 1973.

[30] S.K. Ghosh. *Self-healing materials: fundamentals, design strategies, and applications*. John Wiley & Sons, 2009.

[31] R.C. Gifkins. Grain-boundary sliding and its accommodation during creep and superplasticity. *Metallurgical and Materials Transactions A*, 7(8):1225–1232, 1976.

[32] G. Gottstein. *Physical foundations of materials science*. Springer Science & Business Media, 2013.

[33] M.E. Gramsma. Self-healing of deformation-induced defects in Fe-based alloys using positron annihilation techniques. Master's thesis, Deflt University of Technology, 2015.

[34] Weaver Research Group. Creep and superplasticity, 2012. URL `http://bama.ua.edu/~mweaver/courses/MTE585/Creep2.pdf`.

[35] E. Gutierrez-Miravete. Creep/viscoplasticity, 2005. URL `http://www.ewp.rpi.edu/hartford/~ernesto/F2005/CINVESTAV/Notes/ch6.pdf`.

[36] E. Gutierrez-Miravete. Creep, 2005. URL `http://www.ewp.rpi.edu/hartford/~ernesto/S2005/MEF2/Notes/ch09.pdf`.

[37] M.D. Hager, P. Greil, C. Leyens, S. van der Zwaag, and U.S. Schubert. Self-healing materials. *Advanced Materials*, 22(47):5424–5430, 2010.

[38] M. Hammer. X-ray physics: X-ray interaction with matter and attenuation, 2004. URL `http://xrayphysics.com/attenuation.html`.

[39] S.M. He, N.H. Van Dijk, M. Paladugu, H. Schut, J. Kohlbrecher, F.D. Tichelaar, and S. Van der Zwaag. In situ determination of aging precipitation in deformed Fe-Cu and Fe-Cu-BN alloys by time-resolved small-angle neutron scattering. *Physical Review B*, 82(17):174111, 2010.

[40] S.M. He, N.H. Van Dijk, H. Schut, E.R. Peekstok, and S. Van der Zwaag. Thermally activated precipitation at deformation-induced defects in Fe-Cu and Fe-Cu-BN alloys studied by positron annihilation spectroscopy. *Physical Review B*, 81(9):094103, 2010.

[41] M. Heethoff and P. Cloetens. A comparison of synchrotron X-ray phase contrast tomography and holotomography for non-invasive investigations of the internal anatomy of mites. *Soil Organisms*, 80(2): 205–215, 2008.

[42] G.T. Herman. *Fundamentals of computerized tomography: image reconstruction from projections*. Springer Science & Business Media, 2009.

[43] C. Herring. Diffusional viscosity of a polycrystalline solid. *Journal of applied physics*, 21(5):437–438, 1950.

[44] Jiang Hsieh et al. Computed tomography: principles, design, artifacts, and recent advances. SPIE Bellingham, WA, 2009.

[45] D. Hull and D.J. Bacon. *Introduction to dislocations*, chapter 10.5: Solute atmospheres and yield phenomena, pages 220–228. Butterworth-Heinemann, 2001.

[46] D. Hull and D.E. Rimmer. The growth of grain-boundary voids under stress. *Philosophical Magazine*, 4 (42):673–674, 1959.

[47] A. Inoue, H. Nitta, and Y. Iijima. Grain boundary self-diffusion in high purity iron. *Acta Materialia*, 55 (17):5910–5916, 2007.

[48] A. Isaac, F. Sket, W. Reimers, B. Camin, G. Sauthoff, and A.R. Pyzalla. In situ 3D quantification of the evolution of creep cavity size, shape, and spatial orientation using synchrotron X-ray tomography. *Materials Science and Engineering: A*, 478(1):108–118, 2008.

[49] M.E. Kassner. *Fundamentals of creep in metals and alloys*. Butterworth-Heinemann, 2015.

[50] U.F. Kocks. The relation between polycrystal deformation and single-crystal deformation. *Metallurgical and Materials Transactions B*, 1(5):1121–1143, 1970.

[51] M. Kuzmina, D. Herbig, M.and Ponge, S. Sandlöbes, and D. Raabe. Linear complexions: Confined chemical and structural states at dislocations. *Science*, 349(6252):1080–1083, 2015.

[52] E.N. Landis and D.T. Keane. X-ray microtomography. *Materials characterization*, 61(12):1305–1316, 2010.

[53] E. Lassner and W.-D. Schubert. *Tungsten: properties, chemistry, technology of the element, alloys, and chemical compounds*. Springer Science & Business Media, 2012.

[54] K.-H. Lee, S.-M.and Huh J.Y. Suh, J.-Y.and Hong, and W.S. Jung. Microstructural evolution and creep-rupture life estimation of high-Cr martensitic heat-resistant steels. *Materials Characterization*, 106:266–272, 2015.

[55] Y.g Li, S. Li, M. Huang, and Z. Li. Analytical solution for Coble creep in polycrystalline materials under biaxial loading. *Mechanics of Materials*, 91:290–294, 2015.

[56] I. Manke. X-ray tomography, 2016. URL `https://www.helmholtz-berlin.de/forschung/oe/em/werkstoffe/methoden/x-tomo/index_en.html`.

[57] F. Masuyama. History of power plants and progress in heat resistant steels. *ISIJ international*, 41(6): 612–625, 2001.

[58] K.L. Murty. Creep and stress rupture. 2004. URL `http://www4.ncsu.edu/~murty/MAT450/NOTES/creep.pdf`.

[59] Y.S. Na and J.H. Lee. Interpretation of viscous deformation of bulk metallic glasses based on the Nabarro–Herring creep model. *Journal of materials processing technology*, 187:786–790, 2007.

[60] F.R.N. Nabarro and J.P. Hirth. *Dislocations in solids*, volume 12, chapter 8.5.3: Dislocations and Indentations: Metals, page 526. Elsevier, 2004.

[61] W.D. Nix. Mechanisms and controlling factors in creep fracture. *Materials Science and Engineering: A*, 103(1):103–110, 1988.

[62] W.D. Nix, K.S. Yu, and J.S. Wang. The effects of segregation on the kinetics of irrtergranular cavity growth under creep conditions. *Metallurgical and Materials Transactions A*, 14(3):563–570, 1983.

[63] D.M. Owen and T.G. Langdon. Low stress creep behavior: An examination of Nabarro—Herring and Harper—Dorn creep. *Materials Science and Engineering: A*, 216(1-2):20–29, 1996.

[64] Sprawls P. Interaction of radiation with matter, accessed: 20 November 2017. URL `http://www.sprawls.org/ppmi2/INTERACT/#Compton`.

[65] J. Pelleg. *Mechanical properties of ceramics*, volume 213. Springer Science & Business, 2014.

[66] N.L. Peterson. Self-diffusion in pure metals. *Journal of Nuclear Materials*, 69:3–37, 1978.

[67] J. Philibert. Creep and diffusion. *Solid State Ionics*, 12:321–336, 1984.

[68] R. Raj and M.F. Ashby. On grain boundary sliding and diffusional creep. *Metallurgical and Materials Transactions B*, 2(4):1113–1127, 1971.

[69] R. Raj and M.F. Ashby. Intergranular fracture at elevated temperature. *Acta Metallurgica*, 23(6):653–666, 1975.

[70] H.M.M.A. Rashed, J.D. Robson, P.S. Bate, and B. Davis. Application of X-ray microtomography to analysis of cavitation in az61 magnesium alloy during hot deformation. *Materials Science and Engineering: A*, 528 (6):2610–2619, 2011.

[71] Y. Shima, Y. Ishikawa, H. Nitta, Y. Yamazaki, K. Mimura, M. Isshiki, and Y. Iijima. Self-diffusion along dislocations in ultra high purity iron. *Materials Transactions*, 43(2):173–177, 2002.

[72] R.E. Smallman and A.H.W. Ngan. *Physical metallurgy and advanced materials*. Butterworth-Heinemann, 2011.

[73] R.N. Stevens. Grain boundary sliding and diffusion creep. *Surface Science*, 31:543–565, 1972.

[74] G. Sundararajan. The Monkman-Grant relationship. *Materials Science and Engineering: A*, 112:205–214, 1989.

[75] Z. Suo. Evoloving small structures: the vacancy, 2009. URL `http://imechanica.org/files/L02%20Vacancy.pdf`.

[76] S. Takemoto, H. Nitta, S.Y. Iijima, and Y. Yamazaki. Diffusion of tungsten in α-iron. *Philosophical Magazine*, 87(11):1619–1629, 2007.

[77] H. Torres, M. Varga, and M. Rodríguez Ripoll. High temperature hardness of steels and iron-based alloys. *Materials Science and Engineering: A*, 671:170–181, 2016.

[78] S. van der Zwaag. *Self healing materials: an alternative approach to 20 centuries of materials science*. Springer Science+ Business Media BV, 2008.

[79] S. van der Zwaag and E. Brinkman. *Self healing materials: Pioneering research in the Netherlands*. IOP-Press, 2015.

[80] C.D. Versteylen, N.K. Szymanski, M.H.F. Sluiter, and N.H. van Dijk. Finite element modelling of creep cavity filling by solute diffusion. Submitted to Philosophical Magazine.

[81] J. Wadsworth, O.A. Ruano, and O.D. Sherby. Deformation by grain boundary sliding and slip creep versus diffusional creep. In *Minerals, Metal and Materials Society Annual Meeting, San Diego, Calif*, 1999.

[82] Y.-J. Wang, A. Ishii, and S. Ogata. Grain size dependence of creep in nanocrystalline copper by molecular dynamics. *Materials Transactions*, 53(1):156–160, 2012.

[83] Y. Weerakkody. Filtered back projection, 2017. URL `https://radiopedia.org/articles/filtered-back-projection-1`.

[84] S.R. White, N.R. Sottos, P.H. Geubelle, J.S. Moore, M.R. Kessler, S.R. Sriram, E.N. Brown, and S. Viswanathan. Autonomic healing of polymer composites. *Nature*, 409(6822):794–797, 2001.

[85] P. Yavari and T.G. Langdon. The transition from nabarro-herring to harper-dorn creep at low stress levels. *Scripta Metallurgica*, 11(10):863–866, 1977.

[86] S. Zhang. *Self healing of damage in Fe-based alloys*. PhD thesis, Technische Universiteit Delft, 2015.

[87] S. Zhang, C. Kwakernaak, W. Sloof, S. Brück, E.and van der Zwaag, and N.H. van Dijk. Self healing of creep damage by gold precipitation in iron alloys. *Advanced Engineering Materials*, 17(5):598–603, 2015.

[88] S. Zhang, C. Kwakernaak, F.D. Tichelaar, W.G. Sloof, M. Kuzmina, M. Herbig, D. Raabe, E. Brück, S. van der Zwaag, and N.H. Van Dijk. Autonomous repair mechanism of creep damage in Fe-au and Fe-Au-BN alloys. *Metallurgical and Materials Transactions A*, 46(12):5656–5670, 2015.

[89] S. Zhang, H. Fang, M.E. Gramsma, C. Kwakernaak, W.G. Sloof, Frans D. Tichelaar, M. Kuzmina, M. Herbig, D. Raabe, E. Brück, et al. Autonomous filling of grain-boundary cavities during creep loading in Fe-Mo alloys. *Metallurgical and Materials Transactions A*, 47(10):4831–4844, 2016.